A MESOSCOPIC MODEL FOR BLOOD FLOW PREDICTION BASED ON EXPERIMENTAL OBSERVATION OF RED BLOOD CELL INTERACTION

by

Erfan Niazi

Thesis Submitted In Partial Fulfillment of the Requirements

for the Doctorate in Philosophy Degree in Mechanical Engineering

Ottawa-Carleton Institute for Mechanical and Aerospace Engineering

Faculty of Engineering

University of Ottawa

Acknowledgments

I would like to express my genuine appreciation to my parents and my wife, for their unconditional support and love throughout my life. Accomplishments would not be possible without them.

This work was made possible through input from advisors, co-workers, friends and family. In particular I wish to thank Professor Marianne Fenech. She has shown a huge interest in this work and she has pushed me forward when needed. Professor James McDonald is also be mentioned, he put me on a right track and has been an avid reader of my output, giving loads of suggestions. Besides my supervisor, I would like to thank the rest of my thesis committee, for their insightful comments and questions, which assured that the research is proceeding on the right track from various perspectives.

Statement of Ethics Approval

The research involving human subjects that is reported in this thesis was conducted with the approval of the ethics committee of the University of Ottawa (H11-13-06).

Abstract

In some species, including humans, red blood cells (RBCs) under low shear stress tend to clump together and form into regular stacks called rouleaux. These stacks are not static, and constantly move and break apart. This phenomenon is referred to as red blood cell aggregation and disaggregation. When modelled as a single liquid, blood behaves as a non-Newtonian fluid. Its viscosity varies, mainly due to the aggregation of RBCs. The aim of this research is to develop a mesoscale computational model for the simulation of RBCs in plasma. This model considers RBC interaction and aggregation to predict blood-flow characteristics such as viscosity, rouleaux size and velocity distribution.

In this work, the population-balance modelling (PBM) approach is utilized to model the RBC aggregation process. The PBM approach is a known method that is used for modelling agglomeration and breakage in two-phase flow fluid mechanics to find aggregate size. The PBM model is coupled to the incompressible Navier-Stokes equations for the plasma. Both models are numerically solved simultaneously. The population-balance equation has been used previously in a more restricted form, the Smoluchowski equation, to model blood viscosity, but it has never been fully coupled with the Navier-Stokes equation directly for the numerical modelling of blood flow. This approach results in a comprehensive model which aims to predict RBC aggregate size and their velocities for different flow configurations, as well as their effects on the apparent macro-scale viscosity.

The PBM approach does not treat the microscopic physics of aggregation directly but rather uses experimental correlations for aggregation and disaggregation rates to account for the effects of aggregation on the bulk. To find the aggregation rate, a series of experiments on RBC sedimentation due to gravity is designed. In these tests, aggregated RBCs (rouleaux) tend to settle faster than single RBCs and, due to low shear stresses, disaggregation is very low and can be neglected. A high-speed camera is used to acquire video-microscopic pictures of the process. The size of the aggregates and their velocities are extracted using image processing techniques. For image processing, a general Matlab program is developed which can analyze all the images and report the velocity and size distribution of rouleaux.

An experimental correlation for disaggregation rate is found using results from a previous steady-state Couette flow experiment. Aggregation and disaggregation rates from

these experiments are used to complete the PBM model. Pressure-driven channel flow experiments are then used for the final validation of the model. Comparisons of the apparent viscosity of whole blood in previous experiments show reasonable agreement with the developed model. This model fills a gap between micro-scale and macro-scale treatments and should be more accurate than traditional macro-scale models while being cheaper than direct treatment of RBCs at the micro-scale.

Table of Content

List of Figures

List of Tables

Nomenclature

Parameters	Definition	Units
α	Volume fraction	
$\dot{\gamma}$	Shear rate	s^{-1}
Γ	Collision rate	$m^3.s^{-1}$
μ	Dynamics viscosity	Pa.s
μ_l	Intrinsic Viscosity	Pa.s
μ_{app}	Apparent viscosity	Pa.s
μ_f	Plasma viscosity	Pa.s
μ_{rel}	Relative viscosity of blood to plasma viscosity	
ρ	Density	$Kg.m^{-3}$
σ	Shear stress	Pa
$\sigma_{A\kappa\lambda}$	Cross sectional area between κ class and λ class	m^2
χ	Density ratio of plasma to red blood cells	
ω	Fluid vorticity	s^{-1}
$\omega_{\kappa,\lambda}$	Breakage frequency of particle in class κ to create class λ	s^{-1}
Δt	Time step in numerical model	s
Δt_c	Collision time step	s
Δt_f	Fluid time step	s
Δt_p	Particle time step	s
Δx , Δy	Grid size in numerical model	m
ΔP	Pressure drop	Pa
Ω_A	Aggregation Rate	$ml.s^{-1}$
Ω_B	Break up (disaggregation) rate	s^{-1}
a , b and c	Ellipsoid semi-axis on $\hat{x}$, $\hat{y}$ and $\hat{z}$ axis	m
d	Diameter	m

g	Gravity	$m.s^{-2}$
$\bar{g}$	Mean particles relative speed	$m.s^{-1}$
κ	Particle class (size)	
k	Boltzmann constant	$J.K^{-1}$
m_κ	Mass of the particles in size κ	Kg
n	Number density	m^{-3}
r_κ	Radius of particle κ	m
s	Sticking probability	
t	Time	s
u, v	Velocity in two direction	$m.s^{-1}$
v_κ	Volume of a particle in size κ	μm^3
$\bar{v}$	Mean particle speed	$m.s^{-1}$
x	Particle position	m
A_κ	Area of a particle in pixels	$Pixels^2$
AAS	Average aggregate size	$Pixels^2$
B	Birth of a particle	$particles.m^{-3}s^{-1}$ or $Kg\,m^{-3}s^{-1}$
D	Death of a particle	$particles.m^{-3}s^{-1}$ or $Kg\,m^{-3}s^{-1}$
E_p	Young's modulus of the particle	Pa
F_G	Gravitational force	N
F_D	Drag Force	N
F_L	Lift Force	N
F_{VM}	Virtual Mass (Added mass) force	N
F_b	Basset force	N
F_{pl}	Source term coming from reaction force of a particle on the base liquid	N
H_t	Hematocrit - RBCs percentage in plasma (volume fraction)	

L	Length	m
Np	Number of particles	
P	Pressure	Pa
Pe	Peclet number	
P_κ	Perimeter of a particle in pixels	Pixels
Q	Volume flow rate	$\mu l.min^{-1}$
R	Radius of a channel	m
Re	Reynolds number	
S	Source term	
T	Temperature	^oC
U	Whole blood flow velocity	$m.s^{-1}$
Y	Effect of base fluid on aggregation and disaggregation	
$[\,]_i$ $[\,]_j$	Subscript i and j are used for showing grid location	
$[\,]_\kappa$ $[\,]_\lambda$	Subscript κ and λ are used for showing class of particles	
$[\,]_p$	Subscript p represents particle	
$[\,]_f$	Subscript f represents fluid	
$[\,]_A$	Subscript A represents aggregation	
$[\,]_B$	Subscript B represents break up or disaggregation	
$[\,]^n$	Superscript *n* represent time marching in the numerical discretization	
$[\,]^m$	Superscript *m* represent semi implicit time marching in the numerical discretization	

List of Acronyms

AAS	Average Aggregate Size
CCD	Charged-Coupled Device
CFD	Computational Fluid Dynamics
CFL	Cell-Free layer
DPD	Dissipative Particle Dynamic
BD	Brownian dynamics
EDTA	Ethyleneiaminetetraacetic
ESR	Erythrocyte Sedimentation Rate
GUI	Graphical User Interface
Ht	Hematocrit
LBM	Lattice Boltzmann Method
MC	Monte Carlo method
MD	Molecular Dynamics Method
N-S	Navier-Stokes
PBE	Population Balance Equation
PBM	Population Balance Model
PBS	Phosphate Buffered Saline
PDE	Partial Differential Equation
PDMS	Poly-Di-Methyl-Siloxane
PIV	Particle Image Velocimetry
RBC	Red Blood Cell
TDMA	Tridiagonal Matrix Algorithm
SIMPLEC	Semi-Implicit Method for Pressure Linked Equations Corrected
2D	Two-dimensional
3D	Three-dimensional
µPIV	Micro Particle Image Velocimetry

Chapter 1

Introduction

1.1 Introduction

Blood is a complex fluid with a unique set of properties. It is well known that blood behaves as a non-Newtonian fluid with a viscosity that varies with fluid state and history [2]. This behaviour is related to the particulate nature of blood components, as it is composed of a Newtonian base fluid (plasma) with suspended particles (red and white blood cells and platelets). Red blood cells (RBCs) are the most abundant cells in blood, hence changes of blood behaviour in microcirculation originate mostly from this component. White blood cells, platelets and other component of blood have a much smaller effect on overall blood rheology [3].

RBCs are deformable biconcave discs and are about 7 microns in diameter and 2 microns in thickness. RBCs tend to clump together and form into regular stacks called rouleaux, as shown in Figure 1.1. These stacks are not static, and constantly move and break apart. This phenomenon is called aggregation. This is a healthy part of blood function and can be viewed as a natural process preserving a more constant set of properties in the blood circulation in human body [4]. RBC aggregation occurs in microcirculation where low shear rates are present but does not occur under normal physiological conditions in large arteries where high shear rates are present.

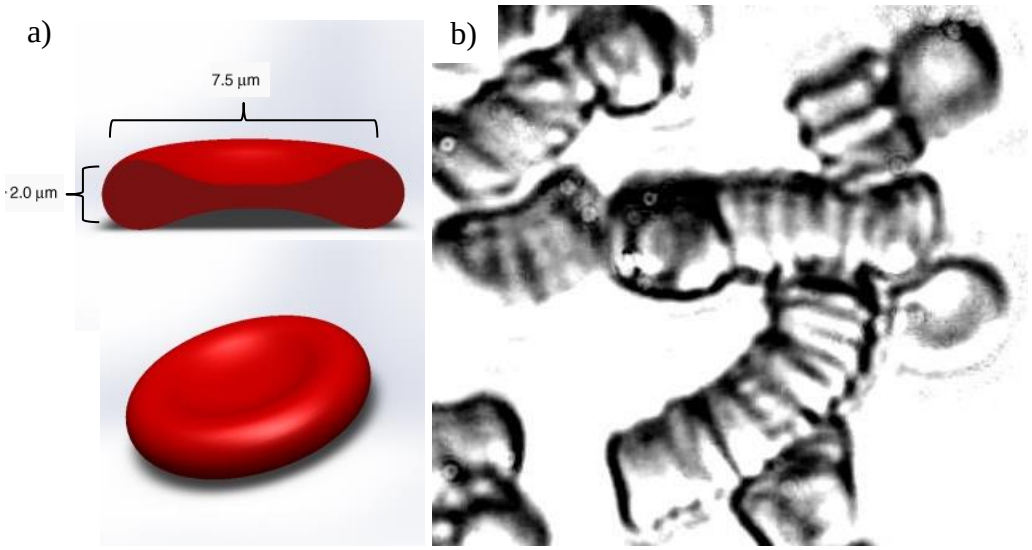

Figure 1.1: a) Geometry of single RBC and b) examples of rouleaux formed by red-blood-cell aggregation.

The complexity of blood behaviour has been the focus of numerous studies, specifically in the numerical simulation of this complex fluid. Currently there is an interest in numerical models that can predict the viscosity of blood, positions and size of rouleaux, and flow velocity profiles in different geometries in microcirculation [6 - 18]. These studies aim to develop a mathematical model of RBC interaction that can be used to numerically model the dynamics of blood flow. Three major applications of these models are:

1- Understanding the formation of rouleaux in different diseases like infections, cancers, and autoimmune diseases [3].
2- Understanding the migration of RBCs and the distribution of RBCs in microcirculation for drug delivery purposes [6].
3- Blood-flow distribution in bifurcations and microcirculation [7].
4- Predicting the viscosity of blood in microcirculation in healthy and diseased conditions [6].

In this work, the population-balance equation (PBE) is used to model the evolution of RBCs. This equation has the ability to simulate aggregation and disaggregation of RBCs in blood flow. It is coupled with the Navier-Stokes equations in order to study the effects that the base plasma flow and the aggregation of RBCs have on each other. This model also uses the mass and momentum conservation law to find RBC and rouleaux velocities and positions. This model needs two experimental correlations for the aggregation and disaggregation rate (Ω_A and Ω_B) to be a closed complete model. In this study different experiments including RBC sedimentation, Couette flow and channel flow are used to empirically find these parameters.

1.2 Motivation and Research Question

Several studies in microcirculation [19, 20] have shown that elevated red blood cell aggregation can reduce blood flow in microcirculatory vessels to varying degrees. It has been suggested that this may causes blockage of precapillary vessels [8]. One study shows increase in aggregation causes memory loss in rats [9]. Furthermore, changes in normal blood flow circulation, which occurs in many blood related diseases and disorders such as malaria, sickle cell anemia, and diabetes, may also lead to serious organism disease or death [21]. Blood-flow

features under healthy conditions and in various diseases and disorders can provide vital information for understanding many biological processes such as increase in blood viscosity and pressure drop for such diseases. This has motivated a scientific effort in blood-flow research which can be divided in to experimental and numerical modelling. Experimental studies have shown the complexity of blood flow, however, they have so far not been able to predict complex blood behaviour in microcirculation. Several numerical studies have also attempted to model the complex behaviour of blood. However, the majority of these studies do not accurately consider all microscopic properties of blood.

Numerical simulation of blood flow can be categorized into three main groups, each of these groups applies to one measurement scale. The first category is macro-scale modelling. In this type of simulation, blood is considered as a complex fluid with variable viscosity (non-Newtonian). Several non-Newtonian formulations have been used in recent years [3, 22-24]. Macro-scale modelling is a powerful tool to understand blood flow in different geometries but it has a disadvantage. This model does not consider RBCs as a distinct material therefore it is not able to properly simulate RBC transport and its effect on the flow (*e.g.* oxygen transfer, microcirculation, cell-free layer, etc.).

Another category is microscale modelling, which accurately and directly tracks individual cells and deformations of RBCs. Simulations of this type are challenging due to the small length scales involved with adhesion between cells and small deformation of RBCs. The diameter of a typical cell is on the order of 10 μm, while adhesion between cells occurs at distances on the order of 10 nm. These simulations are computationally intensive due to the required small length scales, tracking of individual protein bonds between cell surfaces that are responsible for adhesion, and tracking of the deformation of individual sections of discretized cell surfaces [25-31]. Considering the 3D biconcave shape of the RBC is essential for these type of simulations as the contact surface between cells is an important parameter in this type of simulations. Another parameter that changes with the deformation of the cells is the drag and lift coefficients. Looking at the literature there seems to be a lack of information on these parameters for RBCs.

The third category is mesoscale modelling, which uses continuum models for RBCs, treating then as a fluid that is distinct from the background plasma [32-34]. In the same category of the computational models, Smoluchowski coagulation theory can be added. This model is used to determine the distribution of aggregate sizes [14, 35-37] without any flow. These models simulate the effect of large numbers of aggregating cells, rather than directly treating adhesion between discrete, individual cells. Instead, these models rely on empirically determined constitutive equations to describe the interaction between the cells and the base fluid [10].

Looking in the literature, it seems that only Owens' [11] model can simulate blood flow in microcirculation by using a modified population-balance method. Using the population-balance equation enables this model to estimate the local viscosity by predicting the average aggregate size in the domain. This model is able to reproduce the thixotropic response of blood [38]. As it does not track the RBC phase, it can be considered as a macroscale model. Owens' model does not consider RBCs as separate particles and thus it cannot simulate micro-properties of blood, including RBC interaction.

From the above discussion, it can be concluded that, in the numerical simulation of blood flow, the following limitations should be kept in mind:

1- Increasing the number of RBCs in micro-scale simulation increases the computational time.
2- Tracking of the deformation of individual RBCs in blood flow demands an enormous amount of computation time and limits the number of particles in the simulation (order of 10 particles [18, 39]).
3- Numerical modelling of the adhesion force between RBCs limits the simulation to a finite number of RBCs [10].
4- Modelling aggregation and disaggregation of RBCs is necessary to correctly find the thixotropic response of blood.
5- There is no definition of drag and lift force of the biconcave shape of RBC and more complications can arise when considering the forces on deformable particles. For complete numerical simulation of blood all the forces on RBCs should be considered.

Figure 1.2 compares length and time scales that are treated by the three classes of models and provides examples of notable members of each family. It can be seen that the models that directly treat smaller length scales also cover smaller numerical time scales. Macro-scale modelling has a reasonable time scale for more practical problems but it greatly simplifies the physics of the problem. It can be seen that the population-balance method covers smaller length scales, while using the same time scale as macro-scale models. It also provides some representation of the microscopic physics.

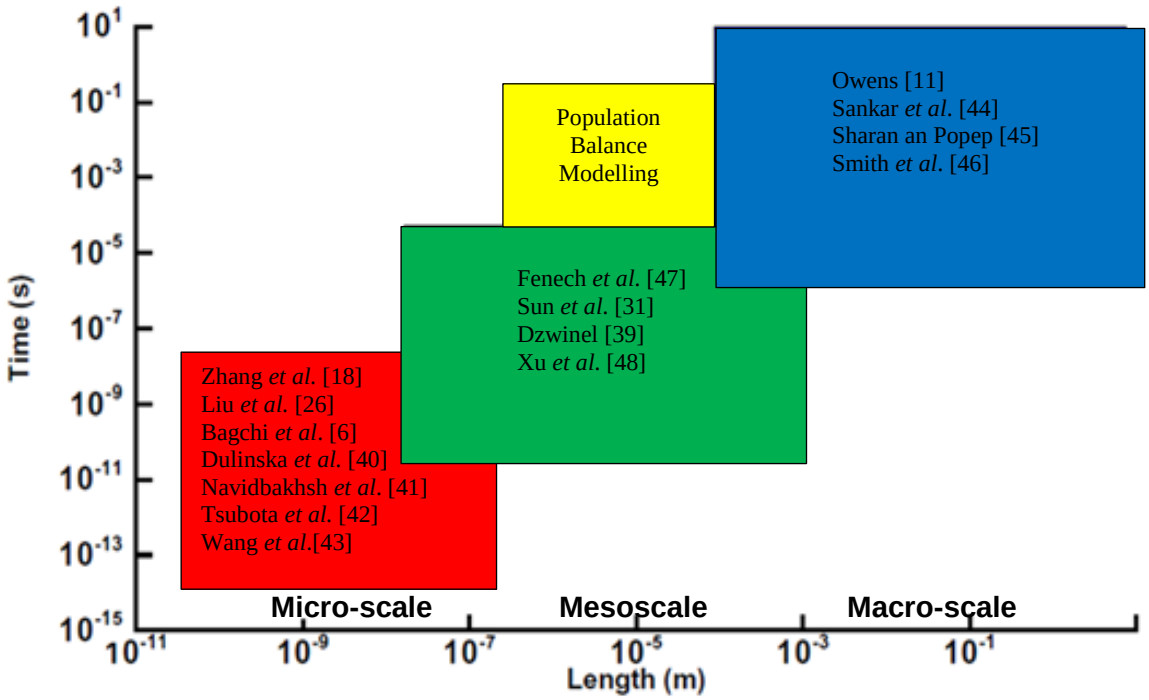

Figure 1.2: A schematic plot of various spatiotemporal scales covered by different computational techniques.

1.3 Research Approach

Due to the above mentioned limitations, there appears to be a gap in mesoscale modelling due to the dependence of these simulations on the number of simulated RBCs. In the same way, modelling aggregation and disaggregation also increases the computational cost and decreases the number of simulated RBCs. In this research, it is proposed to couple a population-balance model with the Navier-Stokes equations. This method is able to model agglomeration and breakage in multiphase fluid mechanics. The population-balance method has been used in numerous multiphase flow simulations found in the literatures, but its application to blood flow and RBCs has not been considered until now. This model's numerical cost is independent of the number of RBCs. It uses a combination of theory and experimental correlations to find RBCs aggregation or disaggregation. The result is that modelling the aggregation process is not computationally expensive. It is important to note that the model is still limited by limitations number 5 in the previous section and there is a lack of information on forces applied on red blood cells in the literature. In order to circumvent this limitation, RBCs are considered as elliptical for the current model.

Population-balance modelling is based on the conservation of the population of the RBCs in term of class sizes (RBCs distributed in each rouleaux size). This model sacrifices microscopic physics of aggregation to get a more macroscopic representation of blood. It compensates for this deficiency by using an experimental correlation for aggregation and disaggregation. This type of modelling also depends on a complete understanding of all applied forces on individual particles. Drag, buoyancy, gravity and lift forces are some of the important forces which are applied to a particle in a flow. This model and these forces are discussed in Chapter 3.

Finding the aggregation and disaggregation rate is the first step to building this model, therefore, several experiments are designed to estimate these parameters. It is known that aggregation depends most strongly on hematocrit and disaggregation depends on the shear rate [3]. In order to find the aggregation rate as a function of hematocrit, a sedimentation experiment is conducted. In this test, aggregated RBCs tend to settle faster than single and smaller rouleaux. Due to low shear stress, disaggregation is very low and can be neglected. A high-speed camera is

used to acquire video-microscopic pictures of the process. The size of the aggregates and their velocities are extracted using image processing techniques. The same procedure is done for a Couette flow to find the disaggregation rate as a function of shear stress. Couette flow presents a constant shear stress, therefore, in steady-state, a balance between aggregation and disaggregation rate is expected. Further experiments on channel flow are conducted to tune and validate the present model.

1.4 Research Contribution

The main contribution of this research is a comprehensive model that is capable of predicting RBC rouleaux size and their velocities in microcirculation. This model is also a useful tool to understand the effects of aggregation on blood flow in microcirculation in different geometries. For example, Figure 1.3 shows a network of blood vessels of healthy human sublingual microcirculation. None of the previously mentioned models are able to simulate such situations accurately. The population-balance model, which is used in this research should be able to model the blood flow directly and simulate this geometry in an acceptable simulation time.

Other contributions of this work are related to developing this model. The aggregation and disaggregation rates are the two main obstacles for this model which are tackled in this work. Three main experiments are conducted and analyzed to find these parameters. To analyze these experiments, a Matlab code with a simple GUI is developed which is a very helpful tool for researchers to analyze their results. Using this tool and the theory presented in Chapter 2, the aggregation and disaggregation rates are found. These parameters are also useful for other researchers who use the Owens [11] or similar models.

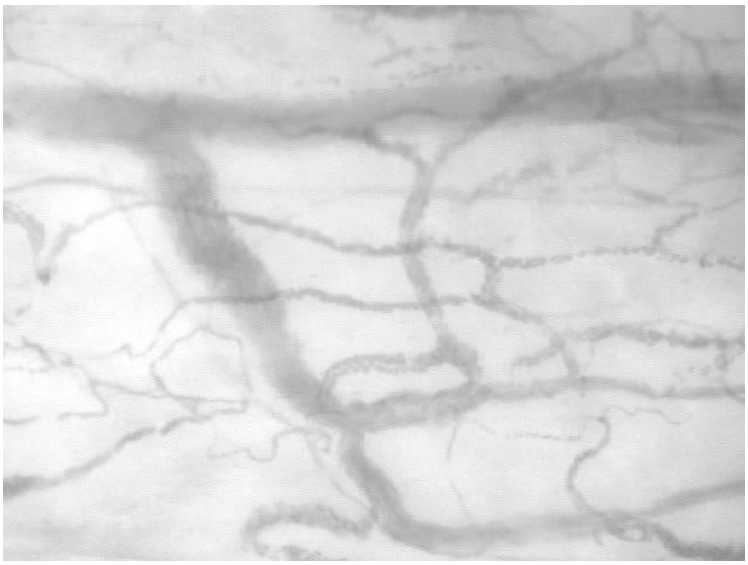

Figure 1.3: Network of blood vessels in microcirculation in a healthy human sublingual microcirculation.

1.5 Thesis Structure

In this chapter, an introduction to this project, the research question and motivation are presented. Next, a review of several experimental and numerical studies in this field is presented in Chapter 2. In Chapter 3, the population-balance equation is introduced and the background theory of the model is discussed. In Chapter 4, details on experimental procedures and image processing techniques are given. In Chapter 5, the proposed computational model is presented, showing how the Navier-Stokes equations are coupled with the population-balance equation. Chapter 6 introduces the procedure to find aggregation rates from the experimental study and its implementation in the numerical model. The comparisons of the numerical results with experimental results are also presented in this chapter. Finally in Chapter 7, the conclusion of this research, the main contributions of this work are discussed along with suggestions for future works.

Chapter 2

Literature Review

2.1 Blood Physiology

The primary function of blood is to supply oxygen and nutrients to cells and tissues throughout the body and to remove waste products. Blood is a concentrated suspension, containing RBCs (or erythrocytes), white blood cells (or leukocytes), platelets and blood plasma with some suspended macromolecules and other chemical elements [12]. The blood volume fraction of RBCs (Hematocrit, H_t) for a healthy individual is approximately 45%. White blood cells occupy less than 1% of the volume, while the rest of the volume consists of the plasma, which has Newtonian characteristics. Therefore, RBCs are by far the largest contribution to the non-Newtonian characteristics of blood when treated as a single fluid [3].

RBCs are highly deformable particles and have a tendency to aggregate under low shear conditions and in the presence of certain plasma proteins (*e.g.* fibrinogen) or other long chain macromolecules (*e.g.* dextran) [7]. Blood aggregation was first observed by Fåhraeus in 1921 and is described by Goldsmith *et al.* [49], where the relationship between the aggregate formation and the sedimentation speed is investigated. Fåhraeus's research showed that the structure of aggregates in healthy and non-healthy individuals is clearly different [50]. Behaviour of RBC interactions changes in different flows. Similarly, the behaviour of a blood flow changes due to RBC interactions. This phenomena causes a complex behaviour of blood flow which is discussed in the next section.

There are two theories that try to explain the mechanism of RBC aggregation. In the first theory, aggregation is explained by the surface adsorption of long-chain macromolecules (fibrinogen or dextran) by the adjacent RBCs membrane. This adsorption links RBCs leading them to bridge together. In the second theory, the aggregation mechanism is explained by a reduction in the concentration of macromolecules in the vicinity of RBCs due to the imbalance between the loss of polymer configuration entropy and the adsorption energy. This difference in concentration results a reduction to the local osmotic forces. This force causes the inter-cellular fluid to move away, thereby bringing the RBCs together and increasing their tendency to bridge together [3].

2.2 Blood Flow

The behaviour of blood flow in a vessel changes with the size of the vessel and the composition of the blood. In *vitro* experiments of blood flow in glass tubes with diameters ranging from 3−4 μm to 1000 μm, showed a dependence of the apparent blood viscosity on the tube diameter, RBC hematocrit, cell aggregability and flow rate [51-53]. As mentioned previously, blood shows non-Newtonian characteristics in microcirculation where low shear rates are present but does not show the same characteristics under normal physiological conditions in larger arteries where high shear rates are present [10]. Before going further into the microscopic details of blood flow, macroscopic characteristics of blood as a liquid are discussed. In the next section a selection of important studies on the blood viscosity are summarized.

2.2.1 Blood Viscosity

The viscosity of blood is an important parameter in the fluid dynamic and physiological behaviour of blood. Under many disease conditions, the viscosity of the blood increases. The microscopic characteristics of blood results in variation of viscosity in a flow domain. To measure a single value for this variable viscosity, researchers use the apparent viscosity, μ_{app}. An apparent viscosity (or effective viscosity) of blood is introduced by invoking the Poiseuille law for Newtonian fluid in a circular pipe as

$$\mu_{app} = \frac{\pi R^4}{8L}\frac{\Delta P}{Q}, \tag{2-1}$$

where ΔP is the pressure drop along a length L of the pipe, Q is the volume flow rate, R is the radius of the pipe. This viscosity acts like an average viscosity of a Newtonian fluid in a domain. The relative apparent viscosity, $\mu_{rel} = \mu_{app}/\mu_f$, is defined as the ratio of the apparent viscosity, μ_{app}, and the viscosity of pure plasma, μ_f.

The apparent viscosity of blood is greater than that of the plasma, mainly due to the presence of RBCs. The extent of the difference in viscosity depends on aspects such as shear rate, hematocrit, temperature, tube diameter, and RBC aggregation (which depends on blood flow history). To determine the effects of shear rate, hematocrit, and temperature on blood

viscosity, Rand *et al.* used a micro cone-plate viscometer with normal human blood [54]. In their study, the blood is reconstituted to a desired hematocrit. Brooks *et al.* also investigated the effects of shear rate, hematocrit, and cell aggregation on apparent viscosity of several suspensions of human RBCs at a constant temperature using a rheometer equipped with concentric cylinders [55]. In Figure 2.1, the apparent viscosity of whole blood is plotted versus shear rates. This figure shows the shear-thinning behaviour of blood using rotational viscometers. These data are used later in this study to validate the results.

Most published works on the subject of measuring the viscosity of blood are in steady-state condition. Only Bureau *et al.* used transient condition and found that human blood viscosity has a time-dependent response [38]. The time dependence of rheological properties arises from the time required for the disaggregation and aggregation and microstructures of rouleaux to form.

Bureau *et al.* [38] employed a Couette rheometer to expose blood to a transient shear flow. In Figure 2.2 (A) and (B) shear stress hysteresis curves for normal human blood are shown. In experiment (A), they reached a maximum shear rate of $\dot{\gamma}_{\max} = 0.12025 \ \ s^{-1}$ at $t_0 = 6.5 \ s$ and in experiment (B) they reached $\dot{\gamma}_{\max} = 1.0234 \ \ s^{-1}$ at $t_0 = 23.8 \ s$. In both cases a residual non-zero shear stress can be seen at the end of the cycle which indicates that blood is viscoelastic and that the stress depends on the entire deformation history and not just the instantaneous rate of deformation [56].

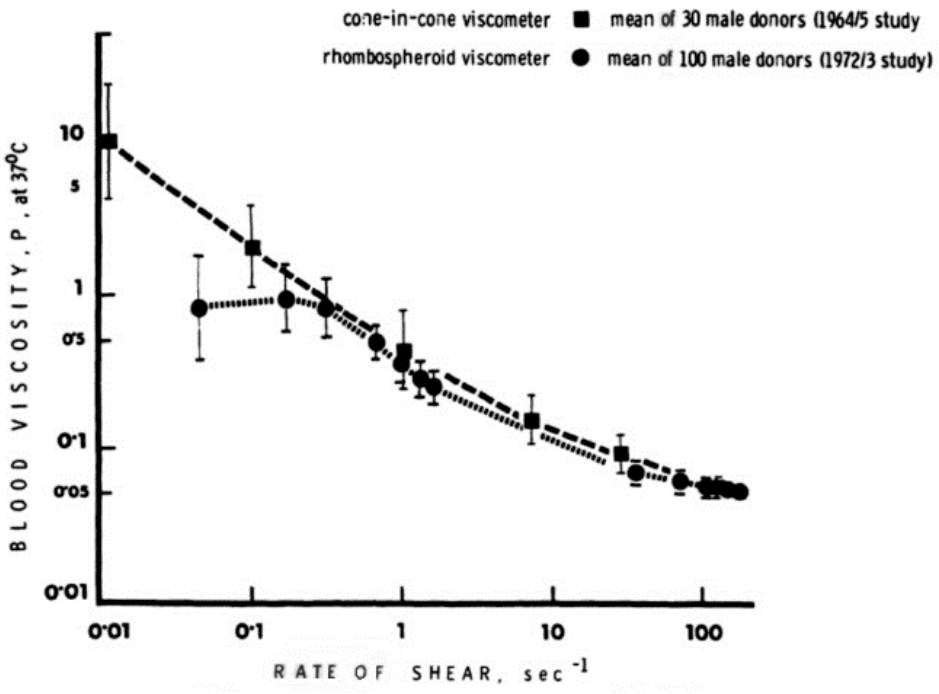

Figure 2.1: Viscosity of whole blood measured over a range of shear rates in rotational viscometers at 37° C using cone-in-cone and rhombospheroid viscometers [57].

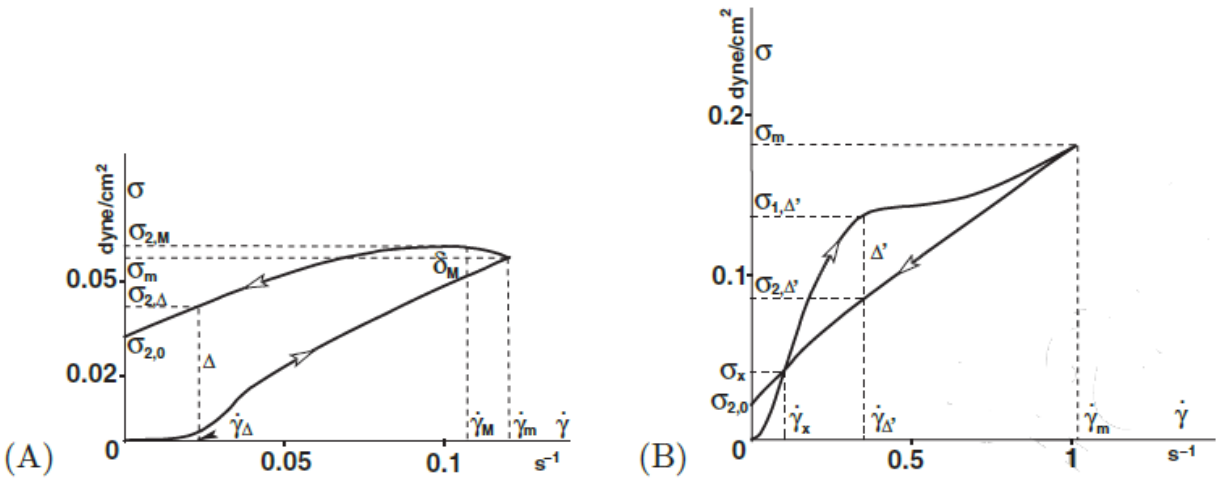

Figure 2.2: Shear stress (σ) hysteresis response for normal human blood at low shear rate. Reproduced from Bureau et al. [38]. (A) $\dot{\gamma} = 0.0185t$ for $0 \le t \le 6.5s$ and $\dot{\gamma} = 0.0185(13-t)$ for $6.5 \le t \le 13s$. (B) $\dot{\gamma} = 0.043t$ for $0 \le t \le 23.8s$ and $\dot{\gamma} = 0.043(47.6-t)$ for $23.8 \le t \le 47.6s$.

2.2.2 Cell-Free or Cell-Depleted Layer

Another microscopic phenomenon that changes blood macroscopic characteristics (*e.g.* viscosity) is the cell-free layer (CFL). In small capillaries, the cell-free layer is a near-wall layer of plasma that is absent of red blood cells. This layer exists because RBCs are subject to migration to the centre of the vessel in Poiseuille flow. This was explained by a lift force caused by the shape and rotation of RBCs near the vessel wall [58]. On the local scale, it has been shown that aggregation tends to blunt velocity profiles [52, 59] which can increase the apparent viscosity. However, aggregation leads to increase in migration of RBCs to the center, which results in a region of low cell density near the wall. Other names for the cell-free layer are the cell depleted layer [52] or cell poor layer [60]. As well as being dependent on aggregation, the width of the cell-free layer is also affected by the hematocrit, red blood cell deformability, vessel diameter, flow rate and the amount of time allowed for the cell-free layer to form [53, 61, 62]. Figure 2.3 shows a schematic of the effects of the cell-free layer on the flow velocity profile.

A paper by Fåhraeus and Lindqvist is one of the first publications that studied the cell-free layer [63]. They used a glass capillary tube viscometer and found that apparent viscosity increased with the tube diameter up to about 0.3 mm at which point apparent viscosity reached a plateau (Figure 2.4). This effect is known as the Fåhraeus-Lindqvist effect. The results were attributed to migration of RBCs toward the centre of the tube and the formation of a cell-free layer of plasma near the tube walls [63].

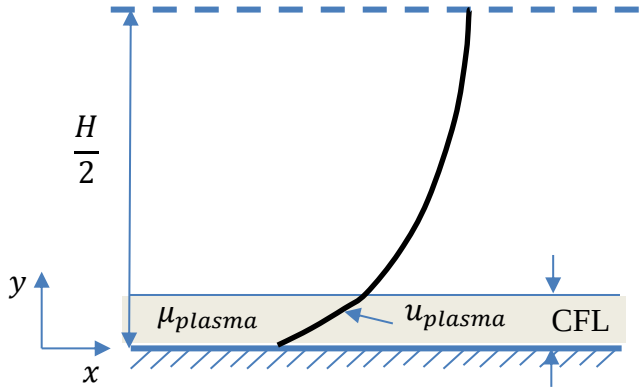

Figure 2.3: Schematic of a typical velocity profile of channel flow using blood.

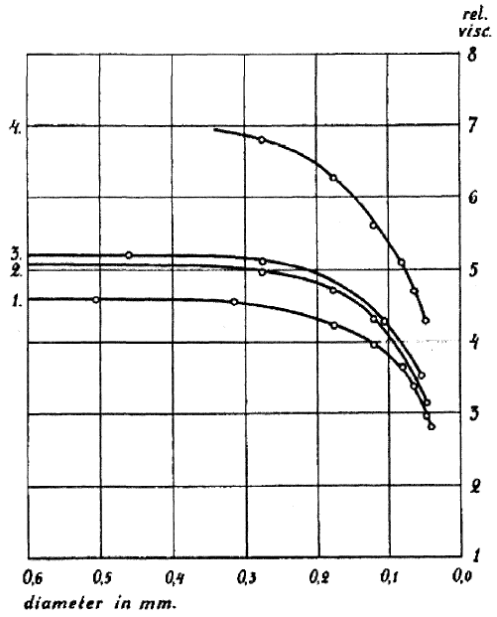

Figure 2.4: Relative viscosity of blood for four samples versus the tube diameter reproduced from Fåhraeus et al. [63].

2.3 Experimental Techniques for Blood in Microfluidics

The basic microscopic and macroscopic characteristics of blood are introduced in the previous section. In this section, experimental techniques that can be used in this study are explored. Blood circulation and blood flow have long been an interesting topic in biomechanics, with an extensive history of experimental studies. Early experimental studies on microcirculation

were performed in dynamically similar systems on the centimeter scale [64, 65] or in glass capillary tubes [66]. Dynamically similar systems, scaled using principles of continuum mechanics based on the Reynolds number and Womersley number are useful when studying relatively simple situations such as the shear force acting on a single cell [65] or more complex problems such as transient flow in non-uniform geometries [67]. However, the validity of these scaling approaches, as well as the continuum assumption, break down when discrete RBCs or cell-cell interactions gain significance in microcirculatory dynamics.

Although there are many experimental studies on blood, this literature review is confined to three techniques. First, an introduction to microfluidics and their application to in *vitro* studies of blood is given. Next, a literature review of RBC visualization and image processing is presented. Finally, several studies on aggregate size measurement are presented. These experiments are the basic tools required to measure aggregation and disaggregation rates later in this study.

2.3.1 Microfluidics and Microcirculation

The microvascular system consists of various veins, arteries, channels and capillaries, some of which are embedded within or around internal organs [4]. These vessels are defined as microcirculation for any vessel less than 300 micrometers in diameter. Generally, microcirculatory is the range of blood vessels where the Reynolds and Wormersly numbers are significantly less than 1 and the viscous stress and pressure gradient have the predominant influence on the flow [68].

Microfluidic devices are component systems of micro scale which allow manipulating gases, liquid and cells in a flow. These systems usually work within a cross sectional dimension on the order 10 to 100 μm. Microfluidics technology is often used to mimic microcirculation and microvasculature networks.

In microfluidics, data is usually collected optically. Construction of microfluidic channels for early studies of blood flow was accomplished by etching glass or silicon substrates [69]. The lengthy fabrication processes likely limited widespread use of these methods until Polydimethylsiloxane (PDMS) based rapid prototyping gained popularity [70]. PDMS has become the microfluidic chip material of choice in most laboratories due to its ease of use,

optical properties, low price, and low volumes of fluids within microfluidic channels. However, there are two main limitations when PDMS is used. First, PDMS chips are usually fabricated with a rectangle cross section—creating a circular channel is challenging. The second limitation is that PDMS material is inherently highly hydrophobic [71]. This is different from blood vessel wall characteristics. Using Oxygen plasma etching removes this behaviour of PDMS but it is not a permanent solution and the hydrophobic characteristics of PDMS return after 2-3 days [72]. Further details on the fabrication of microfluidics devices using PDMS is provided in Chapter 3.

2.3.2 Visualization of Blood Flow and RBC Aggregates

Being able to use transparent experimental set-ups to directly view and analyze aggregation allowed a wide use of computerized visualization techniques. Shiga *et al.* were one of the first research groups to use particle analysis software with a video camera to capture either human or rat RBC aggregate formation at different shear rates within a transparent cone-plate viscometer [73, 74]. Figure 2.5 shows example results from their experiment, where the experiment starts with dispersed RBCs (Figure 2.5 A). Then rouleaux are formed (Figure 2.5 B) and due to a low shear state, they get larger (Figure 2.5 C). Finally, due to gravity they settle and move outside the video domain (Figure 2.5 D). Similarly, Chen *et al.* [75, 76] used image processing methods for analyzing aggregation in channel flow in *vitro*. Later, Bishop *et al.* used image analysis software to examine RBC aggregate size in *vivo* [59]. Their research is discussed further in the next section.

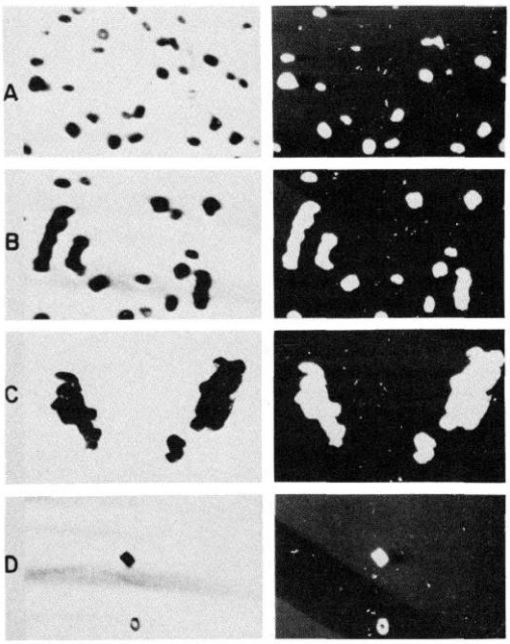

Figure 2.5: Images of RBC aggregation with time at a shear rate of 7.5 s^{-1} and hematocrit of 0.26% [73].

Micron-resolution particle-image velocimetry (µPIV) is a flow-measurement technique offering full-field measurement with high spatial and temporal resolution. Modern µPIV systems have been recently used to determine the velocity profiles of blood flowing through microchannels [78-82]. RBCs themselves or fluorescent micro particles can be used as a tracer (Figure 2.6). A double pulsed camera or high-speed camera can be used to acquire images using very short time steps [77]. Comparison of captured images are used to measure the velocity of each particle.

Another family of methods that can visualize RBC aggregates are laser aggregometry techniques which employ continuous recording of backscattered or transmitted laser light signal from a suspension of RBCs [83-85]. A similar method, called “light intensity” quantifies the aggregation process under dynamic conditions by measuring the changes in the transmitted light intensity [86, 87].

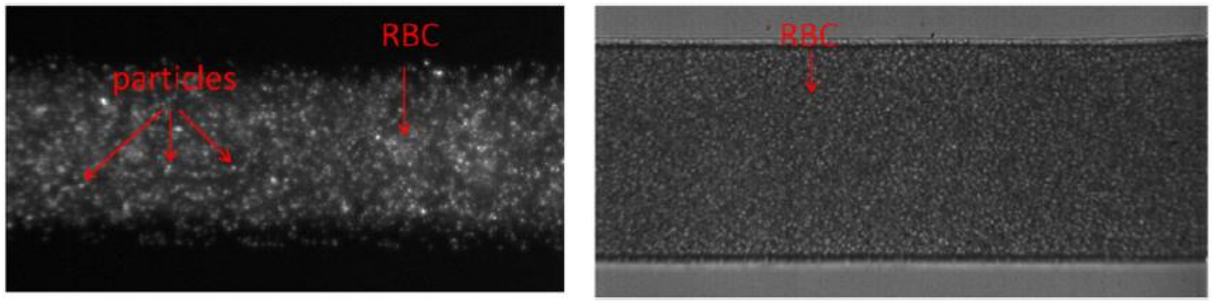

Figure 2.6: The resulting images from the two methods of μPIV. Pulsed images using fluorescing tracer particles are shown on the left, and the high-speed camera images using RBCs themselves as tracers shown on the right [77].

In this study, a sequential video-microscopic system is used to capture different aggregate sizes and their velocity in different geometries. Using the high-speed camera allows one to capture aggregation and disaggregation of RBCs during flow movement in high resolution. Using image processing techniques, such as filtering and background removal, a clear picture of RBCs aggregating can be obtained.

2.3.3 Aggregation Size

The first step to find experimental expressions for aggregation and disaggregation rate, Ω_A and Ω_B, is to measure the range of aggregate sizes in a domain. By measuring the change of number of rouleaux in a specific size under varying conditions (*e.g.* shear rate) a correlation for these parameters can be developed. In this section an overview of similar works that have attempted to find empirical models for rouleaux size or aggregation and disaggregation rate is given.

Murata and Secomb suggested a kinetic equation that determined the number of rouleaux composed of a given number of RBCs and the average number of RBCs per rouleaux size in shear flow [36]. The kinetic equation utilized a sticking probability function for adhesion of one cell to another. Parameters that could be varied in the equation included shear rate, hematocrit, and rate constants related to a collision, sticking probability, and disaggregation. Beginning with a state of complete disaggregation and with all parameters held constant except reduced shear rate (shear rate, normalized by critical shear rate $\dot{\gamma}_s = 5.86 s^{-1}$) they measured the rouleaux size versus time. Figure 2.7 shows that the average rouleaux size increased with reduced time (time,

normalized by critical shear rate and other parameters) to approach an equilibrium, and that higher shear rates approached equilibrium more quickly than lower shear rates, with the equilibrium value being lower for higher shear rates.

Chen and Huang also proposed a model for rouleaux formation and breakage which incorporated expressions for the rates of aggregate formation and degradation based on rouleaux size as a reversible kinetic equation for colloid coagulation [88]. Parameters of the model were chosen that best matched the experimental data for rate of rouleaux formation. An example of the agreement between their model and experimental results is shown in Figure 2.8.

Chen *et al.* used a direct imaging study of RBC aggregation in channel flow [75, 76]. They used blood with a hematocrit of 10% in various solutions of plasma and dextran*. A rectangular chamber with a 40 μm gap was used in their study. After image processing, the distribution of aggregate size (number of cells per aggregate) was determined for numerous values of average fluid shear stress and plotted as reported in Figure 2.9. Here, the value of aggregate size indicates the average size of aggregates in a particular size range (*e.g.* 1.5 indicates aggregates of 1-2 particles, 3 indicates aggregates of 3-4 particles, etc.), against the percent of cells in aggregates.

Bishop *et al.* [89] used image processing to digitize video images of rat RBCs and aggregates in rat venules ranging from 27 to 107 μm in diameter with and without aggregation. Although in normal rat blood, RBCs do not aggregate, the researcher induced aggregation with the addition of dextran 500. For both types of flows, the particle dimensions were larger in the centre of the vessel than near the walls (lower shear rate in center). Distributions of individual clusters in Figure 2.10 show that the maximum lengths and widths for dextran-treated blood are about 50% larger than those of normal blood [89].

* Dextran molecule is used to promote RBC aggregation

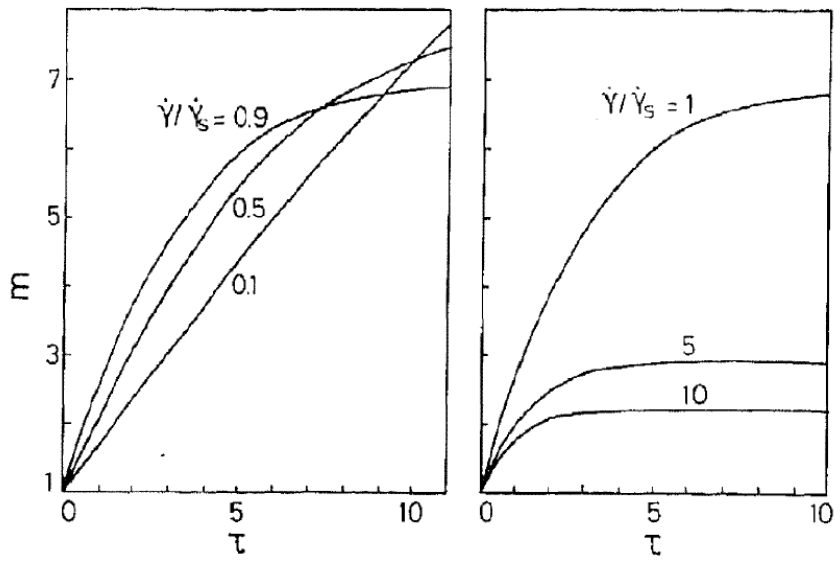

Figure 2.7: Average size of rouleaux as a function of reduced time, τ, with the reduced shear rate, $\dot{\gamma}/\dot{\gamma}_s$, as a parameter [36].

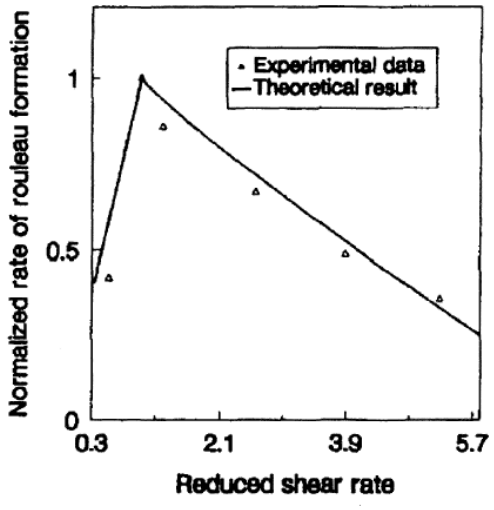

Figure 2.8: Variation of normalized rate of rouleaux formation with reduced shear rate [88].

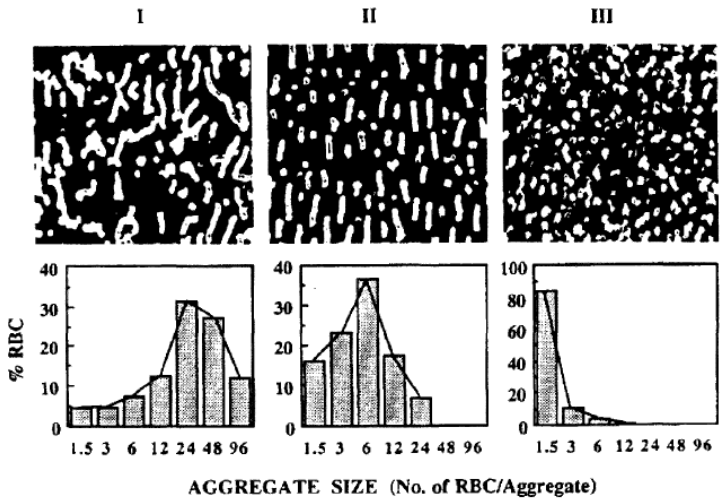

Figure 2.9: Images of human RBC aggregates and corresponding aggregate size distribution at three levels of shear stress including (I) 0.125, (II) 0.5, and (III) 2.0 dyne/cm^2 [75].

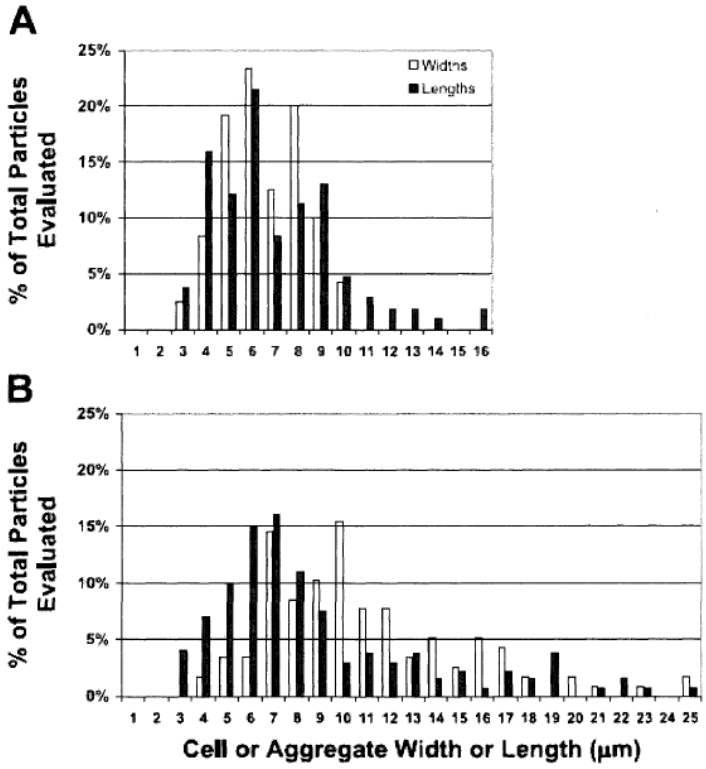

Figure 2.10: Histogram plots of the entire population (n = 1,250) data for RBC or aggregate width and length for normal (A) and blood (B) dextran-treated [89].

2.4 Numerical Approaches for Blood Flow Modelling

In this section, several approaches that researchers have chosen to model blood flow using computational fluid mechanics are reviewed. Blood flowing in large vessels with a characteristic diameter greater than approximately 1 mm is often modelled as a Newtonian fluid with a constant viscosity due to the high shear rates and therefore less aggregation in such vessels [90]. However, in vessels with a diameter smaller than 1 mm non-Newtonian properties of blood are likely to be of importance in blood flow modelling [91]. In this regime, continuum modelling of blood flow may still provide a good approximation for vessel diameters larger than about 100-200 μm if an appropriate non-Newtonian fluid model is used [56]. Nonetheless, continuum modelling of blood flow in vessels of diameters smaller than 100 μm is not adequate and requires explicit modelling of RBCs [16].

2.4.1 Time Characteristics

Appropriate numerical methods for a situation must be chosen after considering several relative time scales. The following time scales are expected to be important when modelling blood flow [15]:

1- The fluid time step, $\Delta t_f = \beta_1 L/U$, is used to update the fluid flow.

2- The particle time step, $\Delta t_p = \beta_2 d_p/U$, is used to identify particle collisions.

3- The sticking time step, $\Delta t_c = \beta_3 d_p(\rho_p^2/E_p^2 U)^{1/5}$, is used to compute adhesion forces.

In the above equations, L and U are respectively the macroscopic characteristic length and velocity scales of the fluid flow, ρ_p is the particle density and E_p is the Young's modulus of the particle. The variable d_p signifies the equivalent particle diameter; the diameter of a spherical particle having the same volume as the given particle. Constants β_1, β_2 and β_3 are all positive and smaller than unity. The values of these parameters for blood flow modelling are presented in the next paragraph.

The case of RBCs in arterial blood flow is considered as a representative example to illustrate sizes of the different time steps. The volume of an average RBC is 94 μm^3 [68], giving

an equivalent particle diameter of 5.64 μm. In a large artery, a fluid length scale of $0.2\,\mathrm{cm}$ (arterial diameter), fluid velocity scale of $20\,\mathrm{cm/s}$ (arterial mean velocity), and density ratio of plasma to cell of $\chi = \rho_f / \rho_p \cong 0.9$ are used and the dimensionless equivalent particle diameter is $\varepsilon = d_p / L = 2.82 \times 10^{-3}$. Setting $\beta_2 = \beta_3 = 10\beta_1$, the ratio of fluid time step to particle time step is $\Delta t_f / \Delta t_p = 35$. Assuming an elastic modulus for the RBC membrane of $E_p \cong 26\,\mathrm{kPa}$ [40], the ratio of particle time step to sticking time step is $\Delta t_p / \Delta t_c = 13$, resulting in 455 collision time steps for one fluid time step [10].

From these calculations one can conclude that RBC-flow time steps are ordered such that $\Delta t_f >> \Delta t_p >> \Delta t_c$. The fluid time step and particle time step are fractions of the fluid and particle time scales which are L/U and d_p/U respectively. The collision time step is a fraction of the time scale for the elastic response of a particle when it collides with another particle which is $d_p(\rho_p^2 / E_p^2 U)^{1/5}$ [92].

In the next section, a review of several numerical methods that can be applied to a RBC flow is given. These methods have different time scales which results in diverse accuracy and computational costs.

2.4.2 Classification of Numerical Models

Classical numerical methods are limited in their applications to certain ranges of space and time scales. Atomistic methods, such as the molecular dynamics (MD) and the Monte Carlo (MC) techniques, provide a detailed description on the level of a single atom; however such simulated systems are restricted to very small sizes and times, on the order of nanometers and nanoseconds, due to the demanding computational expense. Mesoscopic approaches include dissipative particle dynamics (DPD) [93, 94], the lattice Boltzmann method (LBM) [95], Brownian dynamics (BD) [96, 97], and smoothed particle hydrodynamics (SPH) [98, 99]. These methods can provide a “coarse-grained" description of a simulated system with respect to an atomistic representation by retaining some molecular physics. They allow for a significantly expanded range of time scales in comparison with atomistic methods, but their upper limit in spatial and temporal scales remains dependent on the size of coarse-graining used. As

mentioned, larger space and time scales are accessible by continuum approaches such as the Navier-Stokes (NS) equations. These methods rely on the continuum assumption and are likely to fail when molecular details of a simulated system are of physical importance [16].

Hybrid multiscale algorithms attempt to merge several existing methods that cover different ranges of space and time scales. They may offer a potential solution for bridging between various scales. Several recently developed hybrid methods include MD-NS coupling [100-103], and MD-LBM [104, 105]. Such algorithms undergo constant developments and improvements; however, to date, they are substantially restricted in their applications. Thus, current hybrid algorithms are able to adequately simulate some Newtonian fluid flows, while efficient multiscale approaches for flows of complex biological fluids are yet to be developed [16].

Between the atomistic and continuum scales lies the mesoscopic intermediate range, which exhibits features of both the atomistic and continuum regimes. It covers a range where the continuum description is not yet appropriate, and a direct treatment of the atomistic representation is not feasible due to a system size. Figure 2.11 shows a schematic plot of length and time scales corresponding to different regimes. The overlaps between the rectangles indicate that there are no definite borders between the neighbouring descriptions. However, gaps between some of the regimes are apparent; for example between the atomistic and the continuum [16].

RBC flow in microcirculation, where aggregation and disaggregation of RBCs complicate the flow, can be categorized in the mesoscale region. Thus, using hybrid methods, DPD-LBM can be considered for modelling blood flow. As shown in Figure 2.11 these models have time scales of 10^{-10} to 10^{-5} s for length scales of 10^{-3} to 10^{-7} m which entail huge computational costs for modelling a simple flow in microcirculation.

2.4.3 Mesoscale Time Dependent Models for Blood Flow

As discussed in the previous chapter, Bureau *et al.* [38] experimentally showed that blood has a time dependent response in Couette flow. This time dependency comes from the changes in microstructures of rouleaux. Hence, models that aim for accurate treatment of this kind of response should consider the microstructure of rouleaux. Fenech *et al.* [47] used the concept of the DPD model and showed that their model is able to predict this phenomena. Figure 2.12

shows a simulation of Fenech *et al.* that uses spherical particles as RBC and solved the equation of motion to find RBC position and velocity. Their model has shown to be in good agreement with prediction obtained with Owens' model (Figure 2.13).

Owens [11] used a very different and unique approach to this problem. He used a general form of the population-balance equation (the Smoluchowski equation [106]) to find an estimate for average aggregation size as a function of shear rates. He used this average size in deriving an equation for the apparent viscosity. His model is not computationally expensive, since it ignores the actual microscopic aggregation physics. Results obtained with his model are in good agreement with Bureau *et al.*'s results.

Owens' model uses the population-balance equation indirectly and considers this equation as a supplementary equation to his viscosity equation. On the other hand, Fenech *et al.* used a DPD model and reproduced the time dependent size of aggregation but without modelling the influence of the aggregate on the flow (*i.e.* using a predefined fixed velocity field). In this work the direct use of population-balance to find rouleaux size is proposed. This equation is fully coupled with the Navier-Stokes equation to find the effects of rouleaux size on the plasma flow. Using this method allows the particles' effect on the local viscosity to be estimated without directly simulating individual RBCs.

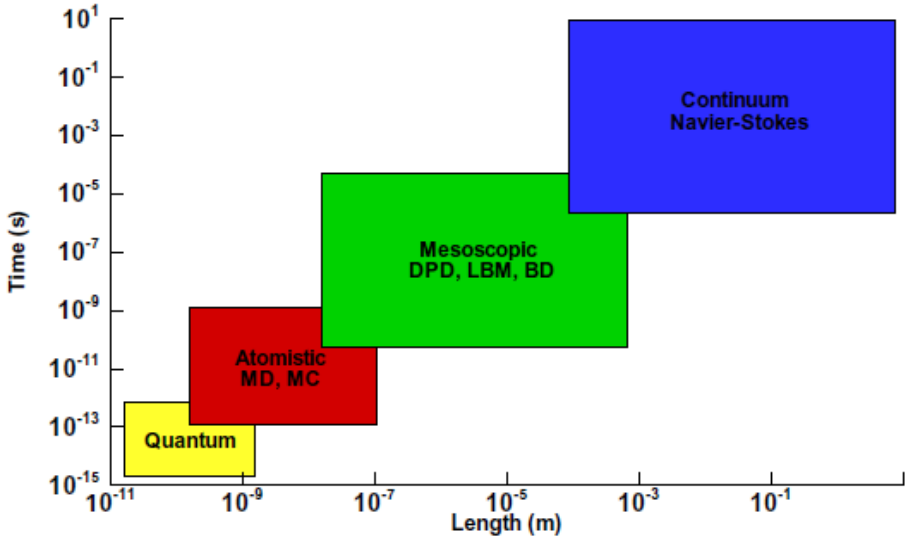

Figure 2.11: A schematic plot of various spatiotemporal scales covered by different descriptions (quantum, microscopic, mesoscopic, and continuum) with several examples of typical methods used [16].

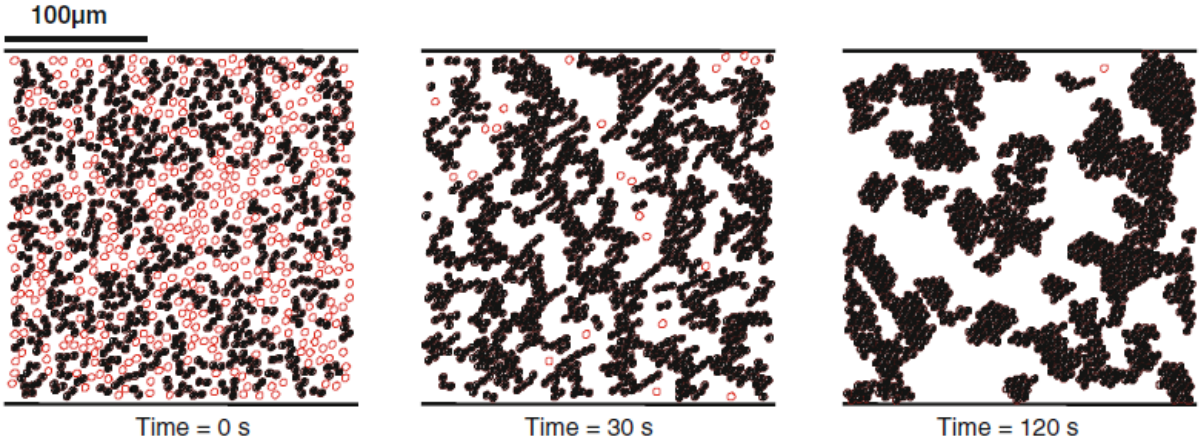

Figure 2.12: RBC aggregation kinetics as a function of time for shear rate of 0.1 s^{-1} for three different times. Empty and filled circles represent non-aggregated and aggregated cells, respectively. Reproduced from [47].

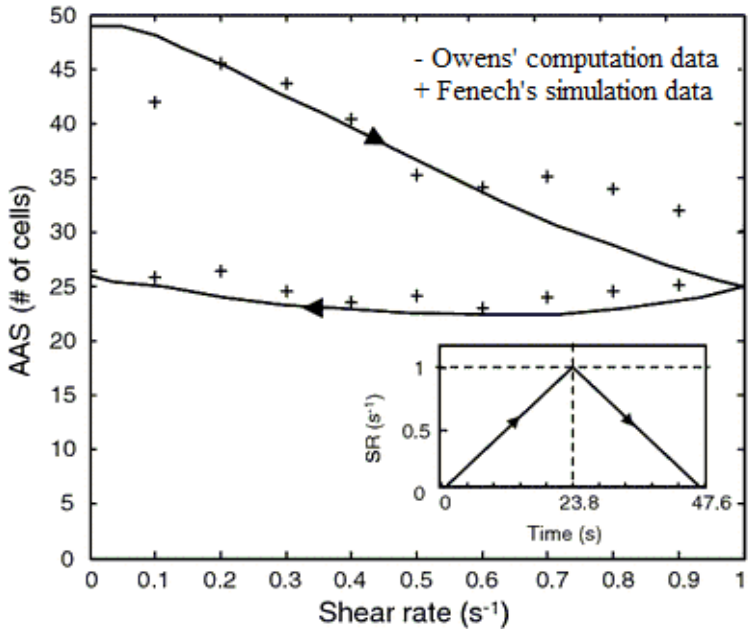

Figure 2.13: Hysteresis effect when a reversible increment of shear rate is applied on aggregated RBCs. The shear rate increases linearly to a maximum of 1 s^{-1} at t=23.8 s before returning linearly to zero at t=47.6 s. Reproduced from [47] .

2.5 Summary

In this chapter characteristics of blood are discussed. Phenomena like the cell-free layer, non-Newtonian viscosity and aggregation in blood flow are introduced. Previous works on blood, both numerical and experimental, are also discussed. Experimental works are also presented which include image processing in microfluidic devices and determination of aggregates sizes. In the next chapter, an introduction to the population-balance method is given. All the equations needed to build the current numerical model are also covered in Chapter 3.

Chapter 3

Background theory

3.1 Introduction to the Population-Balance Method

In this work, the population-balance method is proposed as an appropriate model to numerically investigate the formation and breakage of rouleaux in background plasma flow. In this method, individual particles are not treated directly. Rather statistics describing particle evolution at the continuum level are used. The effect of coalescence and break-up are also treated probabilistically. For example, Ramkrishna [107] studied cell population with single cells as the elementary particle, and the cluster of cells (tumors) as larger particles. In the same way, in this research, the presented computational model regards a single RBC as an elementary particle and aggregates (or rouleaux) as particles that are able to collide with and adhere to each other under the action of the fluid.

Instead of following individual particles, as it is done in particle tracking, a continuum approach based on particle statistics is used in population-balance modelling [108]. Aggregation and disaggregation are also treated probabilistically, with rates that are either measured experimentally, derived theoretically, or (as in this work) a combination of both. This method is used in many mesoscopic problems in which sets of particles can aggregate or break up. The concept of the population-balance equation is now being used in essentially every particle-fluid system. Examples listed in Table 3-1 demonstrate the wide-spread applications of the PBM.

Table 3-1: Simulations conducted using PBM

Yuu and Oda 1983 [109]	Aerosols
Kinneberg and Herbst 1984 [110]	Comminution
Hounslow 1990 [111]	Crystallization
Congalides and Georgakis 1981 [112]	Fluidised beds
Luo and Svendsen 1996 [113]	Bubble distribution in liquid
Chatzi and Kiaparissides 1992 [114]	Droplet distribution in liquid
Garg and Pratt 1984 [115]	Extraction
Ramkirishna 1979 [107]	Cell Population
Du and Wilson 1995 [116]	Rain formation

3.2 The Population-Balance Equation

In general, the population-balance equation (PBE) is a balance equation of the number density of one or multiple particle properties. In this research application, the particle property would be the diameter of particles (d_p). The PBE in its most general form is given by Ramkrishna [117] as

$$\frac{\partial n\left(d_p, x, t\right)}{\partial t} + \nabla_d \frac{d(d_p)}{dt} n(d_p, x, t) + \nabla_x \cdot u_p n(d_p, x, t) = B(d_p, x, Y, t) - D(d_p, x, Y, t). \tag{3-1}$$

In this equation $n(d_p, x, t)$ is the number density of particles with diameter of d_p and it is a function of the particle's location, x, and time, t. The $d(d_p)/dt$ term is the growth rate of the particle diameter* and u_p is the particle velocity at x and t. On the right hand side of the equation, B stands for the birth and D for the death of particles with the diameter, d_p. The dependence on a general parameter, Y, is introduced to describe the influence of the birth and death rates of particles by the continuous phase. For example, in the case of RBCs, Y could be the plasma shear rate, $\dot{\gamma}$, because it has a direct effect on disaggregation of rouleaux. The last two terms can be decomposed as

$$B - D = \left[B_B - D_B + B_A - D_A \right], \tag{3-2}$$

where term B_B indicates the birth of particles due to breakage (disaggregation) of larger particles, D_B indicates the death of particles caused by breakage, B_A indicates the birth of particles due to smaller particle aggregation and D_A indicates particle death as it aggregates with another particle. Both birth and death of particles happen each time either aggregation or disaggregation happen. In Equation (3-1), $B - D$ can be seen as a source term which is affected by the break up or aggregation of RBC's cluster in different size classes.

---

* For example, the growth of a bubble moving to a lower pressure environment.

The second term of Equation (3-1) usually is ignored for blood flow prediction, due to small or negligible change in the volume of particles. Similarly, the density of RBC aggregates does not change and therefore the growth rate of the particles is equal to zero in the present application.

Mathematically speaking, Equation (3-1) has time, space and size as independent variables. Hence, size, d_p, gives an additional dimension to the population-balance equation. Directly discretizing the population-balance equation in the size dimension results in

$$\frac{\partial n_\kappa}{\partial t} + \nabla u_\kappa n_\kappa = B_{B\kappa} - D_{B\kappa} + B_{A\kappa} - D_{A\kappa} \qquad for \quad \kappa = 1,...,N\,. \tag{3-3}$$

This approach is called the method of classes. In it, particles are classified according to their volume or equivalent diameter. Each class, κ, consists of particles with volume of v_κ with diameter of d_κ. In this equation, n_κ is the number density of particles of size "κ" and u_κ is the average velocity of all particles in size "κ" in the control volume.

Equation (3-3) can be interpreted as a balance law with four source terms $B_{B\kappa}$, $D_{B\kappa}$, $B_{A\kappa}$ and $D_{A\kappa}$, each with units of particles.m^{-3}s^{-1}. Figure 3.1 shows a control-volume representation for this equation. As seen, particles cross the control-volume boundary with a velocity of u_κ and their number density can either decrease (death) or increase (birth) inside the volume, depending on aggregation or disaggregation of particles.

Equation (3-3) can be rewritten using density of particles, ρ_κ, instead of number density of particles, n_κ, in a two-dimensional domain as,

$$\frac{\partial \rho_\kappa}{\partial t} + \frac{\partial \rho_\kappa u_{x\kappa}}{\partial x} + \frac{\partial \rho_\kappa u_{y\kappa}}{\partial y} = B_{B\kappa} - D_{B\kappa} + B_{A\kappa} - D_{A\kappa}\,, \tag{3-4}$$

where density of particles in each class is number density of that class multiplied by particle mass. In this equation the units for the four source terms become $\mathrm{Kg\,m^{-3}s^{-1}}$.

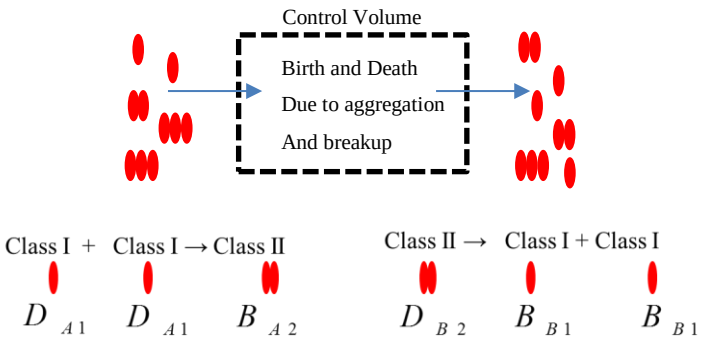

Figure 3.1: Schematic control-volume for the population-balance equation.

3.3 The Population-Balance Model for the Kinetics of RBC Aggregation

Before explaining how aggregation and disaggregation can be found, a historical review on the use of population-balance modelling on RBC aggregation should be given. In 1917, Smoluchowski introduced a theory that is based on the assumption that each particle is surrounded by a "sphere influence" [106]. Initially, the suspension consists only of single spherical particles, which undergo Brownian motion until they collide. Adhesion between particles requires their penetration into each other's sphere, and, once this is achieved, those collisions have equal probability of a successful interaction (sticking of particles). If a doublet is formed, the resulting particle undergoes Brownian movement with a reduced velocity until it enters the sphere of influence of another single or multiple particles. As aggregation proceeds, the average diffusion constant of the aggregate population decreases. It is noteworthy that this model is only applicable to space-homogeneous cases.

The model of Smoluchowski for colliding particles was applied by Ponder (1924) to the kinetics of RBC aggregation in stasis [118]. In developing the formula for rouleaux motion in *vitro*, Ponder limited his model to the treatment of average aggregate size (AAS), took into consideration that RBCs are too large for Brownian motion, and made the following assumptions:

1- The distribution of collision velocities is the same for single RBCs and rouleaux of all sizes.
2- The available contact area is the same in all three types of possible collisions: between single erythrocytes (e + e), between a single erythrocyte and a rouleau (e + r), and between two rouleaux (r + r).
3- Every collision achieving the required contact area results in cohesion.
4- Rouleaux, once formed, do not break up.

With these assumptions, Ponder proposed an equation for rouleaux formation (from singly dispersed RBCs) as a function of time and hematocrit [118] as

$$\mathrm{AAS} = 1 + 0.5 K\ t\ H_t. \tag{3-5}$$

here, AAS is the average aggregate size (average number of cells per aggregate), K is a constant, t is time, and hematocrit (H_t) is the total number of RBCs (both singly dispersed and in rouleaux) per unit suspension volume. Obviously, in the initial condition, when all RBCs are singly dispersed, $\mathrm{AAS} = 1$.

Similarly, Chen and Huang (1995) [88] and Owens (2006) [11] applied the population-balance model in Couette flow without the flux term of Equation (3-3). Owens [11] simplified the population-balance equation using total number of RBCs per unit volume, n_0 (number density of all RBCs), and total number of particles (RBCs and rouleaux). He derived a balance equation for average aggregate size as

$$\frac{d(\mathrm{AAS})}{dt} = \frac{1}{2}\Omega_A n_0 - \frac{1}{2}\Omega_B \mathrm{AAS}^2 + \frac{1}{2}\Omega_B \mathrm{AAS}. \tag{3-6}$$

Here, the first term can be neglected if a steady-state condition is assumed. In this situation, the disaggregation rate can be found as a function of aggregation rate, average aggregate size and total number of RBCs per unit volume. Owens [11] used this equation to develop an expression for the viscosity of blood that is dependent on the AAS. It is important to notice that the average aggregate size, itself, is a function of shear stress in Couette flow.

By using Equation (3-6) in steady-state conditions, a correlations for aggregation and disaggregation rates can be developed. These rates can be referred to as macroscopic aggregation and disaggregation rates, as they are developed using average aggregate size. This procedure is discussed further in Chapter 6. In the next section, Equation (3-3) is discussed further and microscopic aggregation and disaggregation rates are introduced.

3.4 Particle Transfer between Classes of Particles

The following equations are used to describe particles transfer between classes in [117], where each size has twice the volume of the size before it $v_{\kappa+1} = 2v_{\kappa}$:

$$B_{B\kappa} = \sum_{\lambda=\kappa+1,\lambda\neq N}^{N} \Omega_{B\kappa,\lambda} + \sum_{\lambda=1,\kappa\neq N}^{\kappa} b_{i+1,k}\,\Omega_{B\kappa+1,\lambda} + \sum_{\lambda=\kappa}^{N}\left(1-b_{\kappa,\lambda}\right)\Omega_{B\kappa,\lambda} \quad \text{for } \kappa = 1,...,N, \tag{3-7}$$

in which $b_{\kappa,\lambda} = 2^{1+\lambda-\kappa}$ for $\lambda > \kappa$, and

$$D_{B\kappa} = \sum_{\lambda=1}^{\kappa-1}\Omega_{B\kappa,\lambda} \quad \text{for } \kappa = 2,...,N, \tag{3-8}$$

$$B_{A\kappa} = \sum_{\lambda=1,\lambda\neq N}^{\kappa-1} c_{\kappa,\lambda}\Omega_{A\kappa,\lambda} + \sum_{\lambda=1}^{\kappa-1}(1-c_{\kappa-1,\lambda})\Omega_{A\kappa-1,\lambda} \quad \text{for } \kappa = 2,...,N, \tag{3-9}$$

in which $c_{\kappa,\lambda} = 1-2^{\lambda-\kappa}$ for $\kappa > \lambda$, and

$$D_{A\kappa} = \sum_{\lambda=1}^{N-1}\Omega_{A\kappa,\lambda} + \Omega_{A\kappa,\lambda}, \quad \text{for } \kappa = 1,...,N-1. \tag{3-10}$$

The term $\Omega_{B\kappa,\lambda}$ shows the breakage rate of particles in class κ to produce particles in class λ while $\Omega_{A\kappa,\lambda}$ gives the aggregation rate of particles due to collision and agglomeration of particles in class κ and λ. The first term on the right side of the Equation (3-7) indicates the birth rate of particles in class κ due to the breakage of larger particles in class λ ($\lambda > \kappa$). As a

result, this term should be calculated for $\lambda = \kappa + 1$ to $\lambda = N$, where N is the number of particles in rouleaux of the largest class. The next two terms arise due to the redistribution of particles. When a cluster in size class κ breaks, its volume is distributed into two daughter classes such that $v_\kappa = v_\eta + v_\lambda$. For example, consider a problem with size classes of 1, 2, 3, 4 with corresponding volumes 1, 2, 4, 8. A particle in size class 4 with volume of $v_\kappa = 8$ can break into $v_\eta = 7$ and $v_\lambda = 1$. The volume v_λ can be directly assigned to size class 1, but v_η must be redistributed to size classes 8 and 4 to conserve the volume. Here 14% of the volume of the particle is assigned to size class 4 and 86% to size class 8 to have the same volume. In general, v_η is redistributed among $v_{\kappa-1}$ and v_κ according to the volume balance constraint as $v_\eta = b_{\kappa,\lambda} v_{\kappa-1} + (1 - b_{\kappa,\lambda}) v_\kappa$ where, $b_{\kappa,\lambda} = 2^{1+\lambda-\kappa}$ for $\lambda < \kappa$.

Similarly, for the coalescence process, when a particle of volume v_κ coalesces with a smaller particle of volume, v_λ, they form a particle of volume v_η such that $v_\kappa < v_\eta < v_{\kappa+1}$. The volume v_η is redistributed between v_κ and $v_{\kappa+1}$ as $v_\eta = v_\kappa + v_\lambda = c_{\kappa,\lambda} v_\kappa + (1 - c_{\kappa,\lambda}) v_{\kappa+1}$. Here, $c_{\kappa,\lambda} = 1 - 2^{\lambda-\kappa}$ for $\kappa \geq \lambda$.

There are two important assumptions in this model. First, the smallest particle (single RBC $\kappa = 1$) cannot break into any smaller particle. Second, the largest particle ($\kappa = N$) cannot make any larger particle as it collides with other particles. For further information on how to arrange different sizes, readers can refer to [117, 108].

As an example of a system with only agglomeration, Equations (3-3) and (3-9) and (3-10) can be combined together for eight class of sizes, where the relation between classes is assumed to be $v_{\kappa+1} = 2v_\kappa$. These equations can be presented in a matrix form as

$$\begin{bmatrix} \partial n_1/\partial t \\ \partial n_2/\partial t \\ \partial n_3/\partial t \\ \partial n_4/\partial t \\ \partial n_5/\partial t \\ \partial n_6/\partial t \\ \partial n_7/\partial t \\ \partial n_8/\partial t \end{bmatrix} = -\begin{bmatrix} \Omega_{A11} & \Omega_{A12} & \Omega_{A13} & \Omega_{A14} & \Omega_{A15} & \Omega_{A16} & \Omega_{A17} & 0 \\ \frac{1}{2}\Omega_{A12} & \Omega_{A22} & \Omega_{A23} & \Omega_{A24} & \Omega_{A25} & \Omega_{A26} & \Omega_{A27} & 0 \\ \frac{1}{4}\Omega_{A13} & \frac{1}{2}\Omega_{A23} & \Omega_{A33} & \Omega_{A34} & \Omega_{A35} & \Omega_{A36} & \Omega_{A37} & 0 \\ \frac{1}{8}\Omega_{A14} & \frac{1}{4}\Omega_{A24} & \frac{1}{2}\Omega_{A34} & \Omega_{A44} & \Omega_{A45} & \Omega_{A46} & \Omega_{A47} & 0 \\ \frac{1}{16}\Omega_{A15} & \frac{1}{8}\Omega_{A25} & \frac{1}{4}\Omega_{A35} & \frac{1}{2}\Omega_{A45} & \Omega_{A55} & \Omega_{A56} & \Omega_{A57} & 0 \\ \frac{1}{32}\Omega_{A16} & \frac{1}{16}\Omega_{A26} & \frac{1}{8}\Omega_{A36} & \frac{1}{4}\Omega_{A46} & \frac{1}{2}\Omega_{A56} & \Omega_{A66} & \Omega_{A67} & 0 \\ \frac{1}{64}\Omega_{A17} & \frac{1}{32}\Omega_{A27} & \frac{1}{16}\Omega_{A37} & \frac{1}{8}\Omega_{A47} & \frac{1}{4}\Omega_{A57} & \frac{1}{2}\Omega_{A67} & \Omega_{A77} & 0 \\ 0 & 0 & 0 & 0 & 0 & 0 & 0 & 0 \end{bmatrix} \begin{bmatrix} 1 \\ 1 \\ 1 \\ 1 \\ 1 \\ 1 \\ 1 \\ 1 \end{bmatrix} + \frac{1}{2}\begin{bmatrix} 0 & 0 & 0 & 0 & 0 & 0 & 0 & 0 \\ \Omega_{A11} & 0 & 0 & 0 & 0 & 0 & 0 & 0 \\ \frac{1}{2}\Omega_{A12} & \Omega_{A22} & 0 & 0 & 0 & 0 & 0 & 0 \\ \frac{1}{4}\Omega_{A13} & \frac{1}{2}\Omega_{A23} & \Omega_{A33} & 0 & 0 & 0 & 0 & 0 \\ \frac{1}{8}\Omega_{A14} & \frac{1}{4}\Omega_{A24} & \frac{1}{2}\Omega_{A34} & \Omega_{A44} & 0 & 0 & 0 & 0 \\ \frac{1}{16}\Omega_{A15} & \frac{1}{8}\Omega_{A25} & \frac{1}{4}\Omega_{A35} & \frac{1}{2}\Omega_{A45} & \Omega_{A55} & 0 & 0 & 0 \\ \frac{1}{32}\Omega_{A16} & \frac{1}{16}\Omega_{A26} & \frac{1}{8}\Omega_{A36} & \frac{1}{4}\Omega_{A46} & \frac{1}{2}\Omega_{A56} & \Omega_{A66} & 0 & 0 \\ \frac{1}{64}\Omega_{A17} & \frac{1}{32}\Omega_{A27} & \frac{1}{16}\Omega_{A37} & \frac{1}{8}\Omega_{A47} & \frac{1}{4}\Omega_{A57} & \frac{1}{2}\Omega_{A67} & \Omega_{A77} & 0 \end{bmatrix} \begin{bmatrix} 1 \\ 1 \\ 1 \\ 1 \\ 1 \\ 1 \\ 1 \\ 1 \end{bmatrix}. \tag{3-11}$$

Here, the first matrix in the right hand side is death due to aggregation and the second matrix is birth due to aggregation. As can be seen in the death due to aggregation matrix, particles in class 8 cannot be destroyed due to aggregation as they are the biggest particle that can be formed. Similarly, in birth due to aggregation, there is no source term to introduce single particles. Only aggregation in smaller classes can introduce particles in higher classes.

In Equations (3-7) to (3-10), the microscopic aggregation and disaggregation are introduced. These two parameters need to be determined to reproduce experimental observation. Unfortunately, as discussed, the exact form of Ω_A and Ω_B function for RBCs is not known (either experimentally or theoretically). In the next section, the theory behind microscopic aggregation rate is discussed.

3.5 Aggregation Rate

The aggregation rate of particles of class κ and λ, $\Omega_A(\kappa,\lambda)$, is a function of two important parameters, the collision rate of particles in these classes, $\Gamma_{\kappa,\lambda}$, and sticking probability, $s_{\kappa,\lambda}$. It can be written as

$$\Omega_{A\kappa,\lambda} = \Gamma_{\kappa,\lambda}\, s_{\kappa,\lambda}. \tag{3-12}$$

In this equation, the collision rate is the rate that particles of class κ collide with particles of class λ and the sticking probability is the chance of successful collision that results in aggregation. A classical result of kinetic theory is that the collision rate between particles of class κ and λ is a function of mean particle relative speed between the two classes ($\bar{g}$), cross sectional area, $\sigma_{A\kappa\lambda}$, and number density of particles in each class n_κ and n_λ [119]. This relation is presented as

$$\Gamma_{\kappa,\lambda} = k_{\kappa\lambda}\sigma_{A\kappa\lambda} n_\kappa n_\lambda \bar{g}_{\kappa\lambda}. \tag{3-13}$$

A symmetric factor, $k_{\kappa\lambda}$, is introduced to prevent double counting, which corrects the double counting collisions between particles of the same class. For identical particles (also called like particles), $k_{\kappa\lambda} = \frac{1}{2}$, while for different particles (unlike particles), $k_{\kappa\lambda} = 1$. As is shown in Figure 3.2, the particles outside the cross sectional area $\sigma_{A\kappa\lambda}$ would not be able to collide. From this figure it can be concluded that

$$\sigma_{A\kappa\lambda} = \pi\,(r_\kappa + r_\lambda)^2. \tag{3-14}$$

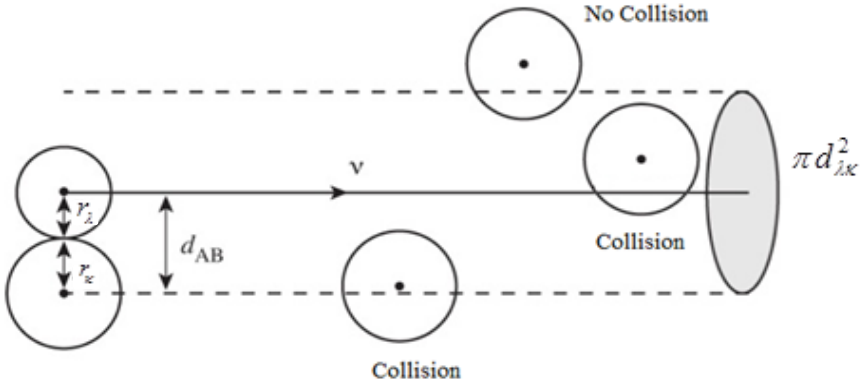

Figure 3.2: Illustration of the necessary area for a successful collision.

The mean particles relative speed, $\overline{g}$, between class κ and λ can be found to be

$$\overline{g_{\kappa\lambda}} = \frac{\sum_{\kappa=1}^{Np_\kappa}\sum_{\lambda=1}^{Np_\lambda}\sqrt{(v_{\kappa x}-v_{\lambda x})^2+(v_{\kappa y}-v_{\lambda y})^2+(v_{\kappa z}-v_{\lambda z})^2}}{(Np_\kappa-1)\,Np_\lambda}, \tag{3-15}$$

where, in this equation, Np_κ denotes the total number of particles in class κ.

The sticking probability, $s_{\kappa,\lambda}$, or sticking efficiency of two particles is a complicated function of their shape, surface condition, electrical potential energy and many other factors. For example, particles colliding with high kinetic energy might simply lead to a bounce. On the other hand, if a particle does not have enough kinetic energy, it would not be able to overcome the electrical potential between the particles. The sticking probability is considered as an unknown in this research and is found experimentally.

Looking back to Equation (3-11), for eight classes of particles there is 28 aggregation rates as unknowns. As discussed in this section, these unknowns themselves are functions of collision rates and sticking probabilities. In Chapter 6, these unknowns are found empirically from experimental data.

3.6 Disaggregation Rate

There are three predominant possible breakage mechanisms for a drop or a bubble in a flow [120]. These are turbulent breakage, viscous shear breakage and breakage due to acceleration of the flow. It is important to note that aggregation phenomena in blood can only be seen in microcirculation where the Reynolds number is smaller than one, therefore turbulent breakage is not relevant to this study. The acceleration of RBCs is expected to be low in these flows and are therefore considered not high enough to cause particle breakage in particles.

The disaggregation rate for particles of class κ that split into particles of class λ can be defined as

$$\Omega_{B\kappa,\lambda} = \omega_{\kappa,\lambda}\, n_{\kappa}, \tag{3-16}$$

where $\omega_{\kappa,\lambda}$ is the breakage frequency of particles in class κ that break into a daughter class of λ. The units for this parameter are s^{-1}.

The breakage distribution function should also be defined. This function describes the allocation of daughter particles when a particle in size κ breaks (term *b* in Equations (3-7) and (3-8)). The breakage of particles is a transient process and it cannot be observed directly in either of steady-state Couette or channel flow, as aggregation and disaggregation in these flows have reached to an equilibrium. These experiments are steady-state and particles have reached an equilibrium in them. Similarly, in the sedimentation test, very low shear exists in the domain and consequently, disaggregation cannot be observed. Therefore, no direct observation is done in this research to find the breakage of particles. To develop the model and to follow Equations (3-7) and (3-8), an assumption is made in this research. It is assumed that in case of breakage in a particle, daughter particles each have half of the volume from the original particle. This assumption, combined with the assumption for the relation between classes ($v_{\kappa+1} = 2v_{\kappa}$), simplifies mentioned equations greatly and it can be written as

$$B_{B\kappa} = \Omega_{B\kappa+1,\kappa} \qquad \text{for } \kappa = 1 \text{ to } N-1,$$
$$B_{D\kappa} = \frac{1}{2}\Omega_{B\kappa,\kappa-1} \qquad \text{for } \kappa = 2 \text{ to } N. \tag{3-17}$$

Similar to the Equation (3-11), for eight classes of particles, this equation will result in 7 unknowns. These unknowns are the breakage frequencies defined in the Equation (3-16), which are each a function of shear rate. The disaggregation rate is commonly considered as a power-law function of the shear rate and the aggregate size [121, 122]. This same relationship is found in the experimental results of Mehri *et al.* [13] for RBC breakage in shear flow. This subject will be discussed further in the experimental results section.

3.7 The Navier-Stokes Equations and the Population-Balance Equation, Two-Way Coupling

As the RBCs play an important role in the characteristics of blood, it is important to have two-way coupling between RBCs and plasma in any accurate model. Two-way coupling means the momentum transfer between RBCs and background plasma is considered in the model. The simplified continuity and momentum equations for base fluid (plasma) in a 2D domain are presented as,

$$\frac{\partial(\rho_f \alpha_f)}{\partial t} + \frac{\partial(\rho_f \alpha_f u)}{\partial x} + \frac{\partial(\rho_f \alpha_f v)}{\partial y} = 0 \tag{3-18}$$

$$\frac{\partial(\rho_f \alpha_f u)}{\partial t} + u\frac{\partial(\rho_f \alpha_f u)}{\partial x} + v\frac{\partial(\rho_f \alpha_f u)}{\partial y} = -\frac{\partial p}{\partial x} + \left(\mu + \sum \mu_\kappa\right)\left(\frac{\partial^2 u}{\partial x^2} + \frac{\partial^2 u}{\partial y^2}\right) + F_{pl} \tag{3-19}$$

$$\frac{\partial(\rho_f \alpha_f v)}{\partial t} + u\frac{\partial(\rho_f \alpha_f v)}{\partial x} + v\frac{\partial(\rho_f \alpha_f v)}{\partial y} = -\frac{\partial p}{\partial y} + \left(\mu + \sum \mu_\kappa\right)\left(\frac{\partial^2 v}{\partial x^2} + \frac{\partial^2 v}{\partial y^2}\right) - \rho_f g_y + F_{pl} \tag{3-20}$$

.

In these equations, α_f is the volume fraction of liquid and ρ_f is the density of base fluid. The term μ_κ is the intrinsic viscosity. It represents the increase in observed viscosity caused by the presence of particles in class κ. Further details on this term are given in

Subsection 3.7.8. The term F_{pl} is a source term in these equations that comes from the reaction force from suspended particles. To find the momentum transfer between phases, all the forces on the RBCs should be calculated and the reaction of these forces should be applied to the base fluid. These forces are described in the next section. As the density of single RBC is very close to the density of plasma, the volume fraction of particles α_p and therefore volume fraction of fluid α_f can be found using

$$\alpha_p = \frac{\sum \rho_\kappa}{\rho_f} \text{ and } \alpha_f = 1 - \alpha_p . \tag{3-21}$$

3.7.1 Equations of Motion for Particles

The population-balance equation can be coupled to the momentum equation for each class of particles (single or rouleaux of RBCs) and the momentum conservation for particles in each class is modelled as

$$\frac{\partial \rho_\kappa u_{x\kappa}}{\partial t} + \frac{\partial \rho_\kappa u_{x\kappa}^2 + P}{\partial x} + \frac{\partial \rho_\kappa u_{y\kappa} u_{x\kappa}}{\partial y} = MB_{B\kappa} - MD_{B\kappa} + MB_{A\kappa} - MD_{A\kappa} + F_{lp} \tag{3-22}$$

$$\frac{\partial \rho_\kappa u_{y\kappa}}{\partial t} + \frac{\partial \rho_\kappa u_{x\kappa} u_{y\kappa}}{\partial x} + \frac{\partial \rho_\kappa u_{y\kappa}^2 + P}{\partial y} = MB_{B\kappa} - MD_{B\kappa} + MB_{A\kappa} - MD_{A\kappa} + F_{lp}, \tag{3-23}$$

where $MB_{B\kappa}$, $MD_{B\kappa}$, $MB_{A\kappa}$ and $MD_{A\kappa}$ are momentum transfer between classes due to birth and the death of particles because of aggregation and breakage. To calculate these terms, a similar method used to calculate the birth and the death of particles $B_{B\kappa}$, $D_{B\kappa}$, $B_{A\kappa}$ and $D_{A\kappa}$ is used (Equations (3-7) to (3-10)). For example, when particles in class κ aggregate with particles in class λ, the new particle should have the sum of momentum of both colliding particles.

An artificial pressure, P, is inserted in these equations to limit particle density to a maximum physical value. In the absence of the artificial pressure, Equations (3-22) and (3-23) can result in a non-realistic situation where the particles density can exceed the maximum packing fraction. This pressure is discussed later in the Section 3.7.7. F_{lp} is the source term for momentum transfer between base fluid flow and particles and can be written as

$$F_{lp} = F_{D\kappa} + F_{G\kappa} + F_{L\kappa} + F_{VM\kappa}. \tag{3-24}$$

The forces on particles include gravitational forces (weight and buoyancy), F_G; drag, F_D; added mass (or virtual mass), F_{VM}; and lift force, F_L. All of these forces are found using low-Reynolds-number approximations. The Reynolds number of a particle Re_p is calculated using

$$\mathrm{Re}_p = \frac{\rho_f \left| u_p - u_f \right| d_p}{\mu}. \tag{3-25}$$

Here, u_f is the base fluid velocity at the particle centroid, and μ is the base fluid dynamic viscosity. Solving the momentum equation for particles requires an estimate for each of these forces on particles. These forces are described in the following subsections.

3.7.2 Gravitational Forces

Weight and buoyancy forces can be described using

$$\vec{F}_G = \left(\rho_p - \rho_f\right)\vec{g}, \tag{3-26}$$

where ρ_p is the particle's density and g denotes gravity.

3.7.3 Drag Force

Unlike gravitational forces, other forces have a more complicated correlation due to the shape of RBCs. In this research, it is assumed that aggregated RBCs are either rigid ellipsoids or rigid spheres. For an isolated ellipsoidal particle in low-Reynolds-number flows, hydrodynamic drag is given by Gallily and Cohen [123] as

$$\vec{F}_D = \mu \hat{K} \cdot \left(\vec{u}_p - \vec{u}_f\right), \tag{3-27}$$

where $\hat{K}$ is the particle frame translation tensor, and u_f is the base fluid velocity at the particle centroid. The particle frame translation tensor for an ellipsoid is a diagonal matrix given by Happel and Brenner [124] as

$$\hat{K} = 16\pi abc\left(\frac{e_{\hat{x}} \otimes e_{\hat{x}}}{\chi_0 + a^2\alpha_0} + \frac{e_{\hat{y}} \otimes e_{\hat{y}}}{\chi_0 + b^2\beta_0} + \frac{e_{\hat{z}} \otimes e_{\hat{z}}}{\chi_0 + c^2\gamma_0}\right), \tag{3-28}$$

where a, b and c are the elliptical particle's semi axes, and $e_{\hat{x}}$, $e_{\hat{y}}$ and $e_{\hat{z}}$ are unit vectors in the particle coordinate system, and $\otimes$ denotes the tensor product. The coefficients $\alpha_0, \beta_0, \gamma_0$, and χ_0 are given by

$$\begin{aligned} \chi_0 &= abc\int_0^\infty \frac{du_p}{\Delta} & \alpha_0 &= abc\int_0^\infty \frac{du_p}{\left(a^2 + u_p\right)\Delta} \\ \beta_0 &= abc\int_0^\infty \frac{du_p}{\left(b^2 + u_p\right)\Delta} & \gamma_0 &= abc\int_0^\infty \frac{du_p}{\left(c^2 + u_p\right)\Delta} \end{aligned} \tag{3-29}$$

where

$$\Delta = \left[\left(a^2 + u_p\right)\left(b^2 + u_p\right)\left(c^2 + u_p\right)\right]^{1/2}. \tag{3-30}$$

A correction factor, f, proposed by Di Felice [125], that accounts for the effect of particle concentration, or crowding, near the particle of interest can also be included in expression (3-28) for drag force resulting in

$$\vec{F}_D = \mu\hat{K}\cdot\left(\vec{u}_p - \vec{u}_f\right) f \ . \tag{3-31}$$

The correction factor is given as

$$f = \left(1 - \sum n\left(\kappa, t\right)\right)^{-\bar{\beta}}, \tag{3-32}$$

where $n(\kappa, t)$ is the number density at the location of the particle in class κ at time t (found using the PBE equation), and $\bar{\beta}$ is a parameter that depends on the particle's Reynolds number given as

$$\bar{\beta} = 3.7 - 0.65\exp\left(-\frac{1}{2}\left[1.5 - \ln\left(\mathrm{Re}_p\right)\right]^2\right). \tag{3-33}$$

With the correction factor defined in Equation (3-33), the expression for the drag force reduces to the expression for drag force on an isolated particle, Equation (3-28), when the number density is zero. Also, $\hat{K}$ for a rigid sphere particles can be calculated when $a = b = c$ which results in $\hat{K} = 6\pi d$.

3.7.4 Lift and Magnus Force

The lift force, caused by the base fluid flow, acts normal to the direction of flow and is caused by the shear and the particle's rotation. For a particle with a rotation rate equal to that of the base fluid surrounding the particle, the lift force correlation is given by Saffman [126, 127] as,

$$\vec{F}_{L} = -2.18\chi \frac{\left(\vec{u}_p - \vec{u}_f\right) \times \vec{\omega}}{\mathrm{Re}_p^{0.5}} \left(\frac{2\left|\vec{u}_p - \vec{u}_f\right|}{\left|\vec{\omega}\right| d_p} \right)^{0.5}, \tag{3-34}$$

where ω is the base fluid vorticity and χ is the ratio of plasma density to RBC density. This density ratio χ is about 0.9 for blood [10].

3.7.5 Virtual Mass Force

A spherical particle accelerating in a stationary background fluid feels a resistance force in addition to the drag force that is proportional to its acceleration. The added mass or virtual mass is this additional force necessary as an accelerating or decelerating body must move a volume of surrounding fluid as it moves through it which is not considered in the drag force formulation [128]. The virtual mass force, F_{VM}, is related to the acceleration of the particle and the required change in kinetic energy of the fluid as the particle moves through it. It is given by,

$$\vec{F}_{VM} = -\bar{c}_M \chi \left(\frac{d\vec{u}_p}{dt} - \frac{d\vec{u}_f}{dt} \right), \tag{3-35}$$

where the added mass coefficient $\bar{c}_M$ is 0.5 for a spherical particle [10].

3.7.6 Other Forces

Other insignificant forces are Brownian and Basset forces. Because forces due to molecular effects, such as Brownian motion, are negligible for particles with diameters greater than 1 μm, cells in blood flow are not affected by these forces [10]. In addition, the diffusive effect of the "fading memory" or Basset force F_b is insignificant for particles the size of cells because $|F_b| / |F_D| \cong \mathrm{Re}_p^{0.5} << 1$.

3.7.7 Artificial Pressure

In Equations (3.21) and (3.22) an artificial pressure was introduced. This pressure should be defined such that, when the particle volume fraction gets near the maximum packing fraction, it activates and quickly increases in severely to prevent future compressions. The function should be continuous as its derivative has a direct effect on the hyperbolic wave nature of the particle-flow model. Red blood cells are very flexible and therefore they can efficiently pack together. A maximum packing fraction, $\alpha_{\max}$, of 90% is reported in the literature [129]. The following equation is suggested and tested (in Section 5.5) to produce a similar physical behaviour as blood.

$$P = \frac{\alpha}{\left(10^8(\alpha_{\max} - \alpha)\right)^9} \tag{3-37}$$

This equation is designed so that, when the volume fraction of particles approaches the maximum packing fraction, it results in a high pressure. The pressure resulting from this function when the volume fraction is not close to the maximum packing fraction is negligible. This function is further analyzed in the verification section (Section 5.5).

3.7.8 Intrinsic Viscosity

The last parameter that should be discussed in this section is the intrinsic viscosity (μ_κ). Figure 3.3 shows the effect of particles on the background fluid. As can be seen, the effects can be separated into to two. The first part is the Stokes drag which is applied as a force source term. The second effect is the part which contributes to the viscosity. Einstein [130], first discussed this effect of spherical particles on the background fluid. Later Jeffery [131] did the same

analysis for ellipsoidal particles. It is important to note that these theories are developed for low concentration of particles in the background fluid. Detailed derivation of the following equations can be found in [132].

The intrinsic viscosity for spherical particles can be written as

$$\mu_\kappa = \frac{5}{2}\mu\phi_\kappa n_\kappa, \text{ where } \quad \phi_\kappa = \frac{4}{3}\pi r_\kappa^3. \tag{3-38}$$

Similarly for ellipsoidal particles, it can be written as

$$\mu_\kappa = A\mu\phi_\kappa n_\kappa, \text{ where } \quad \phi_\kappa = \frac{4}{3}\pi a_\kappa b_\kappa^{\,2}. \tag{3-39}$$

In this equation a_κ and b_κ are the semi-axes of the ellipsoidal particles in each class and it is assumed that $c_\kappa = b_\kappa$. Correction factor A values are presented in Table 3-2.

Table 3-2: Correction factor for intrinsic viscosity of suspended ellipsoidal particles [132]

a/b	0.1	0.2	0.5	1.0	2	5	10
A	8.04	4.71	2.85	2.5	2.91	5.81	13.6

Detailed discussion on the calculation of the correction factor can be found in [131] and more detailed tables similar to Table 3-2 can be found in [133]. As it can be seen when $a/b = 1$, the correction factor corresponds to spherical particles. Further detail on red blood cell geometry in a flow is discussed later in the results section, where the particles' semi axes are found using image processing techniques.

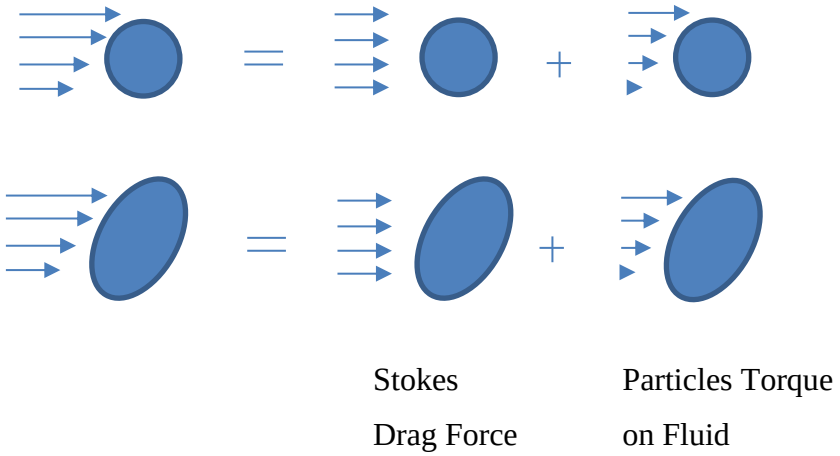

Figure 3.3: Effects of particles on the background fluid flow.

3.8 Summary

In this chapter the background theory needed to start modelling red blood cell flow in plasma using a population-balance method is given. First, the missing parameters needed to complete this model are discussed and after, the interaction between background fluid and red blood cells is introduced.

Important parameters in the population-balance model are the aggregation rate and the disaggregation rate which will be found through experiment. Further discussions on these parameters are provided in Chapter 4.

All the equations needed for a comprehensive model for blood flow are given in this chapter. In Chapter 5, the methods used to apply these equations and to couple them together are given. The computational method used to discretize these equations is also discussed in that chapter.

Chapter 4

Experimental Procedure

4.1 Introduction

As discussed in Chapters 1 and 2, the proposed numerical model is in need of experimental parameters for aggregation rate and disaggregation rate. Therefore, in this chapter, the experimental procedures used to find these expressions are explained. Three experiments are analyzed in this section: red blood cell sedimentation, Couette flow, and pressure-driven channel flow. The sedimentation test was conducted by the author and is explained in detail here in this chapter. The Couette flow and channel flow experiments were done by Mehri *et al.* [13] and Gliah *et al.* [134]; their results and images are used directly. All the experiments were done at room temperature.

The sedimentation test is designed to measure the aggregation rate. In this transient set-up, RBCs aggregate and form bigger particles. These particles move due to gravity and the interaction between particles increases due to these movements. As the background flow is nearly stationary, low shear rate is expected in the flow. It is assumed that the disaggregation rate is a function of shear rate and, therefore, it can be neglected in this test.

The Couette flow is steady-state and independent of time. In this test RBCs aggregation and disaggregation reach to a balance, where the particle size distribution does not change with time. The shear rate is a variable in this test and RBC particle size distribution depends on it. This test is used to find the disaggregation rate as a function of shear rate.

The pressure-driven channel flow is also a steady-state flow and the shear rate in this flow changes in the domain. These characteristics make this flow a good case to validate the model and to study cell-free layer formation.

In Section 4.2 an overview of the microchannel fabrication procedure is given. This method is used to build the case studies. In Section 4.3, an overview of blood sample preparation for the experiment is given. Section 4.4 is dedicated to experimental setup and the video microscopic system. Finally, in Section 4.5 an overview of the image processing technique is given.

4.2 Microchannel Fabrication

In order to perform any experimental tests, a proper channel should be designed and fabricated. Poly-di-methyl-siloxane (PDMS) is used for the fabrication of channels. PDMS is formed from a mixture of a silicon base elastomer and a curing agent at a ratio of 10:1. This gives an appropriate stiffness that is suitable for the application.

Channel molds can be prepared using different methods. The first method is to design a mask using "AutoCAD" software. Completed designs are sent to special commercial printers for accurate printing with a tolerance of $\pm 1\ \mu m$ (Figure 4.1(a)). Once the mask is printed, it can be used to create a mold. For this step, negative photoresist is spin coated on a silicon wafer and exposed to UV lights. A complete protocol for this procedure has been provided by Renaud *et al.* [135]. For simpler geometries, where tolerances are not important, it is also possible to use scotch tapes and glass slides to fabricate the mold [136, 137]. The channel mold is created by attaching tape to the glass slide, drawing the layout on it, and using a scalpel to cut the tape on the glass slide according to the layout. Next, the tape is removed from all regions of the glass slide except those in the layout of the microchannel to create the mold [137]. This method is only used for fabrication of the mold for the sedimentation test.

After preparation of the mold, PDMS is poured on the glass slide, then it is heated for 90 minutes at $80^{o}C$ to obtain a flexible but solid structure (Figure 4.1 (b)). This structure is cut to separate the single channels, as seen in Figure 4.1 (c). The channels are then punched at the channel inlets to insert 2.5 mm diameter connectors. Finally the punched channels are bonded to a microscope glass slide. The bonding process utilizes the oxygen plasma bonding method using the PE-50 series plasma system (Plasma Etch, USA). When the two surfaces to be bonded are exposed to the oxygen plasma, the surface layers with the lower molecular weight are removed while the uppermost atomic layer of the polymer is oxidized. The advantage of using this method is the non-reversible bonding created that comes with clean surfaces to avoid blockage of the channel. Though PDMS is naturally hydrophobic, this treatment gives a hydrophilic nature to the surface that lasts for at least 150 hours [12,72].

For the sedimentation study, a U shape channel with 100 µm height is used that is similar to the one used by Jayavanth *et al.* [138]. In this geometry, it is less likely to have air bubbles when filling the channel. The different lengths of this channel can be viewed in Figure 4.2 (a). Measurement of the height is done by cutting the channel and looking at it under the microscope, as shown in Figure 4.2 (b).

For the Couette flow configuration, experimental data and images acquired by Mehri *et al.* [1] are used. The microchannel configuration and the flow in the microchannel are shown in Figure 4.3 (a) and (b) respectively. In this set-up flow in upper layer has a higher flow rate which results in a quasi-Couette flow in the blood layer. As can be seen, this set-up is not a perfect Couette flow, but velocity profile measured by Mehri [13] show that the flow in the blood layer has similar characteristics to Couette flow. For simplicity, throughout this research, this set-up is called the Couette flow set-up.

Finally, for channel flow, the acquired images for a rectangular cross-section microchannel with height of 100 µm are used. This experiment was conducted by Gliah *et al.* [134]. This flow is used to validate the final numerical model. A sample image from these experiments is reproduced in Figure 4.4.

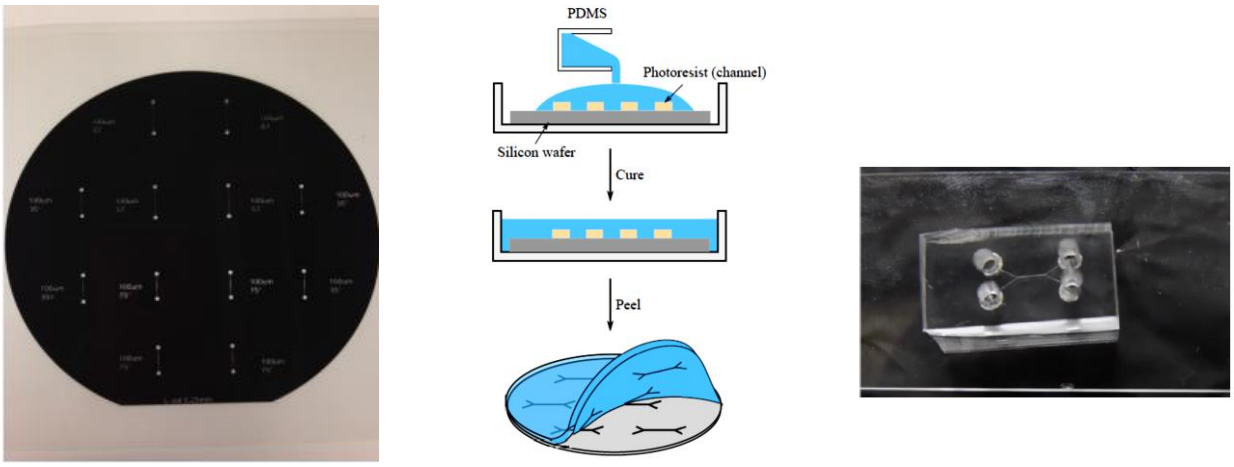

a) Mask fabrication b) Wafer fabrication c) Cut PDMS

Figure 4.1: Fabrication process of the microchannel using the photolithography method [139]

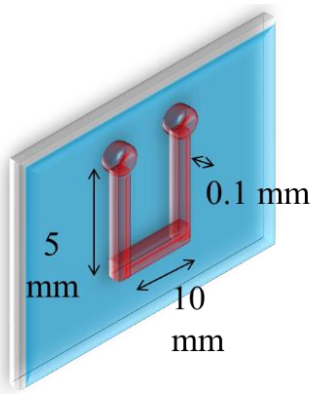

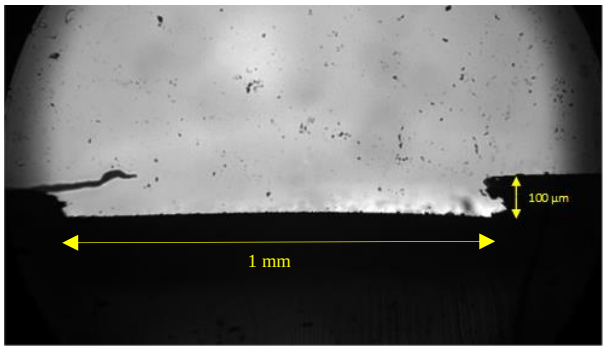

a) The U shaped set-up

b) Cross-section of the channel

Figure 4.2: Sedimentation test set-up and optical measurement of cross-sectional depth

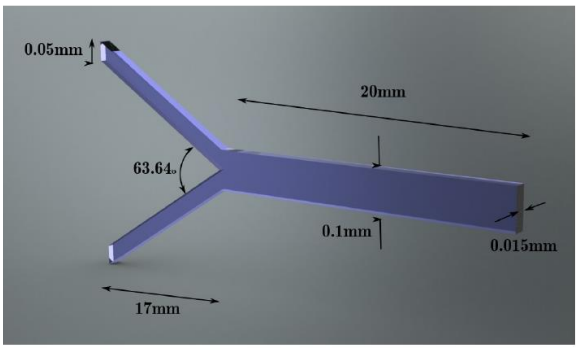

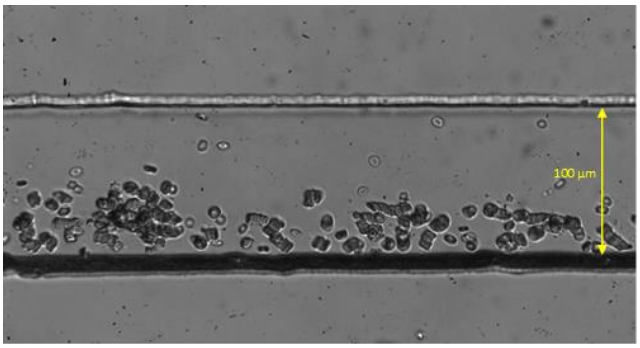

a) Schematic of the Couette flow set-up

b) Example image from of the Couette flow set-up

Figure 4.3: Schematic of the geometry and example image from Couette flow experiments of Mehri et al. [1].

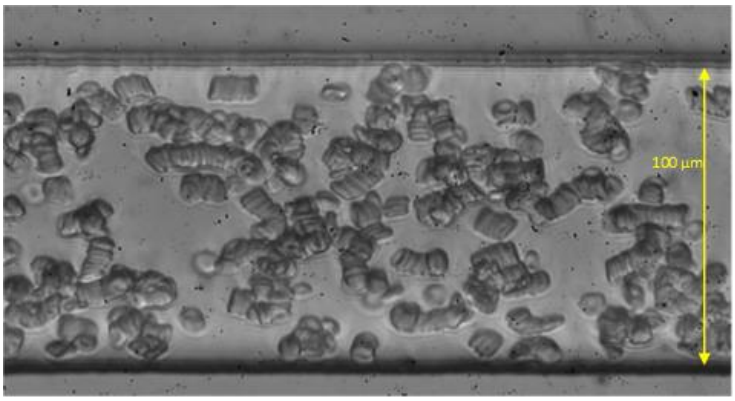

Figure 4.4: Example image from channel-flow experiment conducted by Gliah et al. [134].

4.3 Blood Sample Preparation

Healthy human blood (or porcine blood for proof of concept) is used to evaluate the effect of RBCs aggregation on the bulk properties of the blood. The blood is collected into a tube coated with EDTA. Before starting the test, volunteer whole blood goes through an aggregation test using RheoScan AnD300 aggregometer which uses the light transmission method to find the aggregation index (Rheomeditech, Inc., South Korea). Later, these measurements are compared for different samples to have a better understanding of aggregation rate. Samples are then centrifuged three times for ten minutes at 3000 RPM. After the first round of centrifugation all the plasma is removed from the sample. White blood cells and platelets are removed after each centrifugation, leaving only the RBCs at the end. Instead of plasma, phosphate buffered saline (PBS) is added to the RBCs and the combination is gently mixed before the next centrifugation. After the third round, RBCs are suspended in their own native plasma at desired hematocrits of 5% and 10%. As there is human error when preparing the intended hematocrit, these hematocrits are measured again using micro centrifuge before starting each test.

4.4 Experiment Setup

The experiment setup shown in Figure 4.5 was used for the sedimentation experiments. It consists of a high-speed camera (acA1300, Graftek Imaging, Inc., Austin, TX, USA) controlled using LabVIEW software (National Instruments, USA), an inverted custom microscope with a 10X lens magnification and a white light source. Images are recorded at the rate of one frame per second. The frame capture is controlled via a program developed in LabVIEW, where parameters such as the exposure time of the camera, the frame rate and the field of view can be varied to obtain the highest image quality for each case for proper post processing. These parameters are adjusted before each experiment to try to obtain the highest image quality possible. A sample from the recorded images for hematocrit of 5% is shown in Figure 4.6.

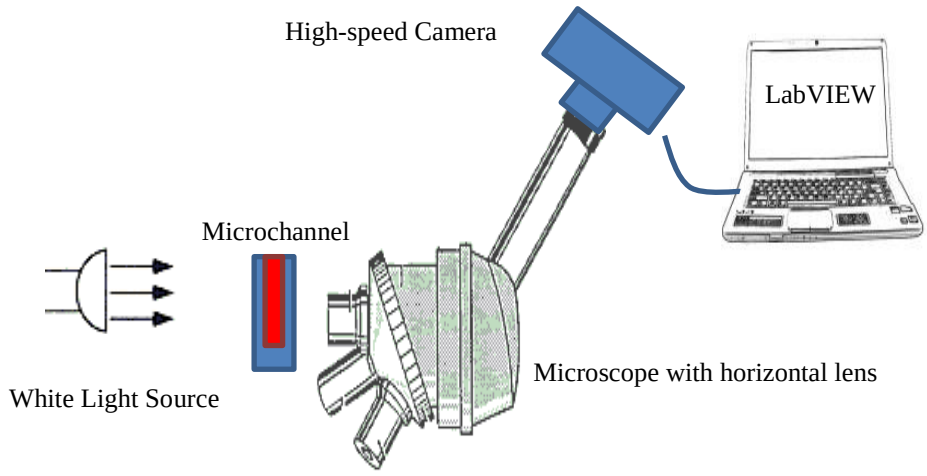

Figure 4.5: Costume video-microscopic system used in the sedimentation experiment.

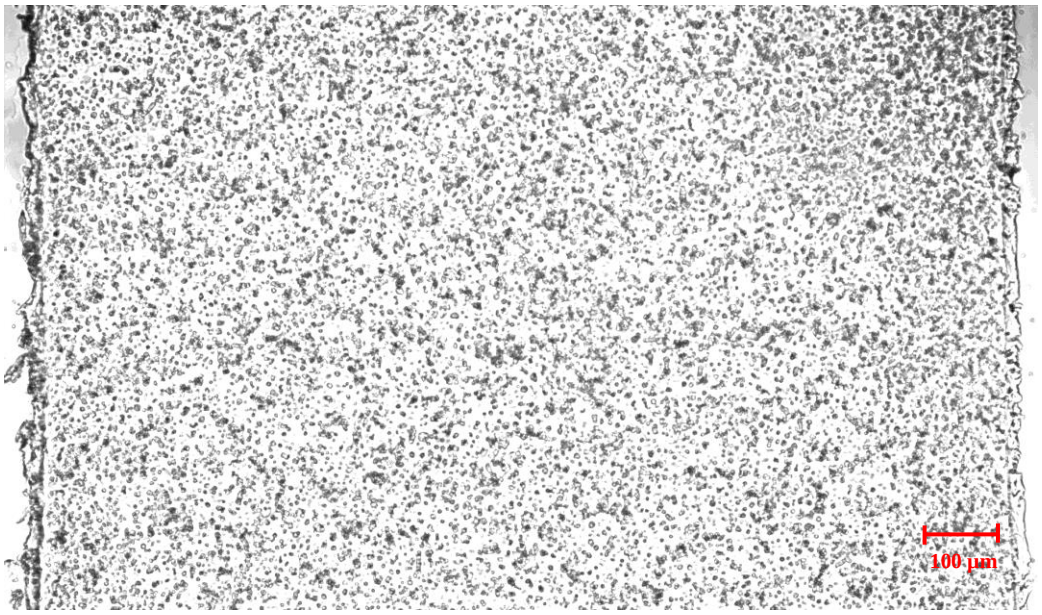

Figure 4.6: Sample image from sedimentation experiments.

Similarly, Figure 4.7 shows the experimental set-up used by Mehri *et al.* [140] for the situation of Couette flow. The experimental setup comprises a µPIV device (LaVisions MITAS) in order to visualize the flow and estimate the velocity field. This µPIV set up is composed of a CCD image intense camera (LaVision gmbh, Germany) with a resolution of 1376x1040 pixels and a very low read out noise, a NewWave Solo-II Nd:YAG laser (New Wave Research, USA) emitting a wavelength of λ = 532 nm and a MITAS inverted microscope (LaVision gmbh,

Germany) with a 20x lens magnification. The fluids, contained in two 50 µl glass syringes (Hamilton, USA), are pushed into a PDMS microchannel at different flow rates using two pumps (Nexus3000, Chemyx Inc., USA and picoplus, Harvard Apparatus, USA). The velocity field of plasma is obtained by velocity measurement of florescent micro particles suspended in liquid. Finally, the motion of RBC in the microchannel is visualized using a high-speed camera controlled using LabVIEW software coupled with the LaVision device [140]. The shear rates in this experiment range from 3.66 to 41.00 s^{-1}.

A similar set-up and experiment is also used by Gliah [134] for channel flow. The only difference is that they used one syringe, as their microchannel had one entrance. Three flow rates of 8, 12 and 16 µl/hr are used which results in apparent shear rates of 28, 56 and 84 s^{-1}.

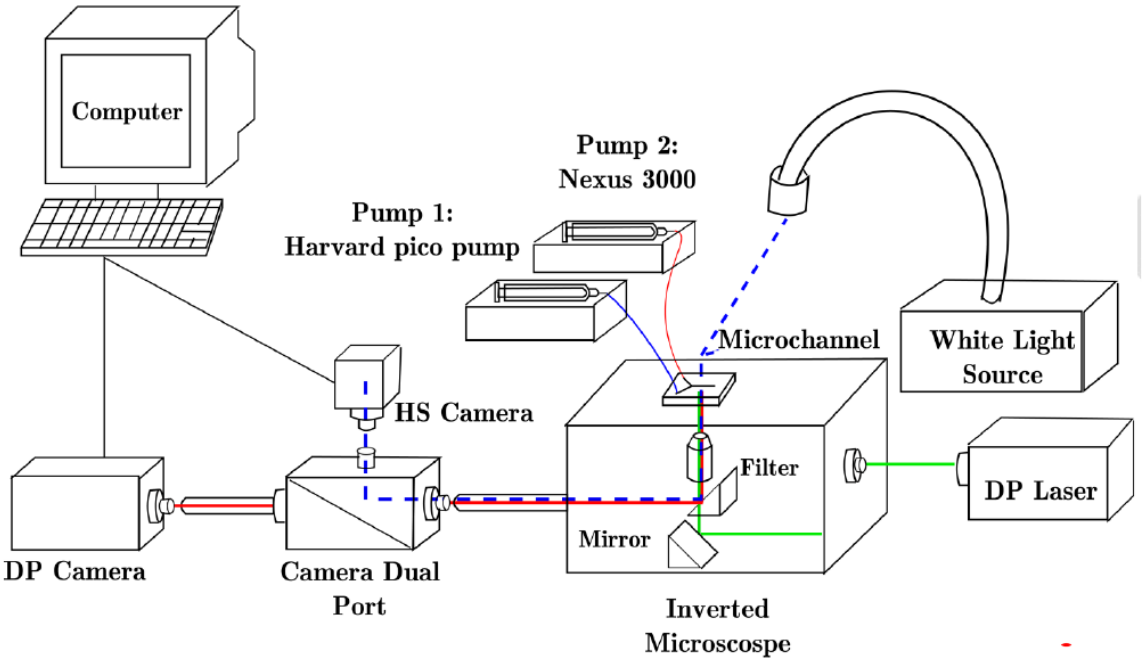

Figure 4.7: Video microscopic system used for the Couette flow experiment by Mehri et al. [140]

4.5 Image Processing

The image-processing technique that is used to detect aggregation size and find particle velocity distribution is described in this section. Both Matlab and ImageJ softwares was used for image processing purposes. For repeatability and faster analysis a user friendly Matlab GUI and batch processing code for ImageJ was developed. The Matlab GUI is discussed in the next section. The ImageJ software does similar processing and is just used to verify the results in Matlab. ImageJ processing is discussed in Section 4.5.4.

4.5.1 Matlab

A Matlab code with a graphical user interface (GUI) was developed for the detection of rouleaux size and velocity. The interface is shown in Figure 4.8. Though developed for RBC rouleaux measurement, this code is flexible enough to be used in a wide range of particle-tracking applications. To make sure that users are not confined to use a specific lens magnification, all the results are reported using pixels as the unit of distance.

After a picture is opened in the GUI, the user can choose different image enhancing methods and filters. These methods includes: 1- Removing the background, 2- Increasing the contrast, 3- Contrast-limited adaptive histogram equalizer, 4- FFT band pass filtering, 5- Averaging filter, 6- 2D median filter. The GUI also has an additional option for filters that are not available in the interface and the user can easily extend the software through the addition of other filters. Details about these filters can be found in the Matlab user guide and the effects of each filter are shown in Figure 4.9. Next, the user can improve the detection by choosing one or more binary operators. These operators include: 1- Complement, 2- Dilate, 3- Erode, 4- Remove Edges 5- Fill holes, 6- Removing small objects, 7- Watershed. Similarly there is a space in the code to add more operators by other users. The effects of each binary operator are shown in Figure 4.10.

Choosing an appropriate threshold to change the filtered image to a binary image is an important step in the image processing. By removing the background in different processes, one can often find a threshold value that is effective for a wide range of tests with different level of light in the background.

Given a set of images, it is up to the user to experiment and find the optimal filters and settings to accurately detect particles. For example, in Figure 4.11 the same image is subjected to the following filters: 1- Remove background, 2- Increase contrast and 3- 2D median filtering. Similarly the following binary operators are also applied: 1- Dilate, 2- Remove edges, 3- Fill holes and 4- Remove smaller objects. The result is that individual particles are effectively isolated from the background.

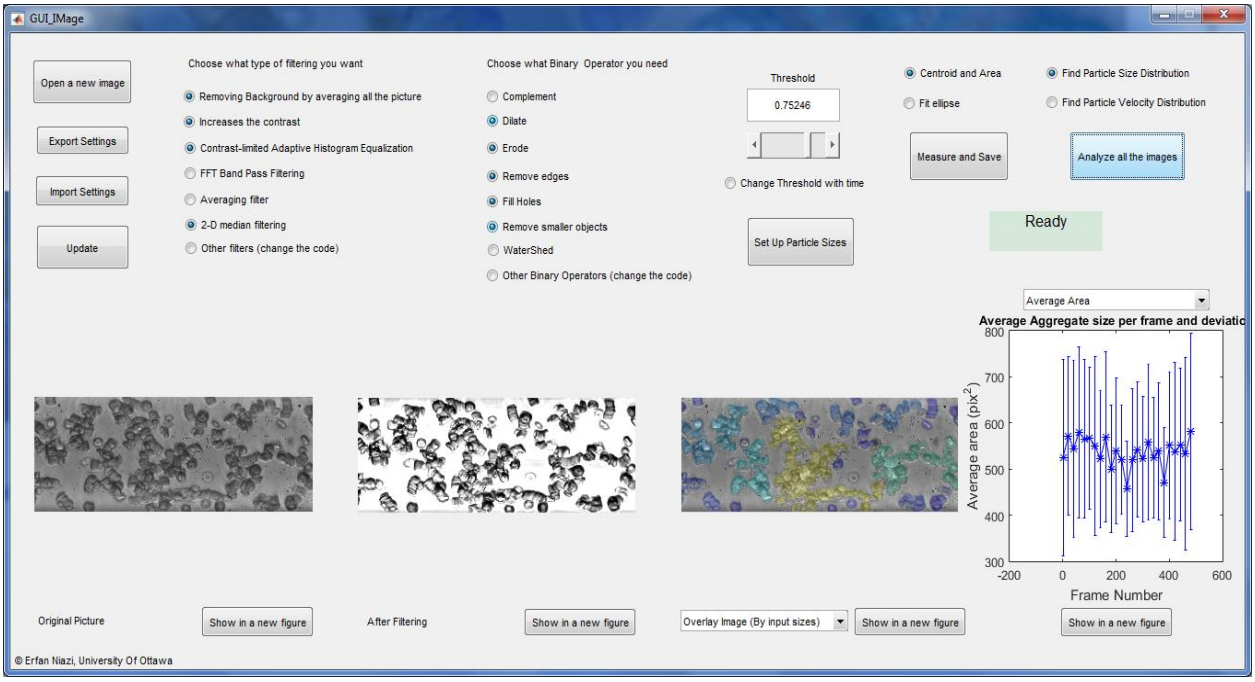

Figure 4.8: The Matlab graphical user interface developed for image processing.

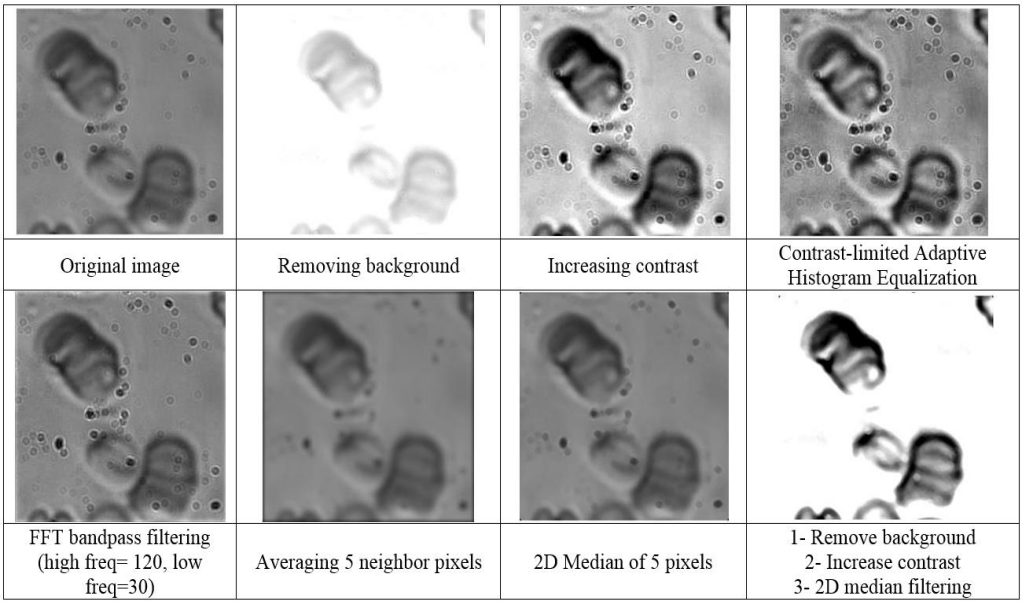

Figure 4.9: Effects of each image enhancement available in the image processing code

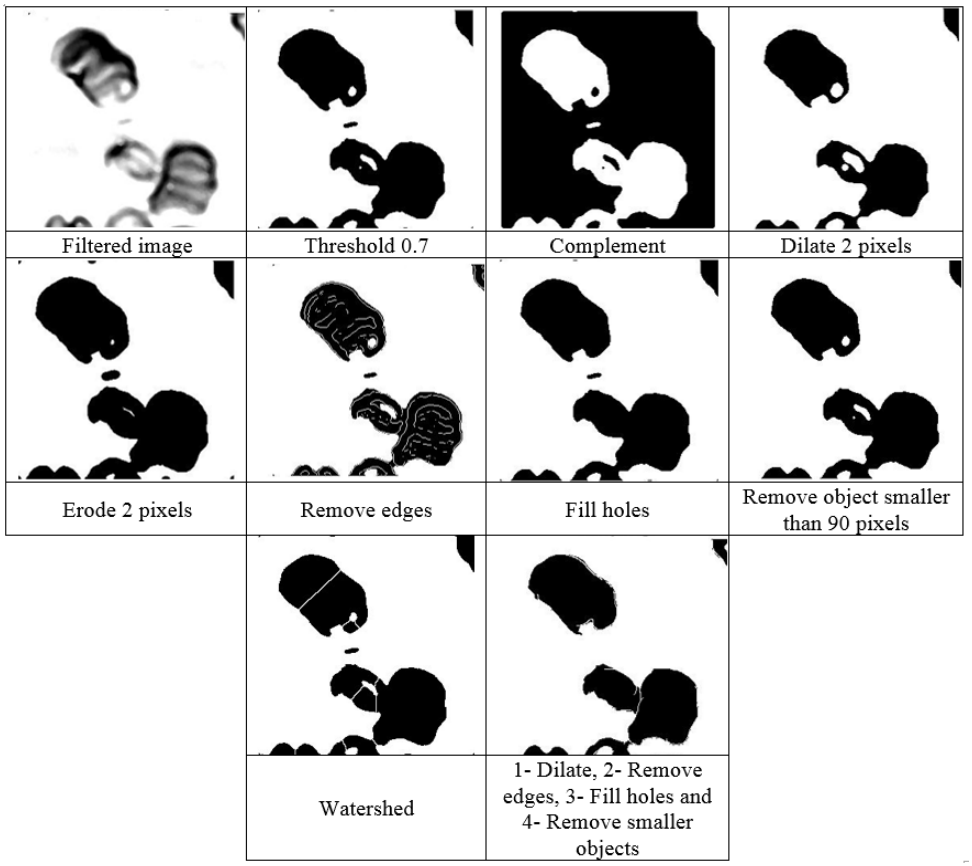

Figure 4.10: The effects of each binary operator available in the image-processing code.

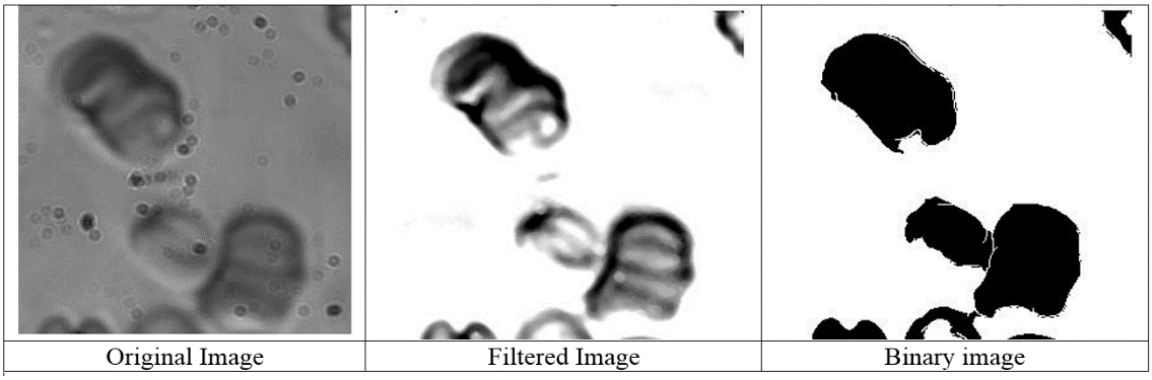

Figure 4.11: Applying a correct set of filter and binary operators to an image.

Each image, depending on the image acquisition system and lighting system, has its own characteristics and requires different filters and binary operators. Once the right filters and binary operators are found, the user can use the "export setting" option in the interface to save the whole procedure for analysis. This option makes a file which can be imported later by using the "Import setting" option.

After processing a set of pictures, each object in the image is approximated and classified as a disk with a predefined radius according to user input. Depending on the lens used for the image acquisition system and pixel density of the image, the size of particles can be determined in pixels. The user can change these settings by clicking on "set up particle sizes" in the interface. These results can be converted into rouleaux size, expressed in micrometers, later. Once the user is satisfied with the quality of the binary images, the specific information that will be output is selected from the GUI. This can include: 1- Centre of mass position, 2- Area, 3- Major and minor axes of the fitted ellipse, 4- Angle of the ellipse, 5- Particle size distribution in each class, 6- Velocity distribution of each class and 7- Collision rate of particles between each class. The workflow for this code is illustrated in Figure 4.12.

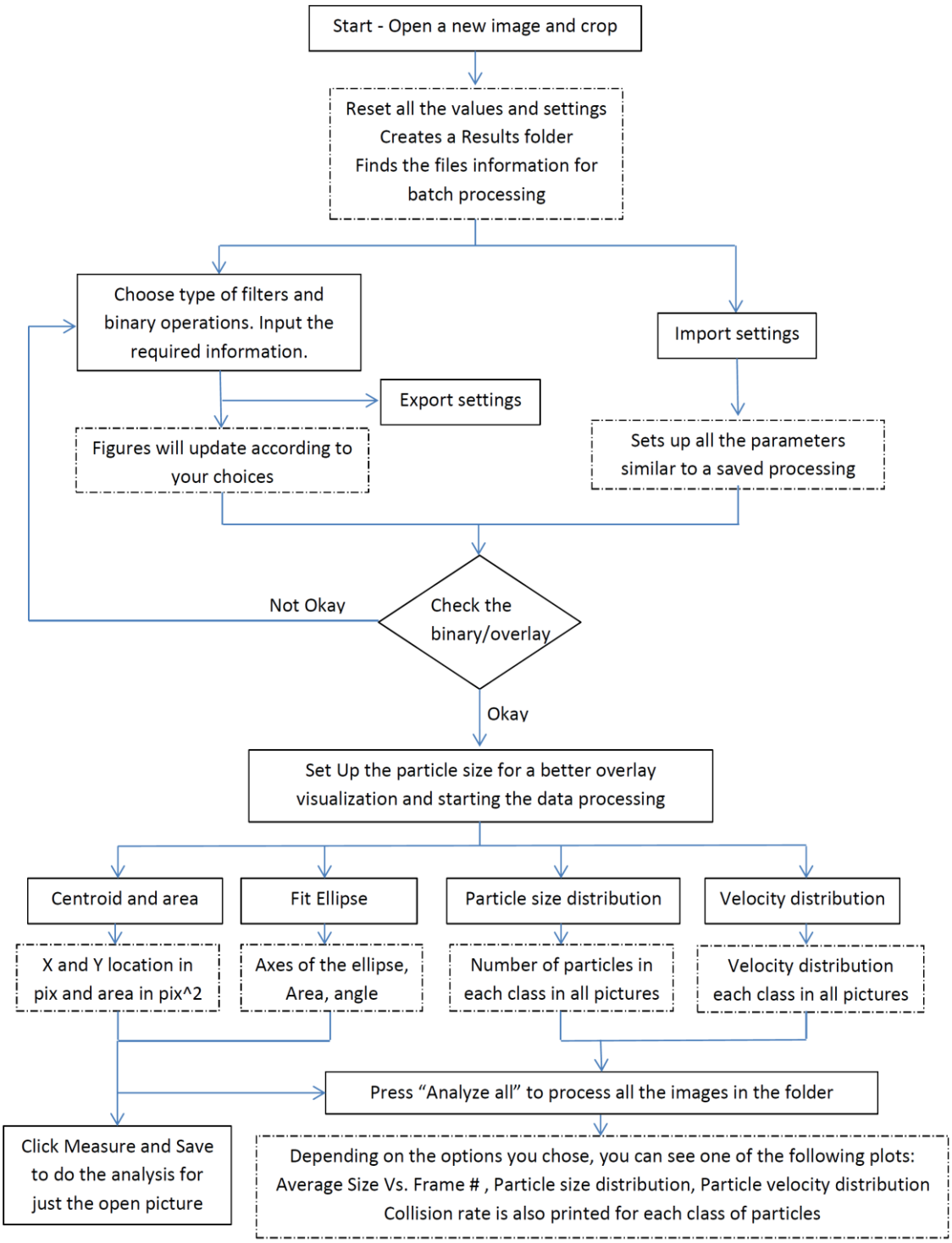

Figure 4.12: Workflow of the Matlab GUI for image-processing of images obtained during the red blood cell aggregation experiments.

Using these results, the number of particles in each class for each image can be found. Similarly, using this method, the distribution of the percentage of RBC within each aggregate as a function of the aggregate size, as well as the number of aggregates in different size ranges can be obtained. Particle-velocity distributions are another output of the code which is used to determine the collision rate. The number of aggregates in each size range, as well as the collision rate, are used to find aggregation and disaggregation rates later in Chapter 6.

4.5.2 Particle Size Measurements

There are two methods to measure the particle-size distribution. In the first method, particles are classified using a pixel range, as presented in Table 4-1. For this method, in each picture, a particle is added to a class if its area is in the range indicated in Table 4-1.

Table 4-1: Different aggregate sizes and their volumes for 10X magnification

Class κ	Area (pixel^2)	Corresponding Number of RBCs	Particle Volume v_κ (μm^3)	Pictures (not to scale)
1	25-60	1	90	
2	60-120	2	180	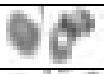
3	120-360	4	360	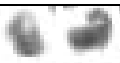
4	360-675	8	720	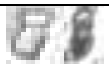
5	675-1500	16	1440	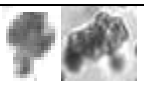
6	1500-2600	32	2880	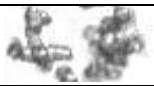
7	2600-5600	64	5760	
8	>5600	128 and more	11520	

This method does not represent correctly the total volume of particles, as all particles in a range are assigned the same representative volume. Therefore a method similar to that used in population-balance model is applied (Equations (3-7) to (3-10)) to distribute the particle. In this method, classes have a specific area assigned to them which is the average value of the range presented in Table 4-1. If a particle area is between two classes, it size would be distributed

between both classes in a way that conservation of volume is satisfied. This method is more reliable compared to the previous method because, each particle volume has an effect on the overall size distribution. In this research, different lens magnifications are used for experiments. In Appendix A, the definition of the particle-size classes for various experiments are summarized.

4.5.3 Particles Velocity Measurements

In order to use Equation (3-15) to find the collision rate between particles, velocity distributions of particles are needed. To find the velocity distribution of particles in different classes, two methods can be used.

In the first method, particle image velocimetry (PIV) is performed using an open-source Matlab tool called PIVlab [141]. This tool returns the particle velocity field, as shown in Figure 4.13. The limitation this particular PIV measurement imposes is that this method produces only a vector field and it does not specify velocities of individual particles. To solve this problem the location of individual particles, which comes from image processing, can be matched with the average of the velocity around that point. This method is not accurate enough, especially when smaller particles are in vicinity of larger particles.

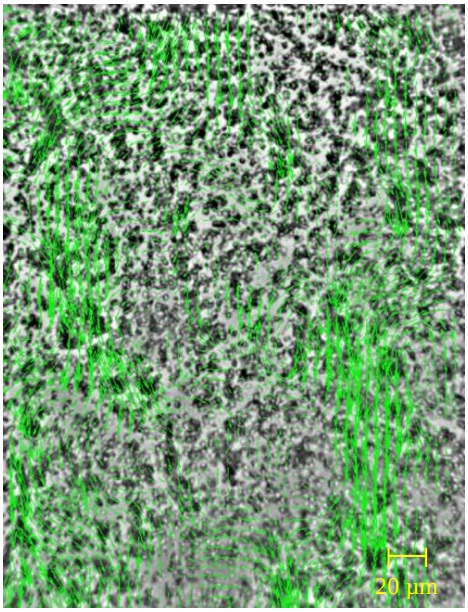

Figure 4.13: Particle velocity field produced using PIVlab for RBCs in a sedimentation experiment.

The second method that is used to find the particle velocity distribution aims to track each individual particle. This results in a more accurate velocity distribution for particles as a function of size. This method also has its own problems. For example, particles might disappear due to aggregation. Also the apparent size or centre of projected area might change suddenly due to overlapping particles. To face these problems, sudden changes are disregarded and if the particle is not found in next frame, it is considered to have disappeared. In these scenarios, the history of particle is saved until the time of its disappearance. The velocity found by this method is expected to be more accurate, although some particles might get lost. Since only the velocity distribution is important for this research application, this method is selected. The base code for this tracking method is available in Mathworks [142]. This code is modified to get its input from the image-processing code. To track particles, particles in each image are linked to the same particle in the next image as they move along in time. For frame to frame linking of particles the Hungarian algorithm (Munkres algorithm) [143] is used. In this method particles are linked according to their previous velocity and the guessed new location. The code looks for the nearest neighbour to the guessed location using Euclidean distance. If it cannot find a neighbour, that particle is not tracked anymore and no velocity is reported for it. In case of sudden appearance, either from aggregation or overlapping, the code uses a guessed velocity, which is the average velocity of particles in the same size, to find its possible location in the coming frame. To start this code, an initial guess for velocity is needed which comes from the first method discussed. It is important to note that in Equation (3-15), velocities in the z direction are needed. The experimental results only give velocities in x and y direction. To have an estimation for the z direction velocities for each particle, a random y velocity is used.

4.5.4 Fitting Ellipse to Rouleaux

Another feature of the code is fitting an ellipse to the detected particle. The code will fit an ellipse to the particle and shrink it to have the same pixel area. Both major and minor axes of each ellipse are saved in a file. In addition, the angle of the ellipse is also measured. Figure 4.14 shows an example of this fitting, for better visualization the shrunken ellipse is not shown and just the best fit is shown. The semi-axes of particles are needed in both the drag calculation and the intrinsic viscosity calculation for solution of ellipsoidal particles as discussed in the previous chapter. These results are presented in Chapter 6.

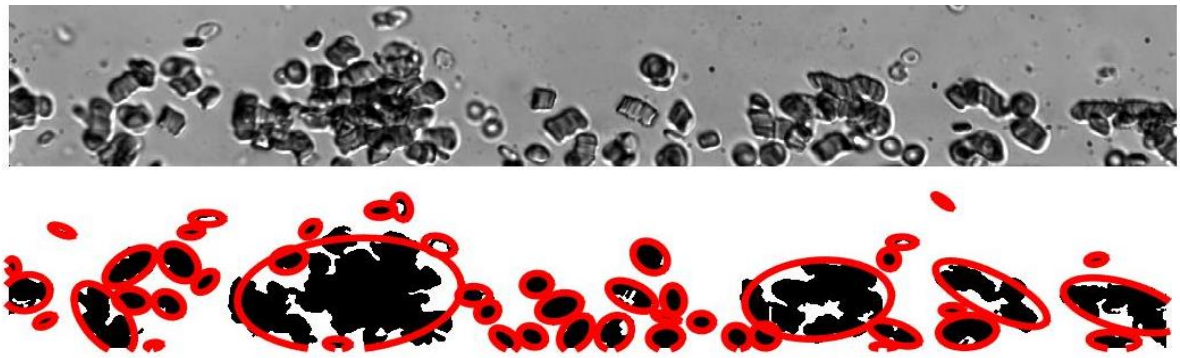

Figure 4.14: Fitting ellipse shapes to the detected particles

4.5.5 Verification

In this section the image processing method used to find aggregates size is verified. Verified results include rouleaux size and their velocities. For checking particle size measurements, manual measurement is compared with automatic measurement using Matlab GUI and ImageJ software results. For velocity distributions, automatic measurements of Matlab GUI, ImageJ software and PIVlab are compared.

ImageJ is an open source image processing and analysis software written in the Java programing language [144]. It is mostly used for proof of concept and to verify the image processing results in this research. It has similar steps and function as the developed GUI. For example, in the sedimentation test, the image processing starts by cropping the image. To find the background, the z-project function [145] is used to find the maximum intensity of all pictures. Then, by subtracting the background, a clearer picture for the image analysis is found. Bandpass FFT filtering [146] is applied to the images to get a better picture of the RBCs. Images are then converted to a binary image based on a threshold value. These cells are then labelled and the information on each detected particle is saved in a file. Resulting images are shown in Figure 4.15. Particle velocity measurement is done using the MtrackJ plugin in the ImageJ software. This tracking plugin uses tracking methods from Meijering *et al.* [147]. Further information on this plugin can be found in [148].

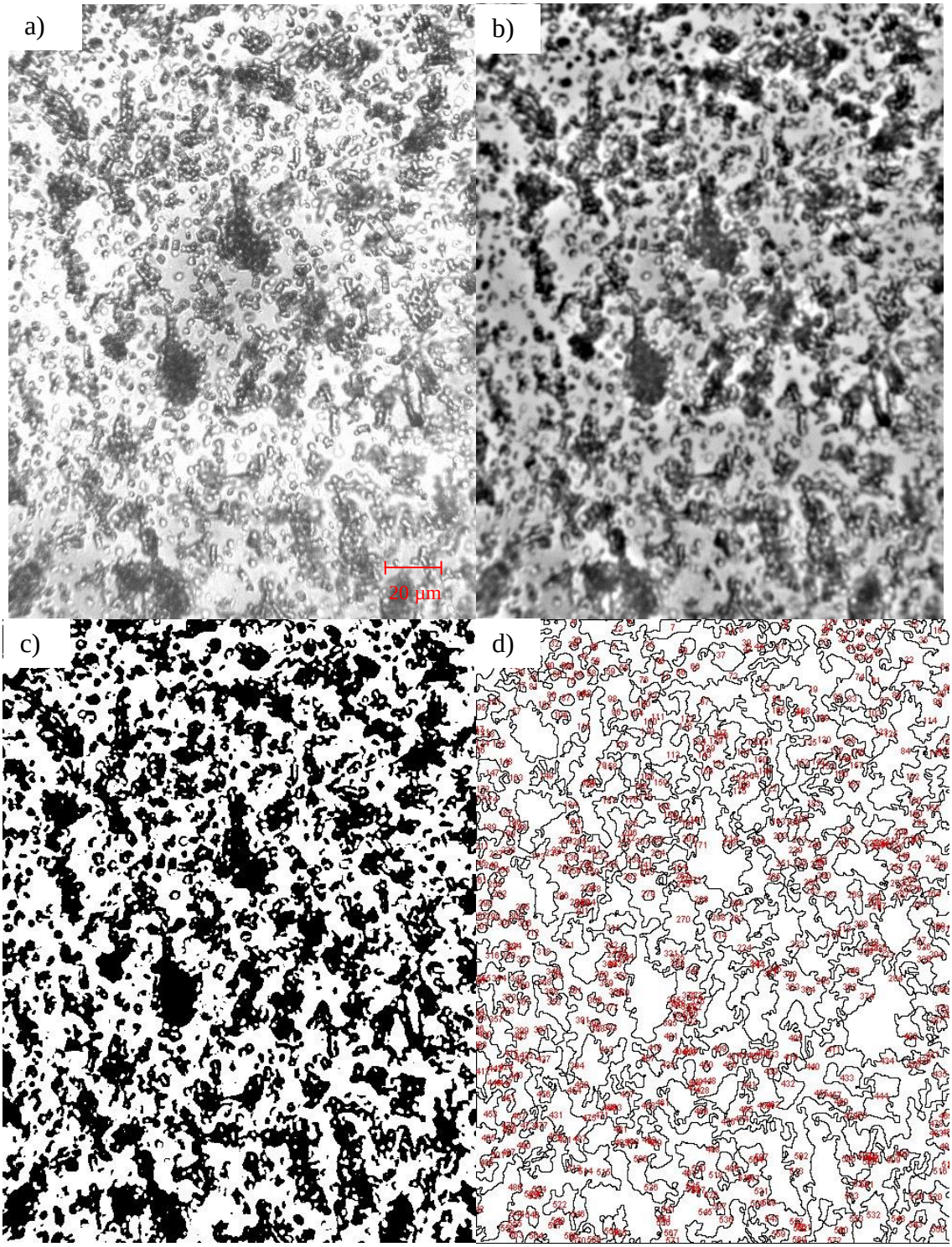

Figure 4.15: (a) Cropped image (b) Removing the background and filtering (c) Binary image (d) Analyzed picture.

To compare the manual size measurement to the Matlab GUI or ImageJ measurements, different sections of images are selected and cropped for comparison (total number of 20 sections). Figure 4.16 shows one of these analyses. For RBC aggregation size quantification, Figure 4.17 compares the percentage of particles detected in each range of particle size for both manual measurements and automatic measurement. A similar method is used for Couette flow by Mehri *et al*. [13].

Similarly, Figure 4.18 shows the comparison for velocity distribution found using Matlab GUI and the MtrackJ plugin in the ImageJ software. Manual measurement is not possible in this case and only two frames with mostly single RBCs is used for this comparison. As it can be seen, ImageJ and Matlab GUI detect similar behaviour in these two pictures.

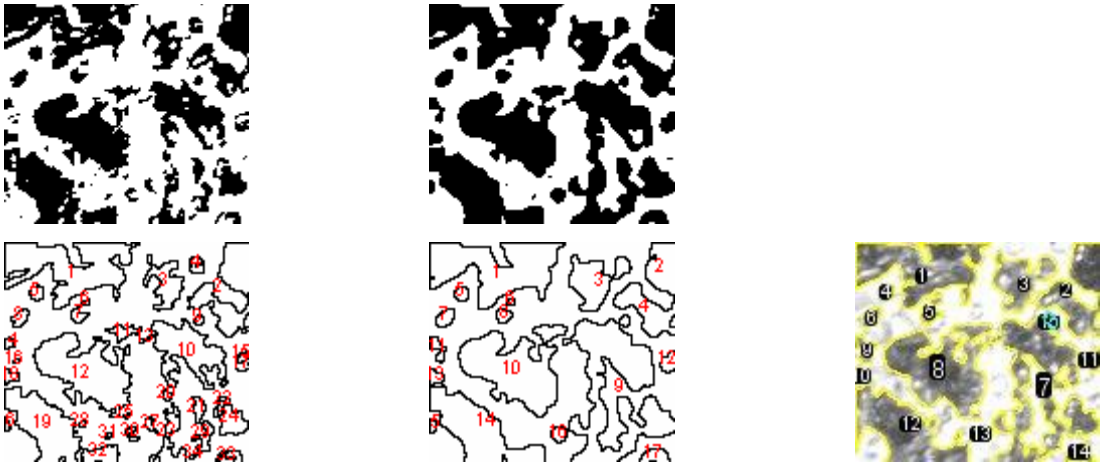

a) Without filtering b) After filtering c) Manual measurements

Figure 4.16: Image processing verification for rouleaux size measurements.

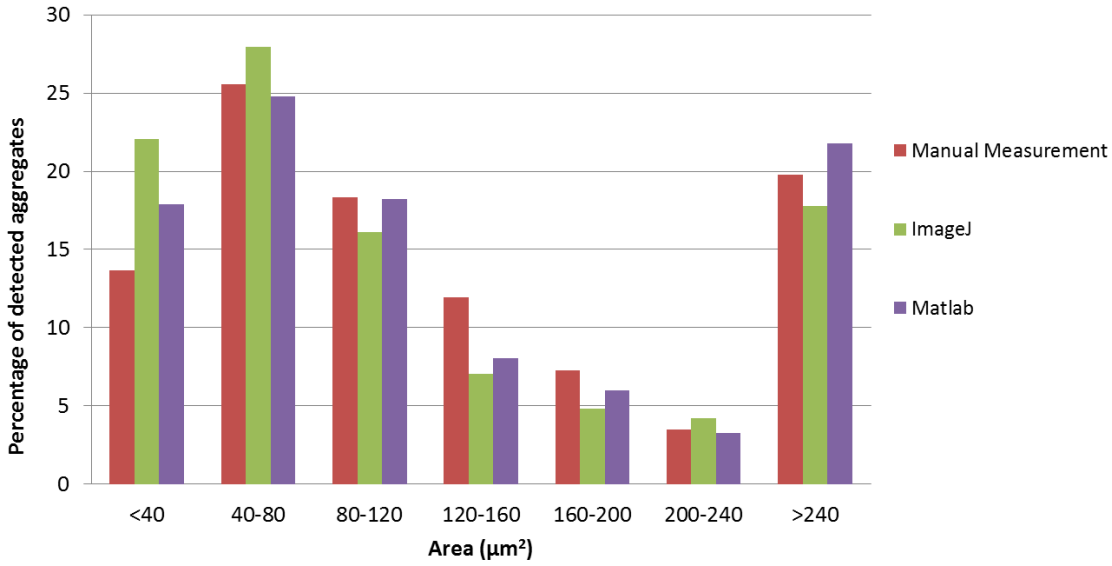

Figure 4.17: Percentage of particles in each aggregate size, manual measurements versus automated measurement by ImageJ and Matlab GUI.

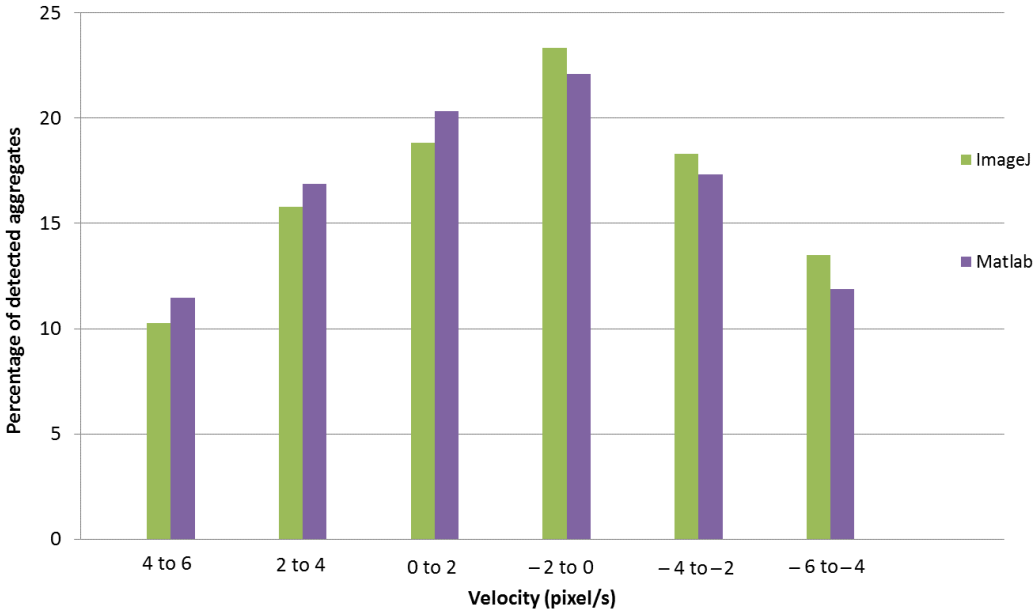

Figure 4.18: Velocity distribution between just two frames, Matlab GUI versus ImageJ.

4.6 Summary

In order to implement an expression for the aggregation and disaggregation rates in the numerical model, experiments are required. Experimental techniques used to calculate the size distribution of aggregated RBCs were presented in this chapter. Micro channel fabrication, blood sample preparation are also explained. Image processing software used and different method of analyzing the images are also covered. It is shown that using filtering and background removal provides a more accurate result. Table 4-2 summarizes the image processing technique used in each experiment and specifies the pixel to μm ratio for each lens magnification. In Chapter 5, after explaining the numerical model, the implementation of the experimental results into the numerical model is discussed.

Table 4-2: Image processing techniques used in each experiment

Experiment	Lens Magnification	Image Filters	Binary Operators	Pixel to μm
Sedimentation	10X	Removing Background, Increase Contrast, Adaptive Histogram Equalization and FFT filtering.	Removing Edges, and Remove Smaller Objects (2 pix).	0.956
Couette flow	20X	Removing Background, Increase Contrast, Averaging and 2D Median Filtering.	Dilate and Erode (2 pix), Removing Edges, Fill Holes, Remove Smaller Objects (20 pix).	0.238
Channel flow	40X	Removing Background, Increase Contrast and 2D Median Filtering.	Dilate (1 pix), Remove Edges, Fill Holes and Remove Smaller Objects (40 pix).	0.122

Chapter 5

Numerical Modelling

5.1 Introduction

A brief overview of population-balance modelling and the role of aggregation and disaggregation is given in Chapter 3. In this chapter, more details on the actual numerical implementation are given. The numerical code is developed in FORTRAN using Cartesian coordinates and structured meshes. This model is confined to 2D simulations due to the heavy calculations involved in 3D modelling. The transient semi-implicit method for pressure linked equations, corrected (SIMPLEC) method [149] is used to discretize the incompressible Navier-Stokes equations for the background fluid. This method results in a first-order accurate model in time and second-order accurate model in space. The particle phase is treated with a Godunov-type finite-volume scheme using the local Lax-Friedrichs flux function [150] for inter-cellular flux calculation. This method is first-order accurate in time. To achieve second-order accuracy in space, linear reconstruction with the minmod slope limiter method [150] is used.

In this chapter, first, the coupling of the fluid flow equations with particle equations is discussed. The discretization method for all the equations is explained in detail in Section 5.3. The computational structure of the model, which includes a coupled Navier-Stokes equation with the population-balance equation, is described in Section 5.4. Section 5.5 is devoted to steps taken to verify the correct implementation of the numerical code. And Section 5.6 gives more detail about the case studies done in this research, including: sedimentation test, Couette flow and channel flow.

5.2 Two-way Coupling of Background Fluid and Particles

As discussed in Section 3.6, this model is made of three separate, yet not independent, components. These pieces are the Navier-Stokes equations (Equations (3-18) to (3-20)) for base fluid flow, a momentum equation for each particle class in the flow (Equations (3-22) to (3-23)) and finally, the population-balance equation (Equation (3-4)). Their dependence on each other is shown in Figure 5.1 for the two-way coupling method. This figure shows that for a complete two-way coupled model, all these equations must be solved simultaneously. In a normal scenario, where eight classes of particle are used, 3 equations are solved for the base fluid, 8 population-balance equations are solved for particle density and 16 equations are solved to find

the momentum density of each particles family. These 27 equations are highly dependent on each other and cannot be solved separately.

As illustrated in Figure 5.1, the population-balance equation (Equation (3-4)) solves for the particle mass density, ρ_κ, for each class of particle. By using the particle density and Equation (3-21), the volume fraction of the background fluid can be found at any point. This parameter is used in the continuity equation for the plasma to find the background fluid velocity field. From this velocity field, shear stress, τ, and shear rate, $\dot{\gamma}$, can be computed. These parameters are used to calculate the breakage rate, as discussed in Section 3.5. The base fluid velocity field is also used in finding the drag force on particles (Equation (3-31)). Therefore, the momentum equation for each particle family can be solved only when base fluid velocity field and particle distribution in each class are known. The momentum equation provides the particle velocity field for each particle class, which is used in the population-balance (Equation (3-4)) to find particle distribution in the domain and the volume fraction, α. In the same section of the model, the forces applied on a class of particle are calculated using Equations (3-26) to (3-35). The same force is applied on the base fluid in the opposite direction as a reaction force.

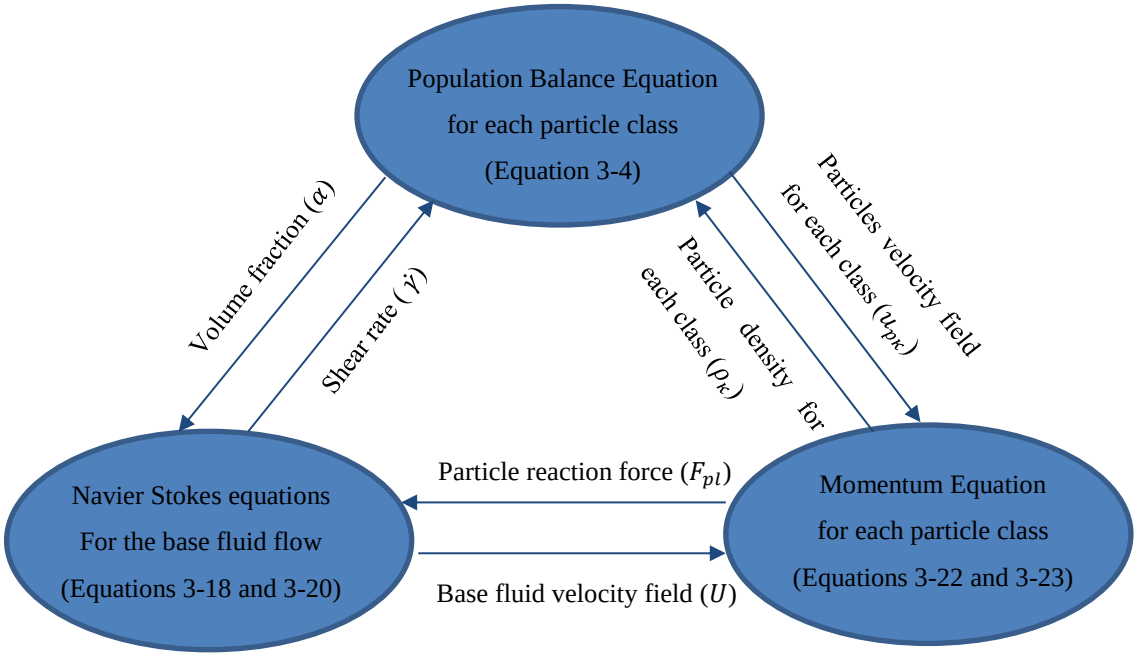

Figure 5.1: Relations between different parameters in the model

5.3 Discretization Method

The present numerical code is built from a combination of two coupled solvers. The first solver is developed to solve for particle movement using Equations (3-4), (3-22) and (3-23). This Godunov-type finite-volume scheme uses the local Lax-Friedrichs flux function with piecewise linear reconstruction in space along with the minmod slope limiter [150]. The second solver is developed to solve the Navier-Stokes equations for the background fluid. This code uses the SIMPLEC method [149] to discretize the equations. In the next subsections, these two solvers and their discretization method are discussed in more detail.

5.3.1 Particle Solver

Equations (3-4), (3-22) and (3-23) form a system of first order hyperbolic partial differential equations (PDEs) that describe the evolution of the particle phase. These equations can be written as

$$\frac{\partial U}{\partial t}+\frac{\partial F_x}{\partial x}+\frac{\partial F_y}{\partial y}=S\,, \tag{5-1}$$

where U is a vector of conserved variables and F is the flux dyad. The parameter S is the source term which considers particle aggregation, disaggregation, momentum transfer due to aggregation and disaggregation and all the forces applied to the particles. This term is discussed later in this chapter. The solution vector and fluxes for one family, κ, are

$$U=\begin{pmatrix}\rho_\kappa\\ \rho_\kappa u_{x\kappa}\\ \rho_\kappa u_{y\kappa}\end{pmatrix}\quad,\quad F_x=\begin{pmatrix}\rho_\kappa u_{x\kappa}\\ \rho_\kappa u_{x\kappa}^2+P\\ \rho_\kappa u_{y\kappa}u_{x\kappa}\end{pmatrix}\quad\text{and}\quad F_y=\begin{pmatrix}\rho_\kappa u_{y\kappa}\\ \rho_\kappa u_{y\kappa}u_{x\kappa}\\ \rho_\kappa u_{y\kappa}^2+P\end{pmatrix}. \tag{5-2}$$

A finite-volume method is applied to solve this hyperbolic set of equations. This involves, first, discretizing the problem domain into non-overlapping volumes that are fixed in time. The governing equations can then be integrated on one volume to give

$$\iiint_V \left(\frac{\partial U}{\partial t} + \nabla \cdot F \right) \mathrm{d}V = \iiint_V S \ \mathrm{d}V \,. \tag{5-3}$$

By splitting the integral into two components and by using the divergence theorem, Equation (5-3) can be rewritten as

$$\frac{d}{dt} \iiint_V U \, \mathrm{d}V + \oiint_A F \cdot \hat{n} \, \mathrm{d}A = \iiint_V S \, \mathrm{d}V \,. \tag{5-4}$$

By defining the cell-average value of the solution vector as $\bar{U} = \frac{1}{V} \iiint_V U \ \mathrm{d}V$ and the average value of the source term as $\bar{S} = \frac{1}{V} \iiint_V S \ \mathrm{d}V$, Equation (5-4) can be rewritten as

$$\frac{d\bar{U}}{dt} = -\frac{1}{V} \oiint_A F \cdot \hat{n} \, \mathrm{d}A + \bar{S} \,. \tag{5-5}$$

For simplicity, the overbar notation on the solution vector and source term are omitted in the remainder of this chapter.

When Equation (5-5) is applied to a two-dimensional control-volume that is bounded by four straight edges [150], it can be written as

$$\frac{\partial U_{i,j}}{\partial t} + \frac{1}{A_{i,j}} \sum_{k=1}^{4} \left(F \,.\, \hat{n} \, \Delta l \right)_k = S_{i,j} \,. \tag{5-6}$$

In this equation, indices *i* and *j* shows the index of the control-volume in a two-dimensional structured Cartesian grid in the *x* and *y* directions respectively. The index *k* is used to show the number of the edges of a particular cell. In the second term, fluxes on each edge should be calculated and multiplied by the edge length, Δl. According to Equation (5-5), this sum should be divided by the volume of the control volume. As the control-volume is two-dimensional, this volume changes to the area of the cell, $A_{i,j}$. The area of the cell can be calculated as $A_{i,j} = \Delta x \, \Delta y$ where Δx and Δy are the cell size in *x* and *y* directions respectively. Further information about the computational cells is shown in Figure 5.2.

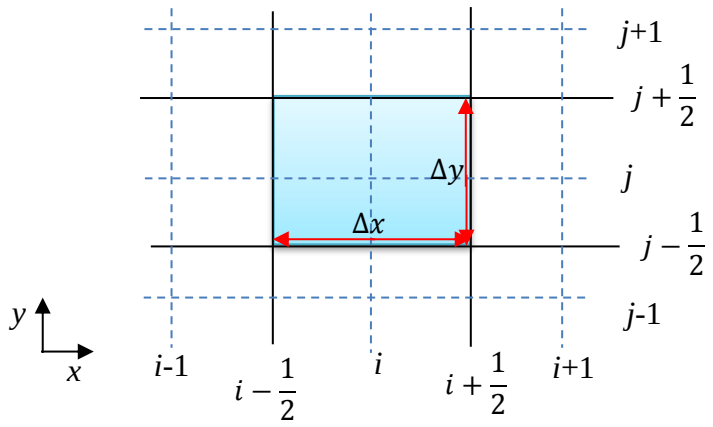

Figure 5.2: An example of a computational cell for the particle solver scheme

In order to obtain a second-order accurate solution in space, flux evaluations are carried out using the local Lax-Friedrichs method and by using piece-wise linear solution reconstruction within each cell. In the present work, *x*- and *y*-direction solution derivatives are computed independently and limited using the minmod limiter. Fluxes are then calculated based on the reconstructed solution state at the midpoint of each cell interface. For simplicity, this procedure is demonstrated in the *x*-direction only. Similar equations can be derived for the *y*-direction. The flux on the right boundary and between cell $(i,\ j)$ and cell $(i+1,\ j)$ is function of the state on either side of the interface,

$$F_{i+\frac{1}{2},j} = f\left(\left(U+\frac{\Delta x}{2}\frac{\partial U}{\partial x}\right)_{i,j},\left(U-\frac{\Delta x}{2}\frac{\partial U}{\partial x}\right)_{i+1,j}\right), \tag{5-7}$$

where $\frac{\partial U}{\partial x}$ in each cell is calculated using the minmod limiter method [150]. In this method the forward-difference, $\left[\frac{\partial U}{\partial x}\right]_{FD}$, and the backward-difference, $\left[\frac{\partial U}{\partial x}\right]_{BD}$, schemes are used to find the slope between two neighbour cells using

$$\begin{aligned}\left[\frac{\partial U}{\partial x}\right]_{FD} &= \frac{U_{i+1,j}-U_{i,j}}{\Delta x},\\ \left[\frac{\partial U}{\partial x}\right]_{BD} &= \frac{U_{i,j}-U_{i-1,j}}{\Delta x}.\end{aligned} \tag{5-8}$$

These slopes are then compared and the slope with the minimum modulus is chosen if they have the same sign. Otherwise, this function returns zero. This can be expressed mathematically as

$$\left[\frac{\partial U}{\partial x}\right]_{i,j} = \begin{cases} \left[\frac{\partial U}{\partial x}\right]_{FD} & \text{if } \left|\left[\frac{\partial U}{\partial x}\right]_{FD}\right| < \left|\left[\frac{\partial U}{\partial x}\right]_{BD}\right| \text{ and } \left[\frac{\partial U}{\partial x}\right]_{FD} . \left[\frac{\partial U}{\partial x}\right]_{BD} > 0 \\ \left[\frac{\partial U}{\partial x}\right]_{BD} & \text{if } \left|\left[\frac{\partial U}{\partial x}\right]_{FD}\right| > \left|\left[\frac{\partial U}{\partial x}\right]_{BD}\right| \text{ and } \left[\frac{\partial U}{\partial x}\right]_{FD} . \left[\frac{\partial U}{\partial x}\right]_{BD} > 0 \\ 0 & \text{if } \left[\frac{\partial U}{\partial x}\right]_{FD} . \left[\frac{\partial U}{\partial x}\right]_{BD} \le 0 \end{cases} . \tag{5-9}$$

Looking back at the Equation (5-7), now that $\left.\frac{\partial U}{\partial x}\right|_{i,j}$ is defined, the only thing that remains to be defined is the function used to calculate the fluxes. The local Lax-Friedrichs method [150] is used for these calculations. For neighbour cells of (i, j) and ($i+1$, j), it can be written as

$$F_{i+\frac{1}{2},j} = \frac{1}{2}\left[F'_{i,j} + F'_{i+1,j} - \left|\lambda_{i+\frac{1}{2},j}\right| \left(\left(U + \frac{\Delta x}{2}\frac{\partial U}{\partial x} \right)_{i+1,j} - \left(U - \frac{\Delta x}{2}\frac{\partial U}{\partial x} \right)_{i,j} \right) \right]. \tag{5-10}$$

Where $F'_{i,j}$ is the flux of Equation (5-2) and reconstructed average values $\left(U + \frac{\Delta x}{2}\frac{\partial U}{\partial x} \right)_{i,j}$. The parameter, λ, is the maximum local speed of information propagation, calculated using particle velocities u_p for each family as

$$\lambda_{i+\frac{1}{2},j} = \max\left(\left|u_{i,j}\right| + \sqrt{\frac{1}{\rho_{i,j}}\left.\frac{\partial P}{\partial \alpha}\right|_{i,j}} , \left|u_{i+1,j}\right| + \sqrt{\frac{1}{\rho_{i+1,j}}\left.\frac{\partial P}{\partial \alpha}\right|_{i+1,j}} \right). \tag{5-11}$$

These speeds are found from the eigenvalues of the *x*-direction flux Jacobian. In order to ensure numerical stability for explicit time marching, these wave speeds are also used to limit the time step size,

$$\Delta t = \min_{i,j}\left(C\frac{\Delta x}{\lambda_x} \quad , \quad C\frac{\Delta y}{\lambda_y} \right)_{i,j}, \tag{5-12}$$

where C is the Courant–Friedrichs–Lewy (CFL) number. In this research, $C = 0.8$ is used, unless otherwise stated. The symbols λ_x and λ_y are the fastest wave speeds in *x*- and *y*-directions respectively.

Now that the time step, Δt, is found, the time discretization in Equation (5-6) can be discussed further. As we are interested mostly in steady-states solutions, a first-order accurate model in time is sufficient. The explicit Euler method is chosen. It can be written as

$$\frac{\partial U_{i,j}}{\partial t} = \frac{U_{i,j}^{n+1} - U_{i,j}^{n}}{\Delta t} = -\frac{1}{A_{i,j}} \sum_{k=1}^{4} \left(F \cdot \hat{n}\, \Delta l \right)_k^n + S^n{}_{i,j} + \hat{S}_{i,j}^{n+1}. \tag{5-13}$$

Where the index n denotes the current time step and $n+1$ denotes the next time step. This explicit time marching method is simple and numerically cheap, which can allow steady-state to be found quickly. By adding the source terms, explained in Section 5.3.4, the particle solver discretization is complete. The source term includes particle and momentum transfer between classes and the interaction forces between background fluid and particles. It is important to mention the drag force is treated implicitly and therefore $\hat{S}_{i,j}^{n+1}$ is included in the Equation (5-13). The details of the local source implementation are discussed later.

5.3.2 Incompressible Navier-Stokes Solver

The previously described particle solver is coupled to the background flow through the fluid forces. The background fluid is modelled as an incompressible Newtonian fluid. It is treated numerically using the SIMPLEC method on Cartesian meshes [149].

In the SIMPLEC method, the pressure field is found indirectly by ensuring that the continuity equation is satisfied, taking into account the volume of fluid that is displaced by the presence of particles. In other words, the method first solves the momentum equations with a fixed pressure field. The predicted velocity field will not be divergence free, therefore the continuity equation is used to compute a pressure correction to force the divergence-free

condition. The SIMPLEC method uses a staggered grid where the scalar pressure and density are saved in the cell centers of each control volume, and the velocities are stored on the midpoint of the cell faces. Details of the SIMPLEC method are given in Appendix B [149].

5.3.3 Staggered Grid

As the solver for background flow uses a staggered grid, it is important that information is passed correctly between the two solvers. The SIMPLEC method uses the staggered grid shown in Figure 5.3 (a), where scalar parameters are saved in the centre of the control-volume and velocities are saved at the midpoint of the surfaces of control volume. The velocities in the cell centre can be found by averaging the velocities on the surfaces. In this figure indices i and j are used for showing the particle solver cell centers, indices i' and j' are used to show the cell surface location in the background solver and finally, indices I and J are used to show the location of fluid solver cell centre, where the scalar parameters are saved. As can be seen in Figure 5.3, there is an offset of 1 when moving from the fluid solver location to the particle solver. Looking at this figure, the following statements can be derived to relate both codes grids

$$u_{f(i,j)} = \frac{\left(u_{f(i',J+1)} + u_{f(i'+1,J+1)}\right)}{2}, \qquad v_{f(i,j)} = \frac{\left(v_{f(I+1,j')} + v_{f(I+1,j'+1)}\right)}{2}. \tag{5-14}$$

Similarly for the Navier-Stokes grid, it can be written as

$$u_{p(i',J)} = \frac{\left(u_{p(i-1,j-1)} + u_{p(i,j-1)}\right)}{2}, \qquad v_{p(I,j')} = \frac{\left(v_{p(i-1,j-1)} + v_{p(i-1,j)}\right)}{2}, \qquad u_{p(I,J)} = u_{p(i-1,j-1)}, \qquad v_{p(I,J)} = v_{p(i-1,j-1)}. \tag{5-15}$$

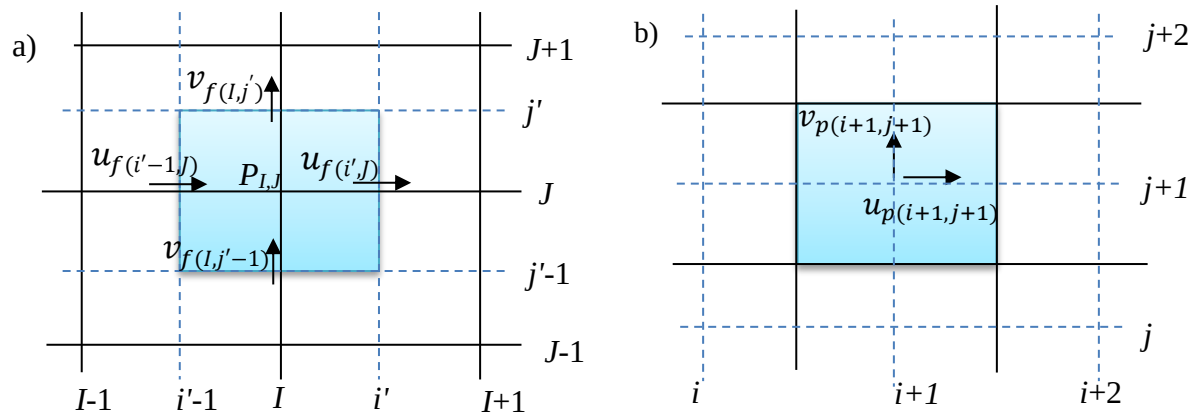

Figure 5.3: (a) Staggered grid used to solve the background fluid. (b) Collocated grid used to solve the particle flow.

5.3.4 Source Terms

The momentum exchange between the particle phase and the fluid occurs due to forces between the two phases. These forces are gravity, drag, lift and added drag force due to virtual mass in both directions and can be written as

$$F_{Particle} = \sum F_{pi} = \sum F_{g\kappa} + F_{D\kappa} + F_{L\kappa} + F_{VM\kappa} . \tag{5-16}$$

These forces were introduced in Section 3.7. At a computational cell, in a discretized time, Δt, the momentum transfer is equal to $F_{Particle} \times \Delta t$.

The gravitational force on the particles in class κ inside a cell can be written as

$$F_g = -\left(\left(\rho_p - \rho_f\right) Vol_\kappa \, g\right)_{i,j} \tag{5-17}$$

where Vol_κ is the volume occupied by particles in class κ, and are given in Table 4-1. Density of RBCs, ρ_p, is constant and is 1125 kg/m^3. The density of the background fluid, plasma, ρ_f, is also constant and is equal to 1025 kg/m^3. The acceleration due to gravity, g, is 9.81 m/s^2 and this force is applied only in *y*-direction.

The drag force can be calculated either for spherical particles or elliptical particles (Section 3.7.3). For simplicity, in this section, it is assumed that particles are spherical and the particle Reynolds number is small. Using these assumptions, the Stokes drag formulation can be applied as follow for *x*-direction

$$F_D = -6\pi d_\kappa \mu_f \left(u_{\kappa(i,j)}^{n+1} - u_{f(i,j)}^{m+1} \right), \tag{5-18}$$

where the particle diameter, d_κ, is calculated form its volume given in Table 4-1. A similar equation can be written for the *y*-direction drag force. This force is treated fully implicitly in the particle solver. The term with $n+1$ indices will appear in the $\widehat{S}_{i,j}^{n+1}$ term in the Equation (5-13). This fully implicit treatment is due to stiffness that this term imposes on the hyperbolic equations, which makes the equations have stability problems. In these equations $m+1$ in the upper indices indicates fluid solver inner loop iteration that is discussed in the Section 5-4 or in more details in Appendix B.

The lift force is mainly generated by the background fluid movement. The following equation is written for the *x*-direction velocities and the force is applied as a source term in *y*-direction momentum equation. In a computational cell this force can be calculated as

$$F_L = -\left(1.96 \frac{\left(u_{\kappa(i,j)}^{m+1} - u_{f(i,j)}{}^{m+1} \right) \omega_{i,j}}{\mathrm{Re}_p^{0.5}} \left(\frac{2\left| u_{\kappa(i,j)}^{m+1} - u_{f(i,j)}{}^{m+1} \right|}{\left| \omega_{i,j} \right| d_\kappa} \right)^{0.5} \right). \tag{5-19}$$

where the particle Reynolds number in a computational cell is defined as

$$\mathrm{Re}_p = \frac{\rho_f \left(\left| u_{\kappa(i,j)} - u_{f(i,j)} \right| \right) d_\kappa}{\mu_f}. \tag{5-20}$$

Here the plasma viscosity, μ_f, is 1.1 mPa.s and the background fluid vorticity in a cell is defined as

$$\omega_{i,j} = \frac{v_{i,j+1}^{m+1} - v_{i,j-1}^{m+1}}{\Delta x} - \frac{u_{i+1,j}^{m+1} - u_{i-1,j}^{m+1}}{\Delta y}. \tag{5-21}$$

Finally, the added drag from the acceleration of particles (virtual mass) in a computational cell can be written as

$$F_{VM} = -0.9\bar{c}_M \left(\frac{u_{\kappa(i,j)}^{m+1} - u_{\kappa(i,j)}^{n}}{\Delta t} - \frac{u_{f(i,j)}^{m+1} - u_{f(i,j)}^{n}}{\Delta t} \right) \tag{5-22}$$

where, the added mass coefficient $\bar{c}_M$ is 0.5 for a spherical particle [10] is used for all simulations. Equation (5-22) shows this force in the *x*-direction and a similar equation can be written for the *y*-component.

5.3.5 Aggregation Function

Looking back at Equations (3-7) to (3-10) shows that the implementation of aggregation and disaggregation in the equations is essential. The numerical values for the aggregation and disaggregation rate are found experimentally in the next chapter. In this section, the numerical implementation of relevant source terms are discussed.

Particles can move between classes according to Equations (3-7) to (3-10). These equations are applied in each computational cell, the only difference is that, instead of number density of particles, the particle density itself is used to develop the solver. This difference only changes the units used in the equations. Another important note on the aggregation and disaggregation function is that, when particles are moving between classes, they also transfer their momentum along with them. For example, if the particle transfer between two sizes is $\Omega_{\kappa,\lambda}\rho_\kappa$, the momentum transfer would be $\Omega_{\kappa,\lambda}\rho_\kappa u_\kappa$, where ρ_κ and u_κ are the density and velocity of particles in the first class and $\Omega_{\kappa,\lambda}$ denotes the proportion of particles moving to the next class.

5.3.6 Boundary Conditions

There are three situations studied in this research: the sedimentation test, Couette flow and channel flow. In the sedimentation test, there are only wall boundary conditions. In the Couette flow, there are wall and periodic boundary conditions. Finally, in channel flow there are wall and inlet and outlet boundary conditions. In this section, the implementation of these boundary conditions for both solvers is discussed.

5.3.6.1 Wall Boundary Conditions

The wall boundary condition for the fluid flow simulation is treated by no slip and no penetration conditions. In the case of the particle flow solver, particles can reflect from the wall, which is equivalent to a no penetration condition. The no-slip boundary condition is not applied for the particle solver and particles are free to slip along the wall.

Figure 5.4 shows the wall boundary condition for the fluid solver. In the case of the fluid solver, looking at the Figure 5.4, applying the no penetration condition is fairly easy. For example, for the left wall (Figure 5.4), this boundary can be applied by putting all $u_{f(1,J)} = 0$. On the other hand, the no slip boundary condition should be applied in the next layer of the grid as there is not a velocity grid exactly on the wall. Therefore, the shear stress appears as a source term in the boundary condition. For example, for the bottom wall, the boundary conditions are shown in Figure 5.5. In this case, first, shear stress, τ_w, should be calculated. It can be assumed that the flow regime in these simulations is laminar. For the laminar flow the wall shear stress for the south boundary is

$$\tau_w = \mu \frac{2u_{f(i',2)}}{\Delta y}. \tag{5-23}$$

Next, this shear stress, should be applied as a source term for cells neighbouring the wall. In case of the South boundary, the J=2 cells would have this source term. A similar procedure should be done for North, East and West boundaries. In the case of moving wall, the relative velocity should be placed in the Equation (5-23).

For the particle solver code, to apply a no penetration boundary condition, a ghost cell is introduced beyond the wall boundary, as in Figure 5.6. To apply a no penetration boundary condition, this cell works as a mirror for velocities that are normal to the wall. For the free slip boundary and parallel to wall velocities, the ghost cell velocity follows the same state as the cell near the wall.

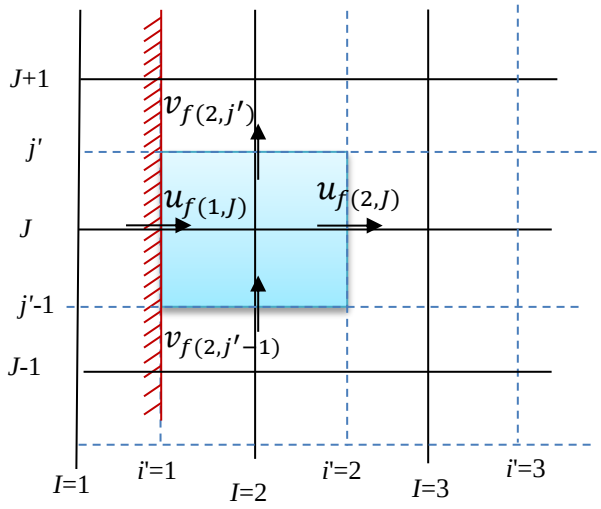

Figure 5.4: Wall boundary condition in staggered grid for the fluid solver.

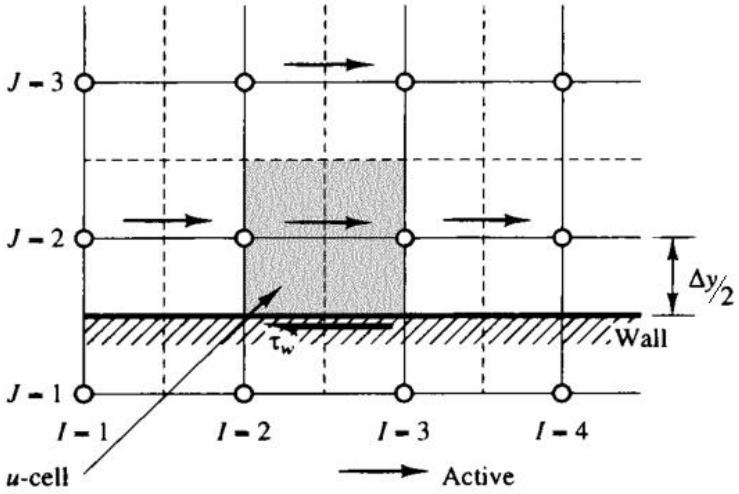

Figure 5.5: Applying no slip boundary condition for the fluid solver [149].

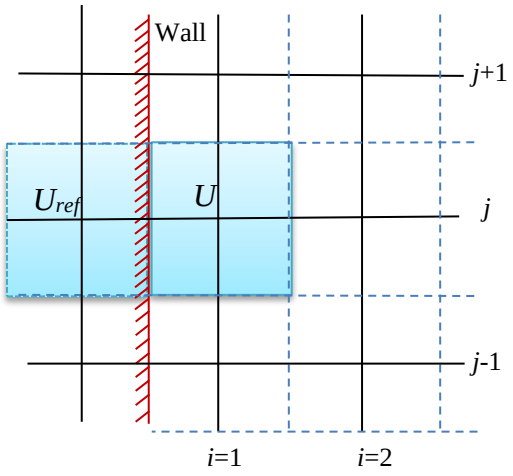

Figure 5.6: Applying a no penetration boundary condition for particle solver.

Figure 5.6 shows the boundary cells for the particle solver in the West wall. For the West wall boundary condition, it can be written as

$$U_{ref} = \begin{pmatrix} \rho_\kappa \\ -\rho_\kappa u_\kappa \\ \rho_\kappa v_\kappa \end{pmatrix}_{1,j} , \tag{5-24}$$

which results in zero particle flux for the particle solver in *x*-direction and does not change the states in the *y*-direction. In the case of the left boundary condition, fluxes on the wall are calculated using Equation (5-10), and, $U_{1,j}$ and U_{ref} as the neighbour states.

5.3.6.2 Periodic Boundary Condition

In the case of Couette flow, periodic boundary conditions must be considered where all the flow properties are identical at the inlet and outlet of domain. For the case of the fluid solver and between east and west boundaries, the velocity boundary condition are

$$u_{f(2,J)} = u_{f(Ni-1,J)} ,$$
$$v_{f(2,j')} = v_{f(Ni-1,j')} . \tag{5-25}$$

Here the term, N_i, indicates the maximum number of cells in the *x*-direction. Similarly, for the particle solver, the boundary condition is easily specified as

$$U_{1,j} = U_{Ni,j} \quad , \tag{5-26}$$

where *U* is the solution vector for the particle solver, defined in Equation (5-2).

5.3.6.3 Inlet and Outlet Boundary Conditions

In the case of the channel flow, inlet and outlet boundary conditions are applied for the fluid flow. For the particle solver, the same periodic condition as previously mentioned is suggested to simulate channel flow. The periodic condition is used so the cell-free layer formation can be studied.

Figure 5.7 shows where the inlet boundary conditions are applied. For example, for the West inlet boundary condition, pressure and velocities in the *x*- and *y*-directions should be all set according to

$$\begin{aligned} u_{f(2,J)} &= u_{in} \quad , \\ v_{f(1,j')} &= v_{in} \quad , \\ P_{1,J} &= P_{in} \quad , \end{aligned} \tag{5-27}$$

where u_{in} , v_{in} and P_{in} are given by the user.

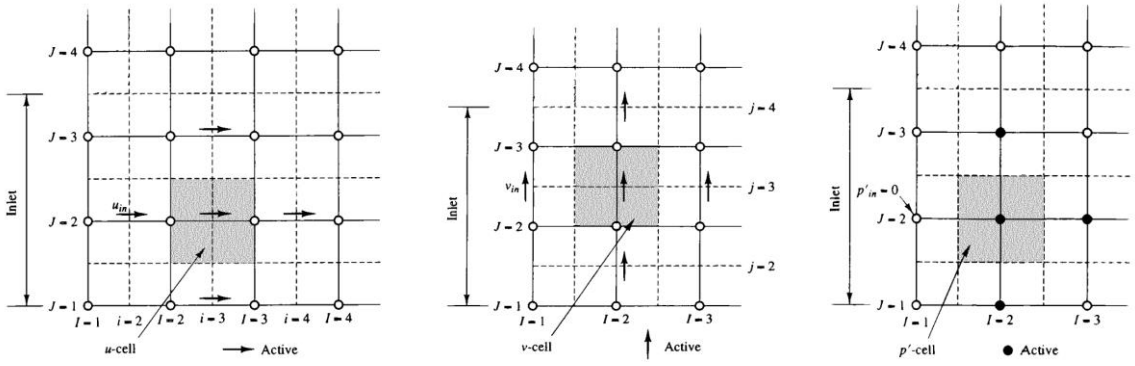

Figure 5.7: Inlet boundary condition for the fluid solver [149]

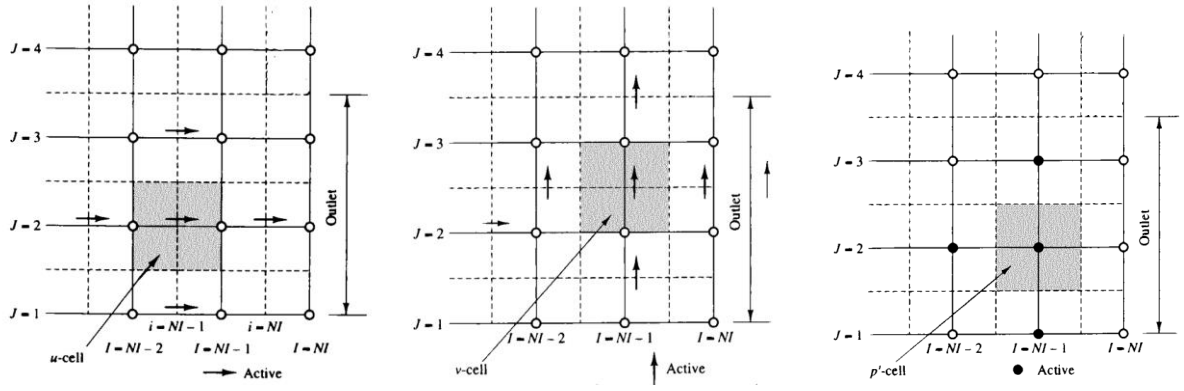

Figure 5-8: Outlet boundary condition for the fluid solver [149]

Similarly, Figure 5.8 shows the outlet boundary condition. To make sure that the continuity equation is satisfied, the flow rate difference is calculated between the inlet and the outlet boundaries. These two flow rates are compared and the outlet velocity, u_{out} , is updated according to the flow rate difference. The following equations are used for the outlet boundary conditions,

$$\begin{aligned} u_{f(Ni,J)} &= u_{f(Ni-1,J)} + u_{\text{correct}} \,, \\ v_{f(Ni-1,j')} &= v_{out} \,, \\ P_{Ni,J} &= P_{Ni-1,J} \,, \end{aligned} \tag{5-28}$$

where, outlet velocity in *y*-direction, v_{out}, is set to zero and a velocity correction in *x*-direction is calculated using

$$u_{\text{correct}} = \frac{\text{flow}_{in} - \text{flow}_{out}}{\text{Outlet Area}}, \tag{5-29}$$

where, flow_{in} is the inlet flow rate and flow_{out} is the outlet flow rate which are calculated from the velocity profile. It is important to note that the no-slip condition has been taken into consideration in this correction and all these calculations are done for $J = 2$ to $J = N_J - 1$.

5.4 Computational Structure

The computational structure of the numerical model is shown in Figure 5.9. This algorithm is implemented in a FORTRAN code. In this section, the order in which the previous equations are implemented in the code is discussed.

The numerical model starts by setting up the problem and by loading the mesh file. The mesh file describes a two-dimensional structured grid. Next, initial values are loaded into the computational cells. An important initial value that should be set by the user is the initial particles density in each class. The code uses this value to calculate and apply the artificial pressure, discussed in the Equation (3-36). Next, the particles boundary conditions are set according to Section 5.3.6. Equations (3-7) to (3-10) are solved next. According to the aggregation and disaggregation models (discussed in the next chapter), particles move between classes. The population-balance model is solved to find the new balance between particles. This will result in updated particle densities, ρ_{κ}^{n+1}, for each class in the domain. Using these updated densities, the volume fraction can be calculated using Equation (3-21).

In the next part of the code, the inner loop for the fluid solver starts iterating. In the first iteration, it uses the information coming from previous time step to find the source terms that are presented in Section 5.3.4. After the first inner iteration, all the source terms are calculated using the *m+1* state and according to Equations (5-18) to (5-22). Next, the particle solver is used to find the particles velocity in each class. In this loop, when the fluid solver updates its velocity field in each iteration, the particle solver should adapt and update its velocity field. After this step in the loop, the fluid solver starts to work. The details on this solver are presented in Appendix B.

The convergence criteria for the fluid solver to stop the inner loop use the maximum residual of pressure field and velocity fields. If this number is reduced by at least two orders of magnitude, the code stops the inner loop and goes to the next time step. In the next section, verification of this code is presented and some of the benchmarks in multiphase fluid flow modelling are simulated using this code.

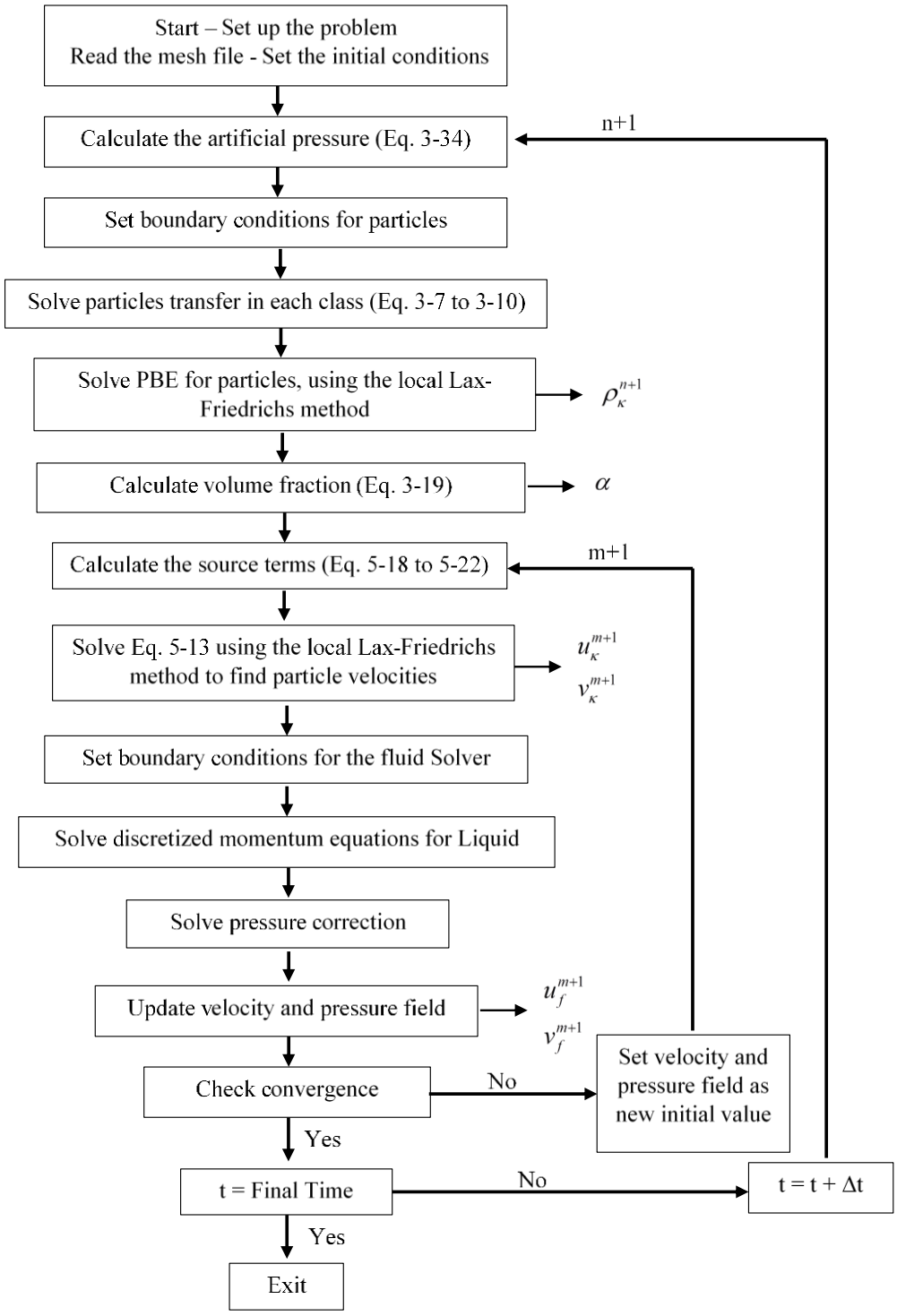

Figure 5.9: Computational structure of the numerical model

5.5 Verification

In this section, several numerical cases are modelled using the current code. These models are not directly related to blood flow simulation. Rather, they are benchmark problems in two phase flow simulation. These cases are used to verify that each individual section of the code is implemented as intended. Also, the grid convergence and the order of accuracy are verified in this section.

5.5.1 Fluid Solver

The solver for the background flow is checked by simulating the classical lid-driven cavity flow and Couette flow. Figure 5.10 shows the cavity flow for two different Reynolds numbers. The Reynolds number in this case is calculated by the velocity and the length of the top wall. To verify the numerical solution, a vertical line and a horizontal line in the centre are chosen and *u* and *v* velocity are compared with the solution of Ghia *et al*. [151] on these lines. In these test cases, a one meter by one meter cavity filled with air is used.

Figure 5.11 shows a satisfactory agreement between the developed code and the Ghia *et al.* [151] results. To find the order of accuracy of the developed code, Table 5-1 is presented for Re=1000 for the *u* velocity error. The error in Table 5-1 is calculated from Figure 5.11 by comparing Ghia *et al.* data with the numerical results of the developed code. The equation used to calculate the error is

$$\text{Error} = \frac{\left|U_{\text{model}} - U_{ref}\right|}{\left|U_{ref}\right|}. \tag{5-30}$$

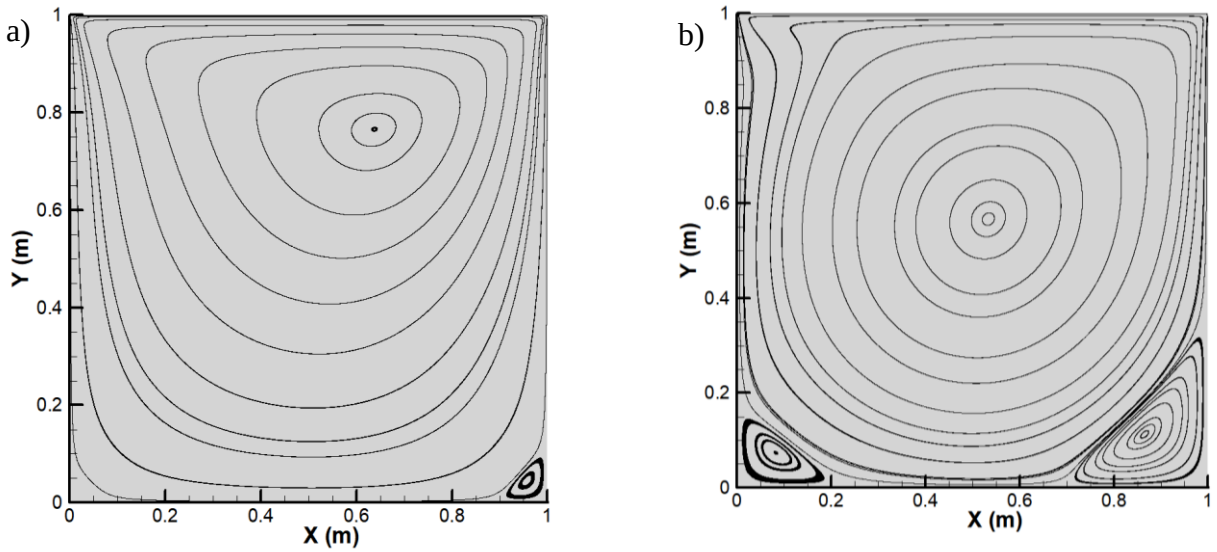

Figure 5.10: Streamline for lid driven cavity flow simulation in (a) Re=100 and (b) Re =1000.

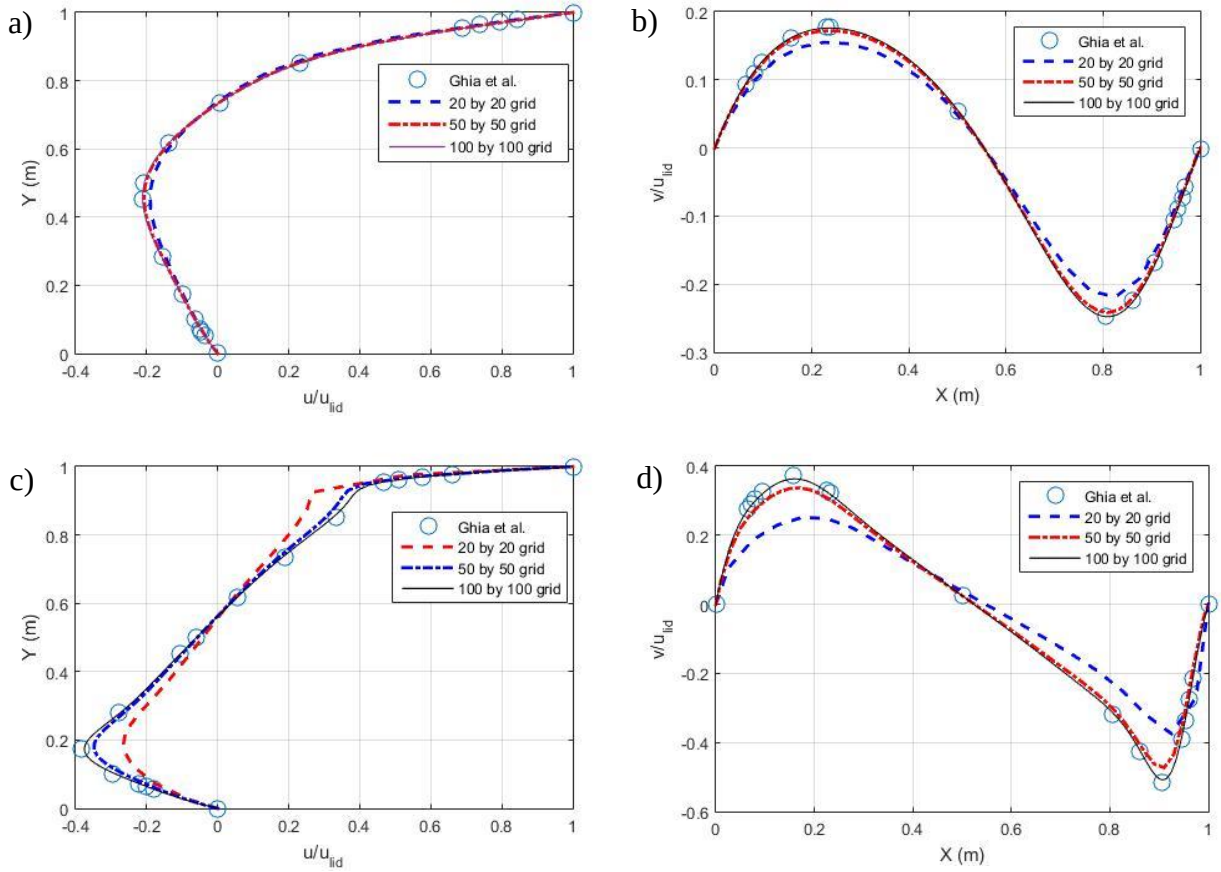

Figure 5.11: Comparison of u and v velocities for two Reynolds numbers (a) Re=100, u velocity, (b) Re=100, v velocity, (c) Re =1000, u velocity and (d) Re =1000, v velocity.

As can be seen in Table 5-1, by reducing the size of the cells of the grid the error decreases. By calculating the order of accuracy using these grid sizes and observed errors, it can be seen that the order of accuracy approaches 2 for this code.

Table 5-1: Error and order of accuracy for Re=1000 and *u* velocity

Δx & Δy	Error	Order of accuracy
0.05	0.3190	-
0.02	0.0769	1.5527
0.01	0.0227	1.7603
0.005	0.0063	1.8493
0.0025	0.0017	1.8961

Similarly for Couette flow and channel flow, the code results are shown in Figures 5.12 and 5.13 for Re=100. In the case of Couette flow, the Reynolds number is calculated using top wall velocity and the height of the channel. For the channel flow, the Reynolds number is calculated using the inlet velocity and the height of the channel. In these case studies water properties are used. A 200 by 200 grid is used for both cases and the exact geometry used for these cases can be seen in Figures 5.12 and 5.13.

As can be seen in Figure 5.12, the Couette flow velocity field shows a linear increase to the velocity. It starts as zero close to the south boundary and increases linearly until it gets to the top wall velocity. For channel flow illustrated in Figure 5.13, a uniform velocity is given as an inlet boundary condition. It can be seen that the no slip boundary conditions takes effect and makes the velocity field approach a parabola. The pressure drop is also visible in this graph. As the flow advance thorough the channel, the pressure decreases due to the viscosity and the no-slip boundary condition.

To compare these results more accurately, the analytical solution for fully developed flow in a similar channel to Figure 5.13 is compared with numerical results. For numerical results, velocities at $x = 0.8$ are plotted for several grid sizes in Figure 5.14 and are compared to the analytical solution of the channel flow. It can be seen that by increasing the number of cells in the simulation, the accuracy of the results increases as well.

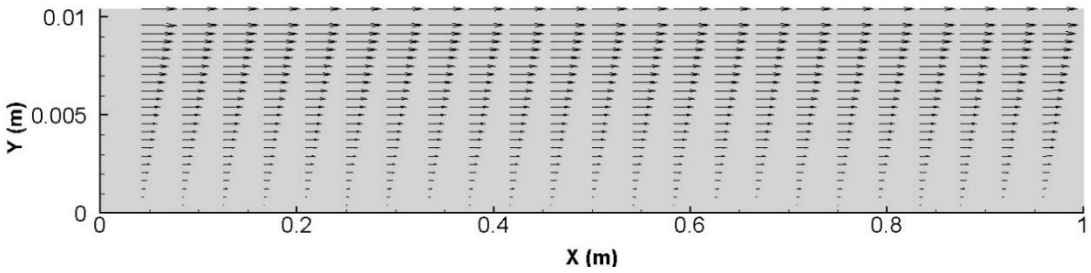

Figure 5.12: Velocity vectors of Couette flow simulation for Re =100.

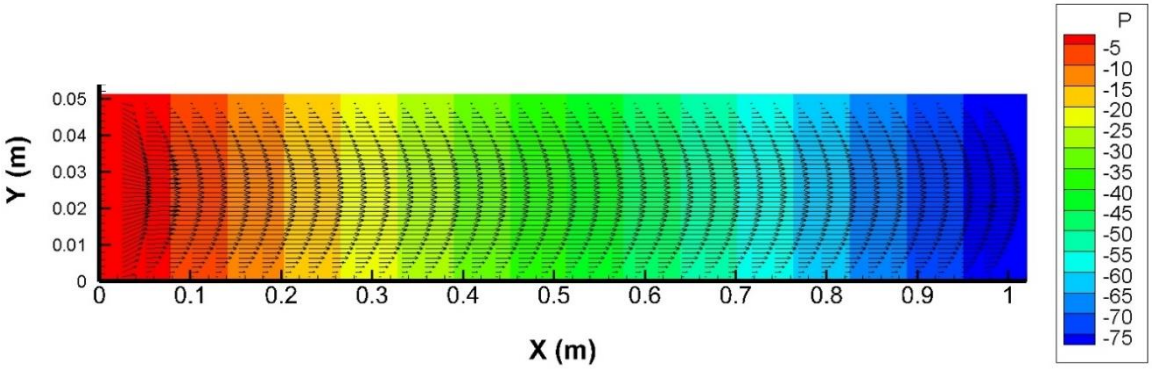

Figure 5.13: Pressure contour and velocity vectors for the channel flow simulation at Re =100.

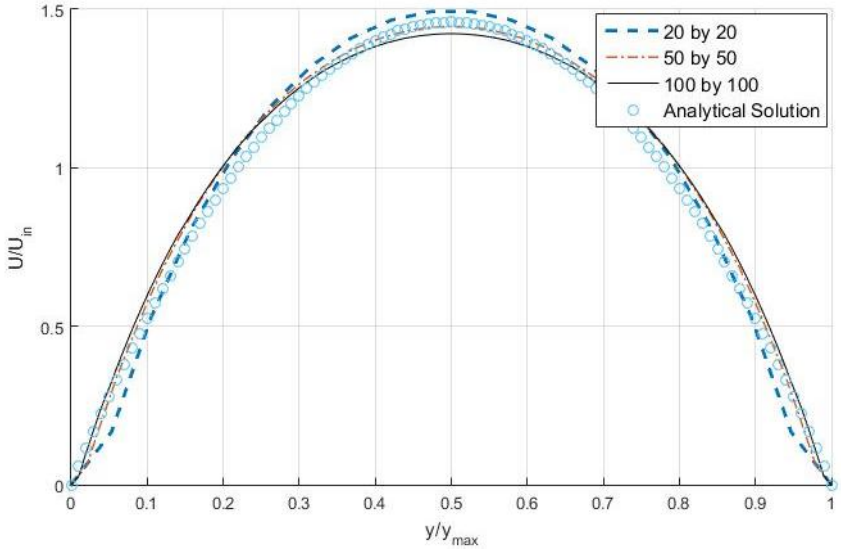

Figure 5.14: Analytical solution versus numerical for the Re=100 channel flow.

5.5.2 Particle Solver

To verify the particle solver, several tests were conducted. For these tests, the background fluid solver is disabled and the background fluid velocity is held constant at zero. In the first test, a pack of spherical particles from only one class with a volume fraction of 0.3 is placed in the centre of the domain. The domain is confined with four solid-wall boundary conditions and the dimensions of the domain is 10 cm by 10 cm. The grid size in this test is 200 by 200 cells. Particles are placed within a 2 cm by 2 cm square in the centre as the initial condition. This test is a transient simulation of particles falling due to acting forces. All the forces are activated one by one and the time for the particles to reach a certain point is measured (Figure 5.15). This measured time is compared to analytical solutions in Table 5-2.

Using Newton's second law of motion, one can predict the location of the particles at any time. For example, for spherical particles in low Reynolds number flow, the drag force and the gravitational force are defined in Equation (3-27) and Equation (3-26), respectively. By combining these three equations, and knowing that $v = {dy(t)}/{dt}$, a second-order differential equation can be derived and solved for the location of particles, $y(t)$, at any time. This differential equation can be written as

$$\frac{d^2 y(t)}{dt^2} = \frac{(\rho_\kappa - \rho_f) g}{\rho_\kappa} - \frac{3\pi\mu d_\kappa}{\rho_\kappa}\left(\frac{d\, y(t)}{dt} - u_f\right) n_\kappa, \tag{5-31}$$

where the initial conditions for solving this equation are $y(0) = 0$ and ${dy(0)}/{dt} = 0$ and the fluid velocity, u_f, is assumed to be zero.

Table 5-2 shows the time calculated for particles to reach a certain location in the domain using numerical model and analytical solution when different forces are active. These comparisons verify that the forces acting on the particles are working properly. In this table properties of particles and background fluid are similar to red blood cells and plasma (same density viscosity, particle radius and etc.). For the drag coefficient, it is assumed that the particles are spherical.

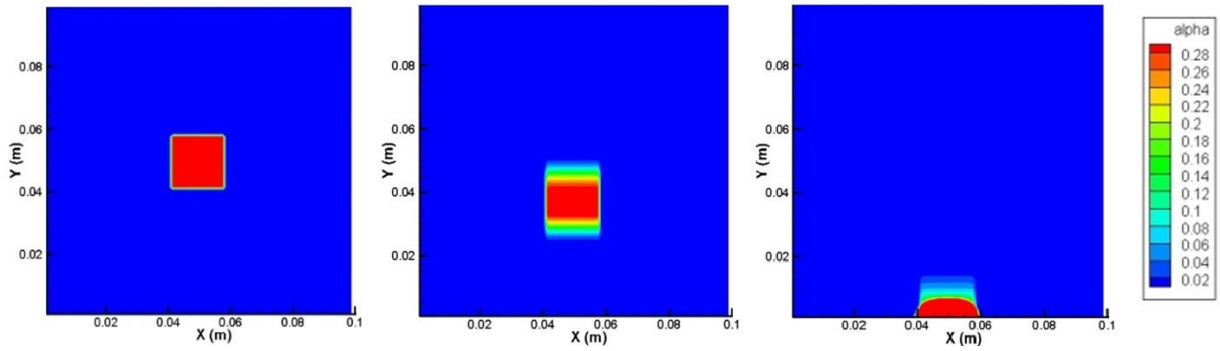

Figure 5.15: Pack of spherical particles moving just due to gravity, from left to right t=0, t=0.05 and t=0.1.

To find the numbers presented in Table 5-2, a condition is implemented in the code which stops the code when the maximum concentration of particles passes the targeted location. The small difference between numerical results and analytical results in Table 5-2 is smaller than the time step in the numerical code. For example the time step for the first case is 0.0004 s, which is bigger than the smallest decimal in the analytical calculation. When gravity, buoyancy and drag are all active, the results for single red blood cell sedimentation can be compared to the erythrocyte sedimentation rate (ESR) test. In the ESR test, the normal range for red blood cells to sediment in a Westergren tube for newborns is between 0 to 3 mm and the simulation in 3600 seconds results in 2.6 mm of sedimentation for single red blood cells.

Table 5-2: Time required for particles to move to a location due to various forces

Active forces in the model	Numerical model time to move 1 cm	Analytical time to move 1 cm
Just Gravity	0.0453 s	0.0452 s
Gravity and Buoyancy	0.1518 s	0.1514 s

Active forces in the model	Numerical model time to move 0.1 mm	Analytical time to move 0.1 mm
Gravity and Drag	15.8097 s	15.81 s
Gravity, Buoyancy and Drag	140.470 s	140.13 s

The next test is intended to verify that the particles properly displace the correct volume of the background fluid. In this case, a 1mm by 1mm domain with a 200 by 200 grid is used. Similarly to the previous case, particles with a volume fraction of 0.1 are placed in 0.1 mm by 0.1 mm square in the center. Only the gravity force is activated in this simulation. The contours

of divergence of momentum density for both solvers are shown in Figure 5.16 in addition to the velocity vectors. The sum of these two contours result in zero total change of density for both solvers. This is a direct result of the implementation of volume fraction in the model (Equation (3-21)). The velocity distribution without activating the drag force also shows reasonable result, where downward movement of particles results in upward moving of the fluid.

Tuning the pressure term is the next step for verifying the particle solver. Figure 5.17 shows the effect of the artificial pressure in the model. In this case, a 1cm by 1cm domain with a 200 by 200 grid is used and particles with a volume fraction of 0.1 are placed in 2 mm by 2 mm square in the center. Only the gravity force is activated in this simulation; all the boundary conditions are solid walls. As can be seen particles have settled down and reached the bottom of the domain in this simulation. Without the pressure term, particles could gather all in the bottom row of computational cells (Figure 5.17 (a)). The artificial pressure is there to stop this modelling error by applying a high pressure when the particles density approaches the maximum packing fraction (Figure 5.17 (b)) using Equation (3-36). As can be seen, using the artificial pressure results in a more realistic model and can mimic the physics of the sedimentation layer.

To compare the effect of the artificial pressure with experiment, a test is designed where particles are initially evenly distributed over the whole domain with 40% volume-fraction. The gravity force is activated and particles all settle down. The same domain, grid and boundary conditions as before are used. As can be seen in Figure 5.18, using the artificial pressure can simulate the sedimentation layer line which is also distinguishable in the experiment. This layer growth will be used for further validation in Chapter 6. It should be noted that the Figure 5.18 (b) does not have the same scale as the simulation and cannot be compared in this figure quantitatively. But qualitatively, it can be seen in Figure 5.18 (b) that in the experiment when the sedimentation layer is formed, lower layers have more concentration of particles and upper layers have less volume fraction. The artificial pressure has the ability to mimic this in the model as can be seen in Figure 5.18 (a).

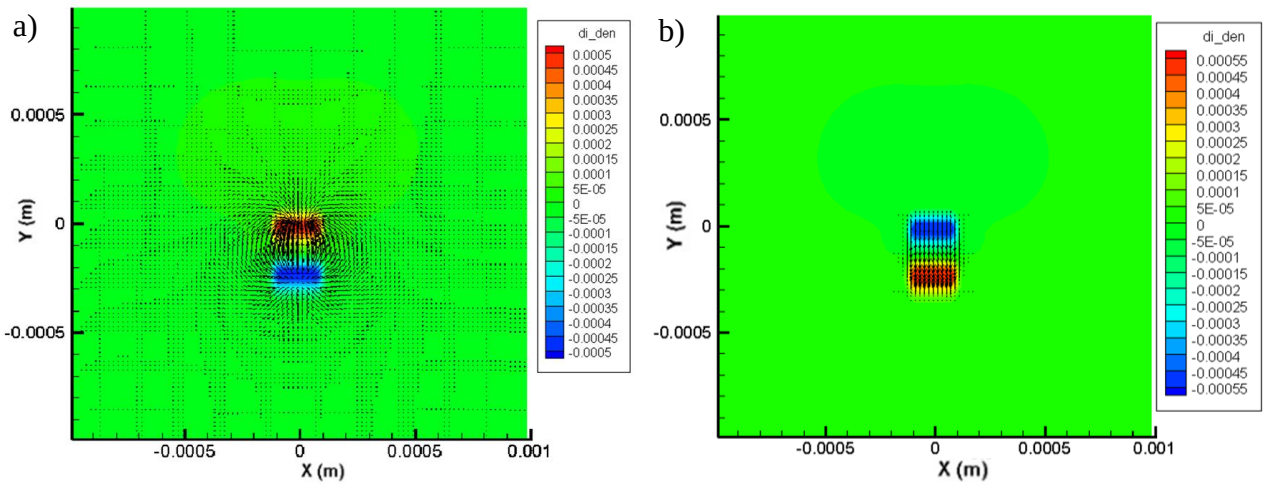

Figure 5.16: The change of density with time when particles are falling due to gravity for: (a) the background fluid solver and (b) particle solver.

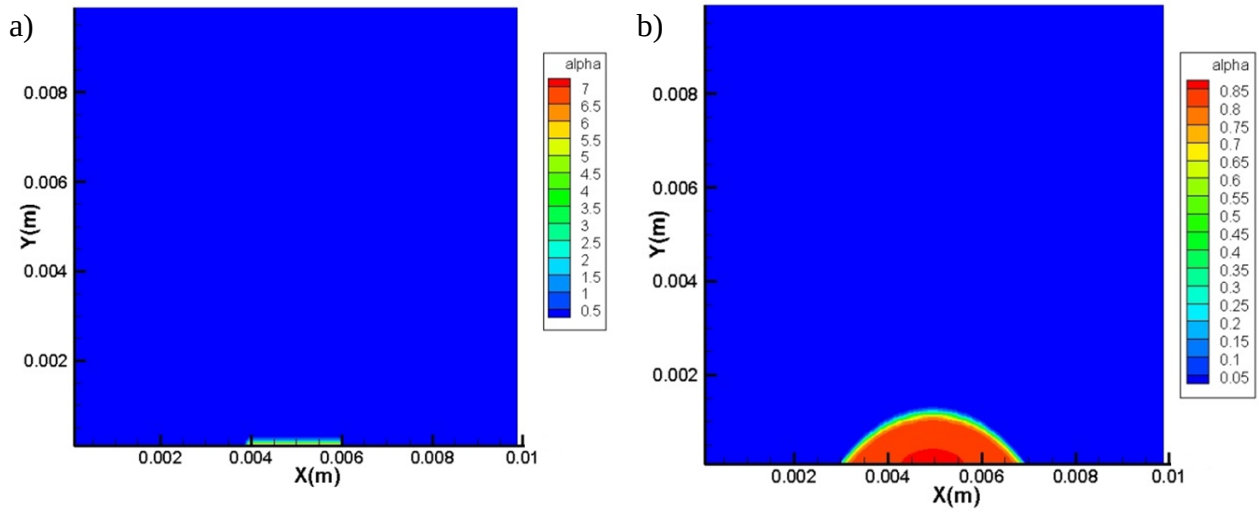

Figure 5.17: Particles settling, (a) without an artificial pressure and (b) with an artificial pressure.

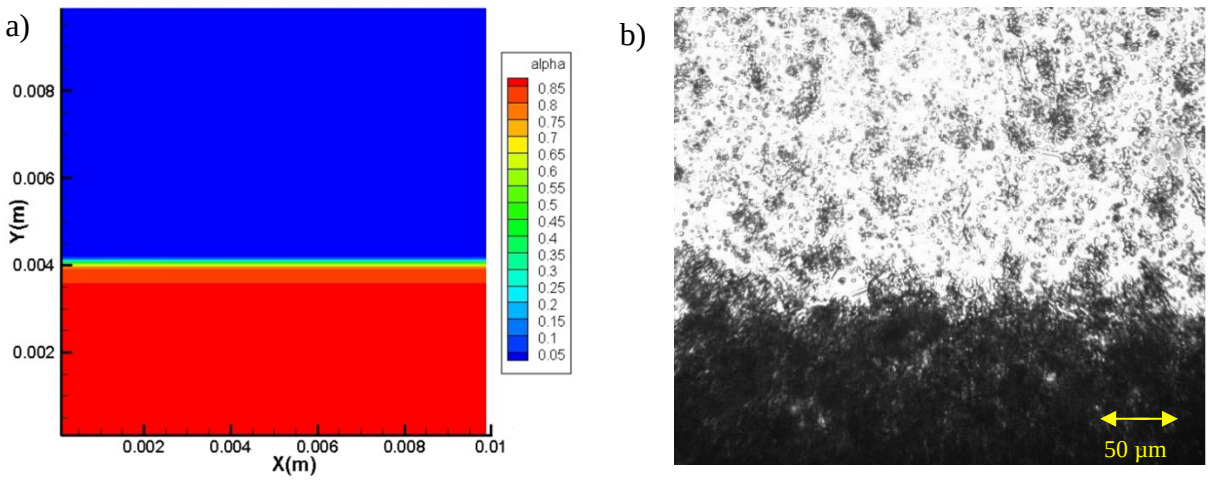

Figure 5.18: Comparison of (a) sedimentation layer formation in the numerical model and (b) sedimentation layer formed in experiment, magnified and after 100 seconds from the start of experiment.

The next step is to verify the interaction of several particle classes. Figure 5.19 shows the first three particle classes at a same time in a simulation (*t=2* s). This simulation starts with all particles at the center. Gravity, buoyancy and drag force are activated and aggregation is turned off. A 1cm by 1cm domain with 200 by 200 grid is used for this simulation. All the boundary conditions are set to be a solid wall. The density of each of these particle families, at the beginning of the simulation is set to be 100 kg/m^3 and they are placed in a 2 mm by 2 mm square at the centre of the domain. As can be seen in Figure 5.19, the location of these three particle families depends on the size of the particles in these families and larger particles settle faster while smaller particles move more slowly. In this case, particles start in a square at the centre. As can be seen in Figure 5.19, after 2 seconds in the simulation, the square shape is changed to a circle shape. The reason for this numerical error is the presence of a discontinuity in the initial condition. Having a cell with high concentration of particles near a cell with no particles results in numerical diffusion. The first-order accuracy in time for the numerical method is not able to handle this discontinuity properly. Comparing Figure 5.15 and Figure 5.19 the effect of first-order accuracy can be seen. Figure 5.15 has less time steps in its calculation and the square shape is preserved, where Figure 5.19 has more time steps and the square shape is changed to the circular shape.

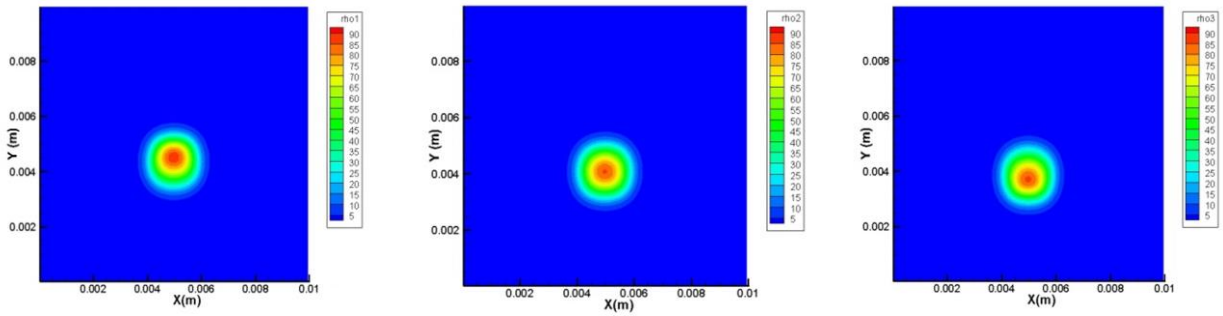

Figure 5.19: Three particle class settling at t=2s, from left to right: $v_1 = 90\mu m^3, v_2 = 180\mu m^3$ *and* $v_3 = 360\mu m^3$.

Now that the particle-solver code is verified, the order of accuracy of the solver in space and grid convergence of the code should be checked. To do so, a case where the particles enter from a small inlet on the left boundary and move due to initial momentum and fluid forces is presented. As explained, having a discontinuity in the domain would result in larger numerical errors. Therefore, for the inlet, a Gaussian distribution for density is assigned so a continuous distribution of particles in the domain can be satisfied. The inlet density distribution is given by

$$\begin{aligned} \rho_{in} &= \frac{83.3}{\sqrt{2\pi\sigma^2}} e^{-\frac{(y-7)^2}{2\sigma^2}} \qquad \text{for} \quad 6.5\,\text{mm} \le y \le 7.5\,\text{mm}, \\ \rho_{in} &= 0 \qquad\qquad\qquad\quad \text{for} \quad y \le 6.5\,\text{mm or } 7.5\,\text{mm} \le y \end{aligned} \tag{5-32}$$

where, *y* is the location in millimeters. The inlet width is 1 mm and the center of it is located at *y* = 7 mm, as can be seen in the Figure 5.20. Here, σ is equal to 0.1667 mm and is the standard deviation of the Gaussian distribution. The rest of the boundaries are assigned as an outlet for particles. The background fluid solver is deactivated and the particle solver uses a fixed initial background velocity to calculate the drag force. Figure 5.20 shows the simulated results with a 200 by 200 grid and the inlet velocity of 0.5 m/s. The domain is 1 cm by 1 cm. Particle diameters are 7 µm for first two cases, but for the other cases a particle diameter of 1000 µm is used. This change is done due to very high drag force on smaller particles. In the first three case studies initial background velocities are set to be zero and in the last case study in Figure 5.20 the initial background velocity is fixed to 0.1 m/s in the *y* direction.

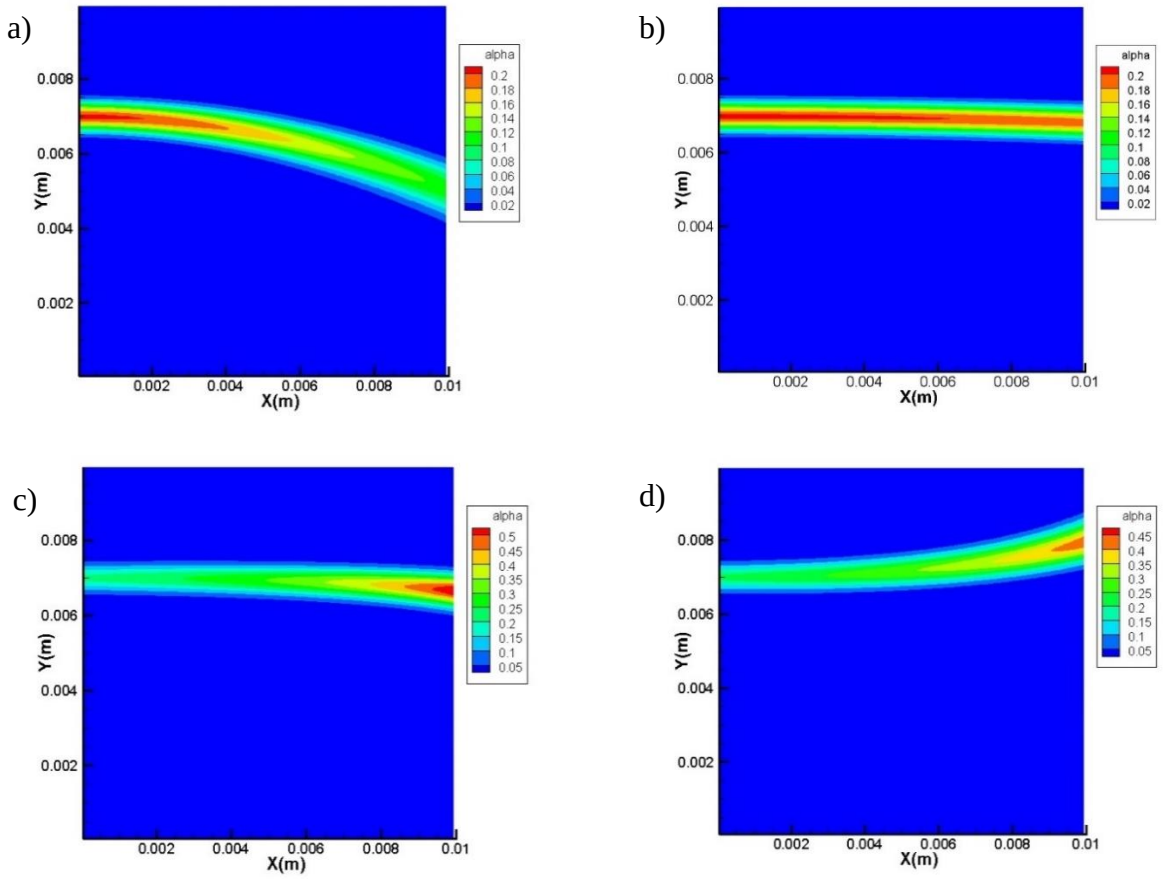

Figure 5.20: Particle entering the domain from a small inlet in the left boundary. Active forces are: a) just gravity b) Gravity and Buoyancy c) Gravity, Buoyancy and Drag d) Gravity, Buoyancy and Drag with a constant upward background flow.

Similarly, analytical solutions for these flows can be developed using Newton's second law of motion in both directions. Equation (5-31) governs the exact solution for the location and the velocity of particles as a function of time in the *y*-direction. A similar equation can be used for the *x*-direction. The initial conditions for particles in the *x*-direction are the same as the inlet condition in the model. From the exact solution of the *y* position, the velocity in each location can be found by taking a time derivative. Using the continuity equation, the density at each location can be found. The last process to have a comparable result to the numerical model is to map these data to the same grid and domain. To calculate the error, the L2 norm of density is used. The equation for calculating error is

$$\text{Error} = \sqrt{\sum \left(\rho_{Numerical(i,j)} - \rho_{Analytical(i,j)} \right)^2 A_{i,j}} \ . \tag{5-33}$$

To find out the order of accuracy of the developed code, the following table is presented for the simulation with all forces active and constant background flow (Figure 5.20-d).

Table 5-3: Error and order of accuracy for case d in Figure 5.20

Δx	L2 norm Error	Order of accuracy
0.05	0.6768	-
0.02	0.1447	1.6840
0.01	0.0441	1.7132
0.005	0.0127	1.7977
0.0025	0.0035	1.8654

To check the grid convergence, the density at the outlet for the last case in Figure 5.20 is plotted in Figure 5.21 and compared with the analytical solution. As can be seen, increasing the number of cells in the domain improves the accuracy of the model and in the coarser meshes the numerical diffusion is higher.

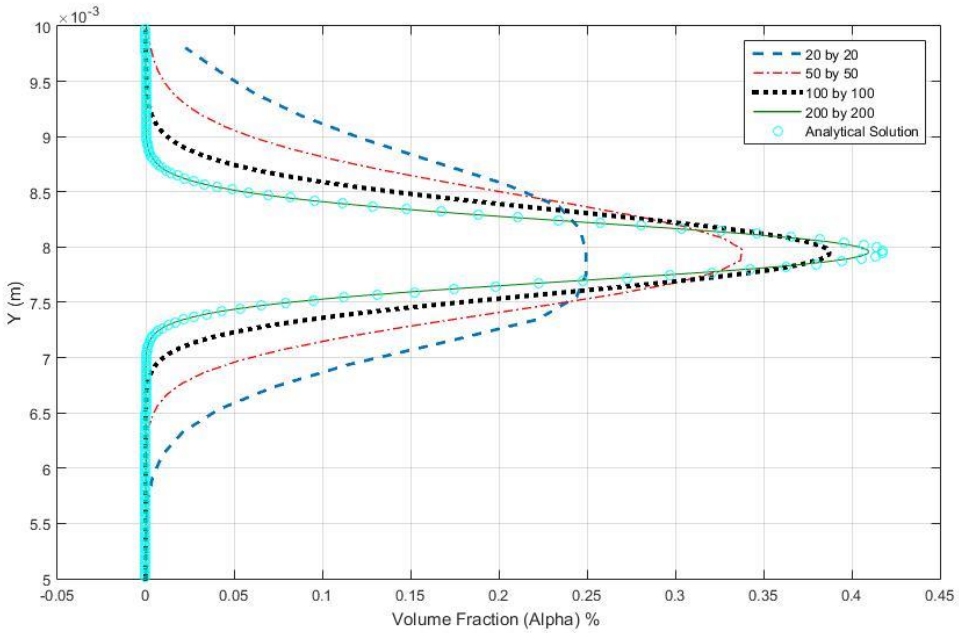

Figure 5.21: Grid convergence of the particle solver

5.5.3 Coupled Model

The fluid solver and particle solver are individually verified thoroughly in the previous sections. When these two codes are coupled together, it is harder to verify the implementation. There is no analytical solution for this model and when considering aggregation, this model becomes very complicated. In this section it can just be shown that this model is consistent with our expectations. Figure 5.22 shows a set of 3 classes of particles settling with a dynamic fluid flow around it. All the forces are active, aggregation of particles is also active and the CFL number of 0.2 is used. The reason behind lowering the CFL number in these simulations is the drag force. Although the semi-implicit treatment of the drag force makes the numerical model less stiff, still some instabilities may occur when using higher CFL numbers. The domain is 1 mm by 1 mm and a grid of 200 by 200 is used. Particles are placed in a 0.2 mm by 0.2 mm square in the centre and their initial density is set to 100 kg/m^3. Figure 5.22 shows the simulation after 100 seconds. The ellipsoidal shape that the particles make is due to the higher settling velocity of particles in bigger classes. Background velocity streamlines are also shown in this figure. The particle movement causes the background velocity field to have a rotational movement.

Similarly, in Figure 5.23, a case where the domain is filled with particles is simulated. Again, all the forces are active, aggregation of particles is also active and the CFL number of 0.2 is used in a grid of 200 by 200. In this situation, the initial condition is set to have only particles in the first class with the volume fraction of 0.45. These particles have diameter of 7 μm. Due to the aggregation function, particles in other classes are formed. These newly formed particles settle faster compared to particles in smaller classes. There is a limit of eight classes and, therefore, particles can aggregate and get larger up to 2^8 of the size of the first particle class. Particles move to the bottom of the domain and the background fluid has to replace them. This is shown in Figure 5.23 by showing the vector field. This figure shows the simulation after 100 seconds.

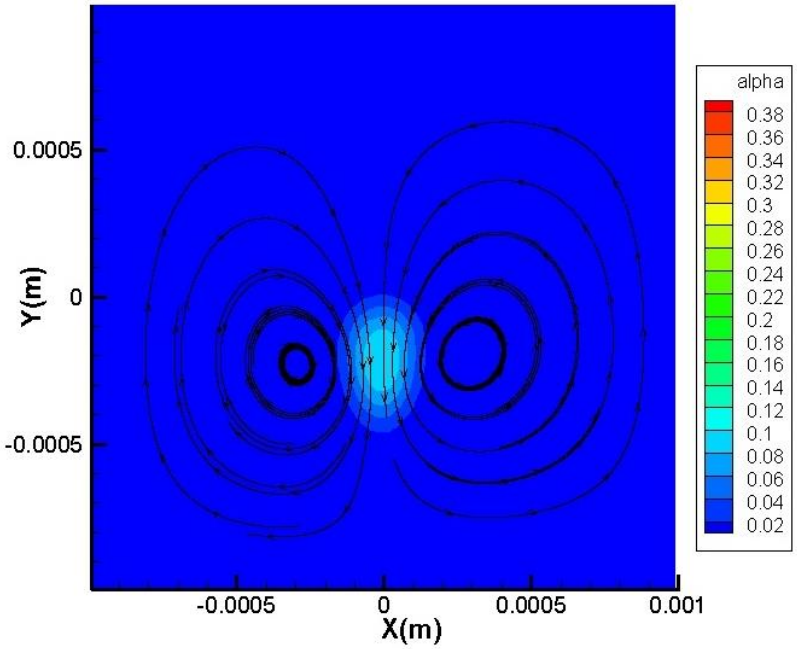

Figure 5.22: The effect of particle settling on the fluid flow

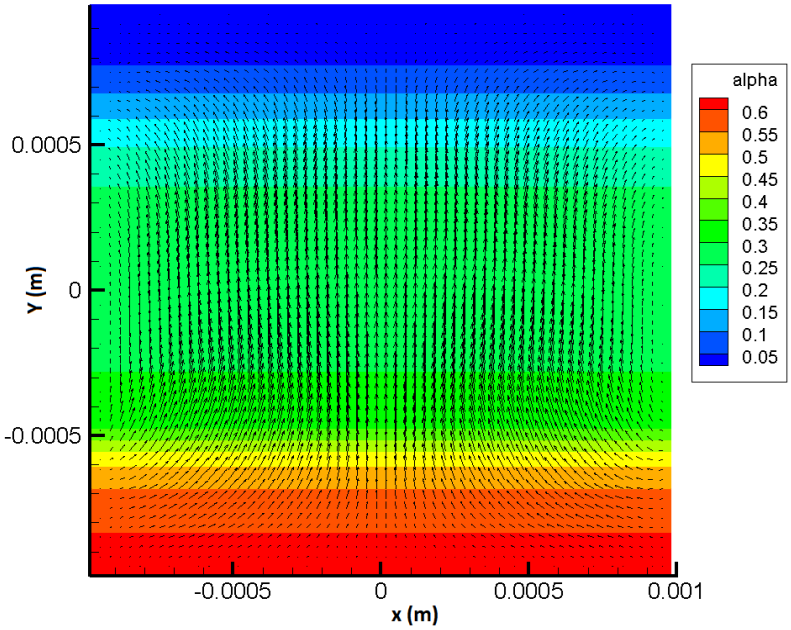

Figure 5.23: The effect of particle settling on the fluid flow (the whole domain is initially filled with particles)

5.6 Summary

The numerical model consists of three important parts: the population-balance equation, the momentum equation for particles and the incompressible Navier-Stokes equations for the Newtonian background fluid. In Chapter 3 all these parts are described in detail. These three parts are not independent and they should be solved as a closed system. The procedure of solving all the equations simultaneously is given in this chapter in detail. The local Lax-Friedrichs method in addition to the minmod slope limiter is used for the discretization in the particle solver. This method results in first-order accurate model in time and second-order accurate model in space. The SIMPLEC method is used to discretize the domain for the background fluid solver which also results in a first-order accurate model in time and second-order accuracy in space. Details on boundary conditions, source terms and details on the numerical code are presented. Verification of the numerical code is also demonstrated.

Chapter 6

Experimental Results and Validation of the Model

6.1 Introduction

In this chapter, the experimental results are presented first. These experimental data are all extracted using the Matlab code presented in Chapter 4. From these experiments, aggregate projected area, perimeter, location and velocity of particles are extracted. Using these data, the missing parameters, like aggregation and disaggregation rates, are found. These parameters are necessary to complete the model. Lastly in this chapter, the implementation of the missing parameters in the model and validation using the experimental data are discussed.

One of the experimental results determined from the raw data provided by the Matlab code is macroscopic aggregation and breakage rates, where Equation (3-6) is the subject of the study in Section 6.3. Macroscopic aggregation and disaggregation rates are useful for macroscopic models similar to Owens' model [11]. These parameters are not used in the present numerical model, but they are used to compare the microscopic and the macroscopic variants of the population-balance model.

As discussed in Section 3.2, defining the aggregate classes is an important factor when the population-balance model is used. In the numerical code when a particle between two classes (*i.e.* v_κ and $v_{\kappa+1}$) is generated, due to either aggregation or disaggregation, that particle is distributed to those classes according to Equations (3-7) to (3-10). Increasing the number of classes should increase the accuracy of this model and the details, but at the same time, for each class of particles, an additional set of 3 equations should be solved in a 2D numerical model.

In contrast, in the experimental results, increasing the number of classes can reduce the accuracy of the measurements. This dependency is a direct outcome of errors coming from the analysis of experimental images. When the particles have very close pixel sizes, it is possible to classify the particle in a wrong class. Therefore in the experimental procedure, classes with easily discernible sizes are preferred. In this work, eight classes of particles are used and the classification of particles for the numerical simulation is the same as the one presented in the experiment. Table 4-1 shows the particle classes in the sedimentation simulation and Appendix A shows the same for Couette and channel flow. In these tables the relation for the volume between two consecutive class is $v_{\kappa+1} = 2v_\kappa$.

The microscopic aggregation rates, Equations (3-9) and (3-10), are harder to find, as these terms depend on sticking probability and collision rates between particles. Also, as shown in the Equation (3-11), for eight class of particles there is 28 aggregation rates that should be estimated for this model. To estimate aggregation rates between each class, Equation (3-12) is used. The collision rate for each experiment is different and is found using the velocity distribution of the RBCs using the Matlab GUI and Equation (3-15). Using the collision rates found from the sedimentation experiments, the sticking probabilities are estimated. These probabilities are used in the rest of the simulations. Section 6.4 explains the method used to find these parameter in detail.

Next, the microscopic disaggregation rates are found using the microscopic aggregation rates and the Couette-flow experimental results. As discussed in Chapter 3, Couette flow is not a transient flow and fields describing the particles are assumed to have reached an equilibrium. As discussed in Section 3.6, by assuming that the particles only break into two daughter particles with the same volume, this model equations (Equation (3-7) and (3-8)) simplifies to Equation (3-17). For eight classes of particles, this equation has only seven unknown functions, which relates the disaggregation frequency of particles to the shear rate in a domain. Further details are provided in Section 6.5.

After determining aggregation and breakage rates, these rates are applied in the model and the numerical code is complete. The only parameter that remains is the shape of elliptical particles in each class which is used to calculate the intrinsic viscosity and the drag force on particles. Section 6.6 is devoted to finding these parameters using image processing outputs discussed in Section 4.5.4. Lastly, the validation of the numerical code in several case studies is presented in Section 6.7 and the whole blood viscosity is estimated using the numerical model in Section 6.8.

6.2 Experimental Data Extraction

Figures 6.1 to 6.3 show samples of the image processing applied to each experiment, using the information presented in Table 4-2. From these figures, the projected area, perimeter, location and velocity of the particles are extracted. As explained in the image processing procedure, the raw image is filtered first and analyzed to find particle size and velocity distribution. All the experiments are performed multiple times on at least 5 different samples. Five alphanumeric characters are used to name the sample and to anonymize the donner.

Figure 6.1 shows an experimental image taken at t = 80 s at the bottom of the channel in the sedimentation experiment. In this experiments a hematocrit of 5% is used. This experiment is transient and it is used to find the relation of particle size with time. A 10X lens is used in this experiment in order to have a wider view and therefore more particles to detect. It can be seen that a sedimentation layer is formed at the bottom of the channel and all range of particles class are present in this picture and are shown by a colour code system. Figure 6.1 (a) shows the original picture taken in the experiment. This picture is cropped to remove additional information. Figure 6.1 (b) shows the same image after applying filters. Particles are easier to differentiate in this image compared to the original image. After classifying the detected particles, particles are colour coded according to their class and are shown in Figure 6.1 (c).

Figure 6.2 shows an experimental image taken by Mehri [13] in the set-up discussed in Section 4.4. In this set-up particles are easier to detect as a 20X lens is used. This lens reduces the area and therefore reduces the number of detected particles but it increases the accuracy of particle detection and classification. In this experiment a hematocrit of 5% and shear rate of 24.48 s^{-1} are used. Figure 6.2 (a) shows a section of channel where red blood cells are moving. Depending on the experiment the width of this section changes from 40 to 50 µm.

Similarly, Figure 6.3 shows an experimental image taken by Gliah [134] in the channel flow experiment. In this experiment a hematocrit of 10%, a flow rate of 12 µl/hr and a 40X lens are used. This lens results in more pixels for each particle compared to a 20X lens and easier detection of particles. The original image, filtered image and overlay image are shown in Figure 6.3 (a) to (c).

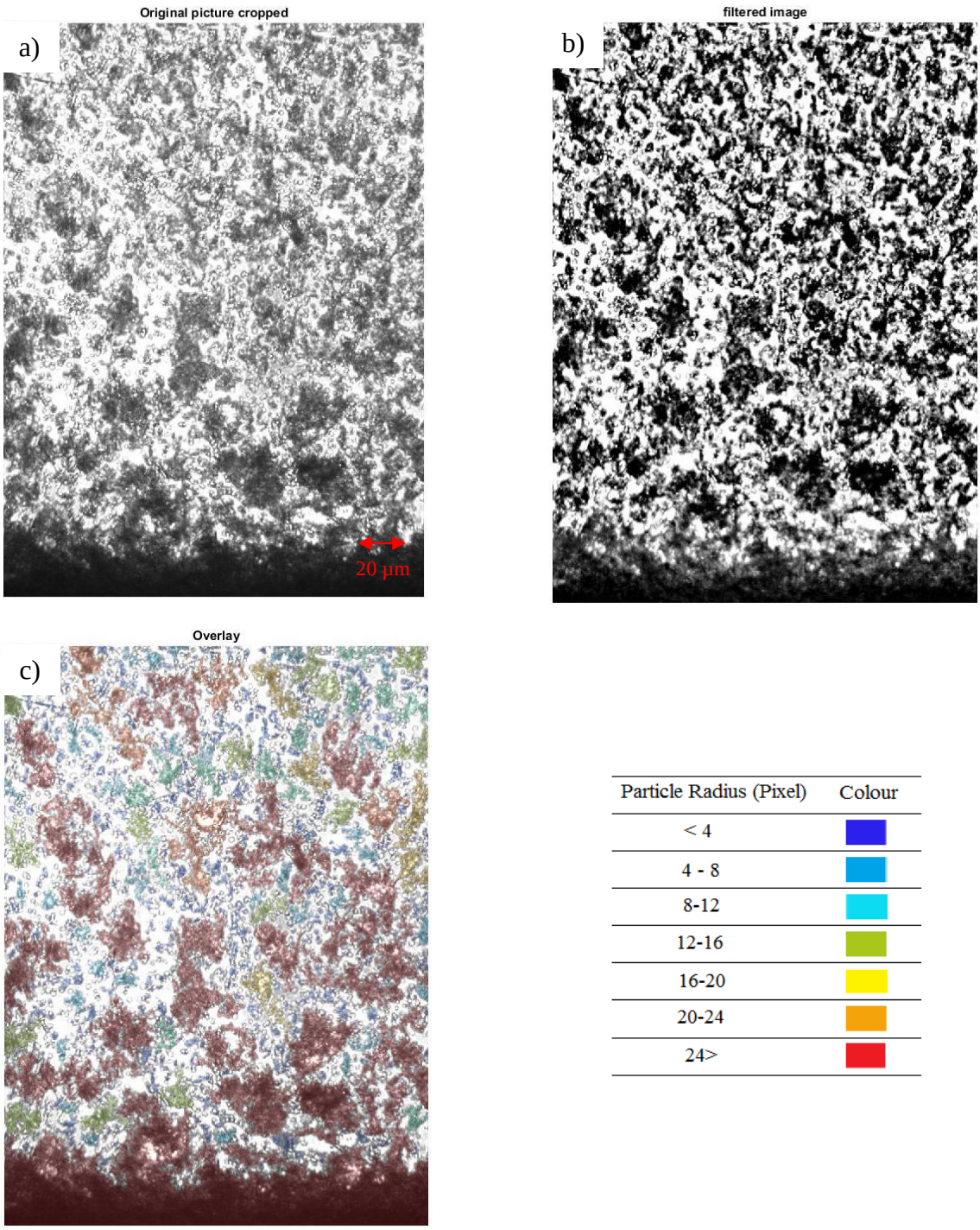

Figure 6.1: Image processing technique applied on the sedimentation set-up at t=80s and Ht=5%. a) Original image, cropped, b) Image after filtering, c) Overlay image

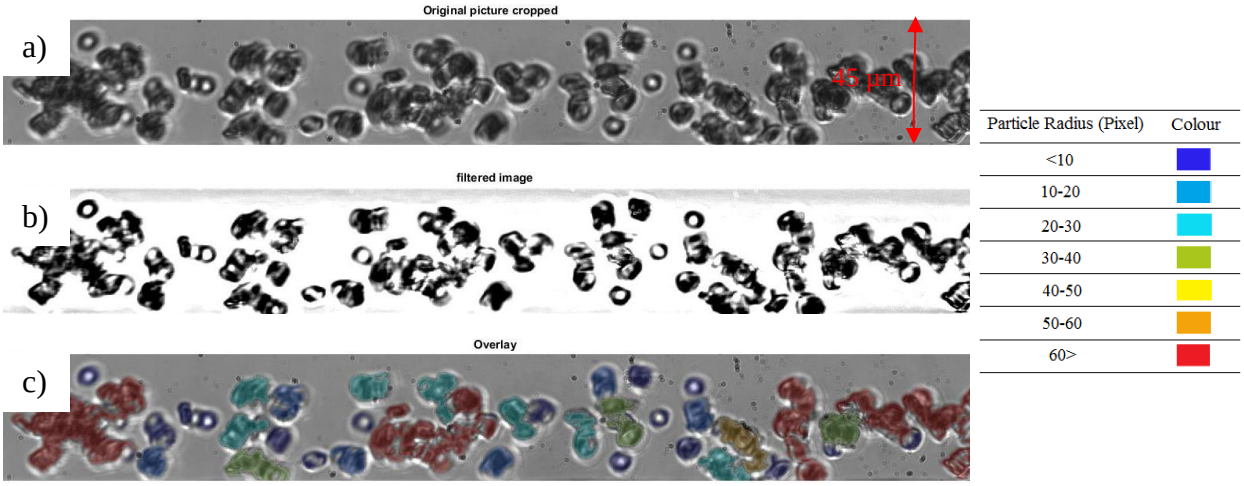

Figure 6.2: Image processing technique applied on the Couette flow set-up at Ht of 5% and shear rate of 24.89 s^{-1}. a) Original image, cropped, b) Image after filtering, c) Overlay image

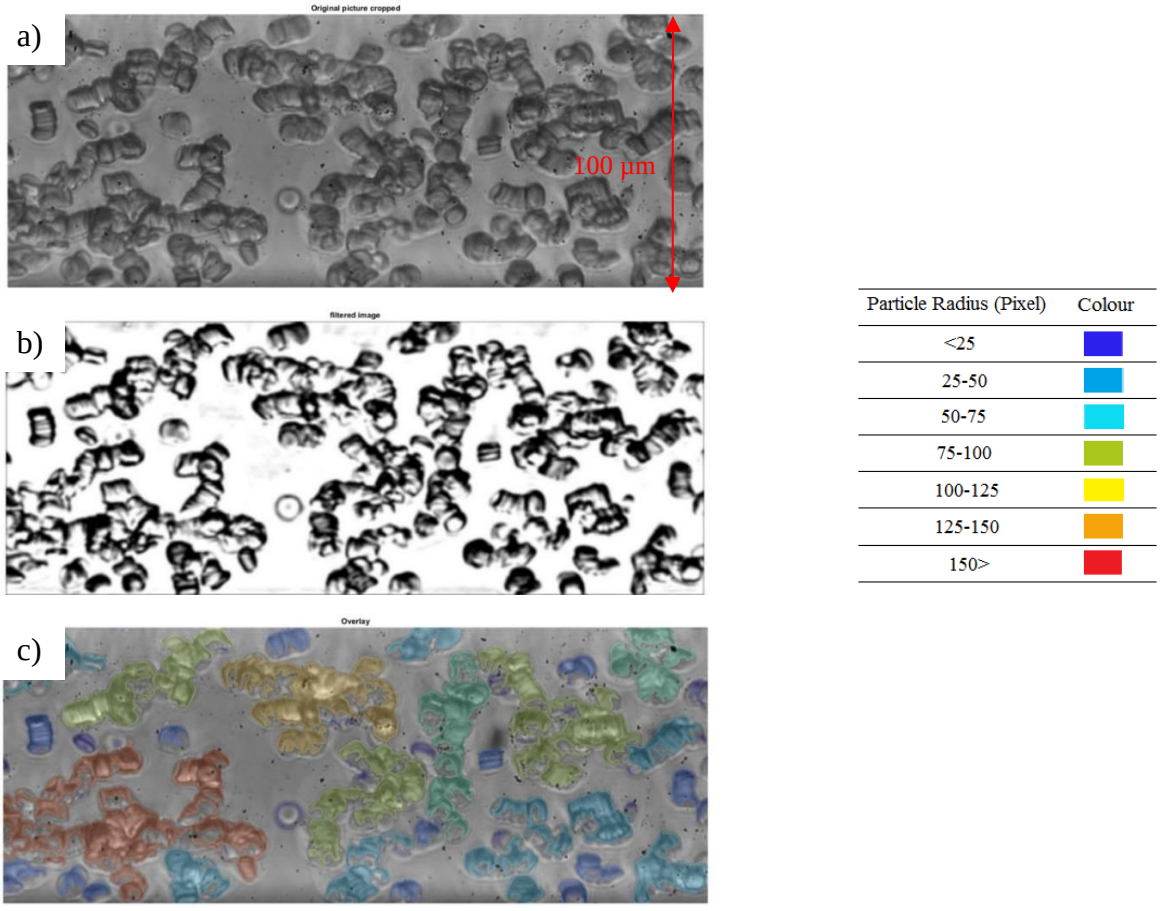

Figure 6.3: Image processing technique applied on the Channel flow set-up with flow rate of 12 µl/min a) Original image, cropped, b) Image after filtering, c) Overlay image

6.3 Macroscopic Aggregation and Disaggregation Rate

As it is discussed in Section 3.3 and Equation (3-6), by measuring the average number of cells per aggregate (AAS) and number density of red blood cells, n_0, the macroscopic aggregation rate, Ω_A, and disaggregation rate, Ω_B, can be estimated. In the sedimentation experiment, due to the low shear stress in the background fluid, low disaggregation rate is expected. Therefore, Equation (3-6) can be rewritten as

$$\frac{d(\mathrm{AAS})}{dt} = \frac{1}{2}\Omega_A n_0 . \tag{6-1}$$

The average aggregate sizes as a function of time are found using processed images for the first 150 seconds. Figure 6.4 shows the average aggregate size (AAS) as a function of the time for $H_t = 5\%$ and $H_t = 10\%$. To calculate the number density of red blood cells, hematocrit can be used directly. By estimating that the volume of a single RBC is 90 cubic micrometers, the number density of RBCs can be calculated. For example, for $H_t = 5\%$, the number density of RBCs is $n_0 = 5.556 \times 10^8 \ \frac{\text{particles}}{ml} = 5.556 \times 10^{14} \ \frac{\text{particles}}{m^3}$.

Now, using Equation (6-1), the macroscopic aggregation rate can be estimated. These results are shown in Table 6-1. In Table 6-1, the aggregation index is found using whole blood and the aggregometer introduced in Section 4.3. Each sample is tested three times and the range is shown in the table. These tests are done to show that the samples used in this research all have similar aggregation indices. It is important to note that, in the experiments, the actual hematocrit of each sample might be different from the intended hematocrit and it should be measured and checked using a micro centrifuge.

(a)

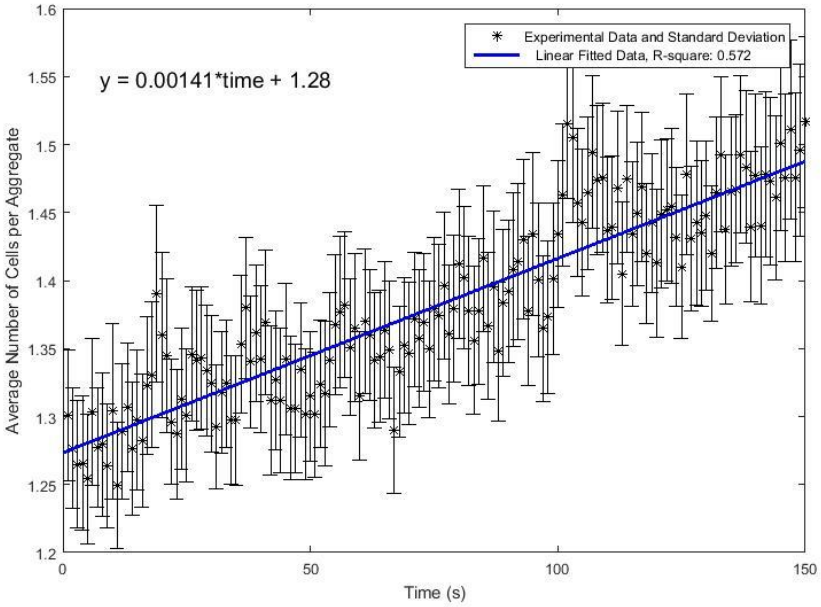

(b)

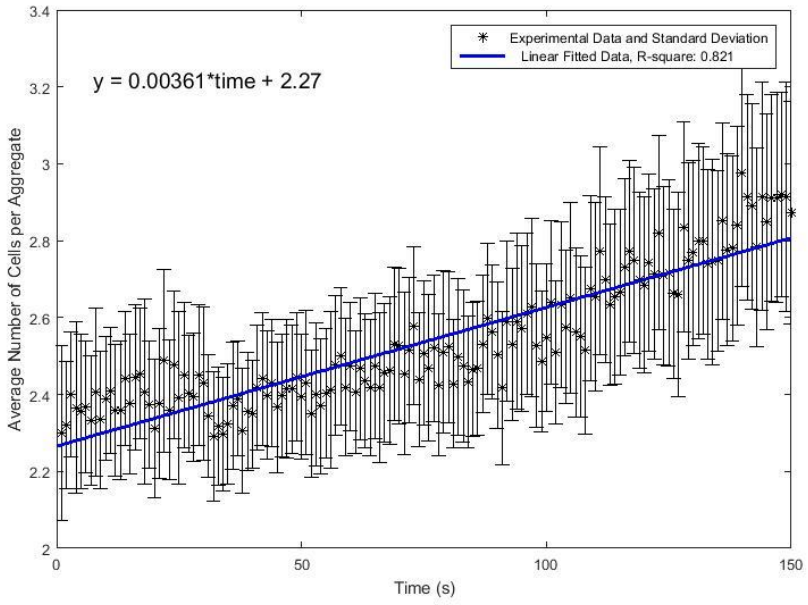

Figure 6.4: Change of the average aggregate size with time (Sample EI09A) a) $H_t = 5\%$ *b)* $H_t = 10\%$

Table 6-1: Macroscopic aggregation rate found from experiment for each sample

	Hematocrit $H_t = 5\%$			Hematocrit $H_t = 10\%$			
Sample	H_t	$\frac{d(AAS)}{dt}$ $1/s$	Ω_A ml/s	H_t	$\frac{d(AAS)}{dt}$ $1/s$	Ω_A ml/s	Aggregation index
EI09A	4%	0.0014	$6.3e^{-12}$	10%	0.0036	$6.5e^{-12}$	39.2 - 42.8
AO02A	6%	0.0023	$6.9e^{-12}$	12%	0.0057	$8.5e^{-12}$	37.7 - 38.4
EH06A	3%	0.0008	$4.8e^{-12}$	11%	0.0035	$5.7e^{-12}$	39.1 - 41.14
SE11A	5%	0.0021	$7.5e^{-12}$	11%	0.0040	$6.5e^{-12}$	38.6 - 40.36
EO09B	6%	0.0027	$8.1e^{-12}$	9%	0.0052	$10.4e^{-12}$	42.03 - 43.5

The average of macroscopic aggregation rates presented in Table 6-1 can be calculated as $\Omega_A = 7.1e^{-12}\ ml/s$. By finding this macroscopic aggregation rate, it is possible to find the disaggregation rate using Equation (3-6). In the Couette flow experiment, the flow is in steady-state conditions and the left hand side of the Equation (3-6) becomes equal to zero, therefore it can be written as

$$\frac{1}{2}\Omega_B (AAS)^2 - \frac{1}{2}\Omega_B (AAS) = \frac{1}{2}\Omega_A n_0 . \tag{6-2}$$

Knowing the aggregation rate from the previous step, the only unknown remaining in Equation (6-2) is macroscopic disaggregation rate (Ω_B). As discussed in Section 3.6, this term depends on the background fluid shear rate. In the experiment, shear rates are measured using micro-PIV and average aggregate sizes are measured using image processing for 5 different blood samples and several shear rates, as mentioned in Chapter 4. Figure 6.5 shows the collected data for estimated hematocrit of 5% by Mehri *et al*. [13]. As discussed in their research, although the hematocrit of the suspensions is measured before being injected into the microchannel, the hematocrit of the blood flowing in the field of view of the channel cannot be precisely controlled. In order to account for this difference, hematocrit was calculated from the microscopic images based on the aggregates detected in the microchannel [13].

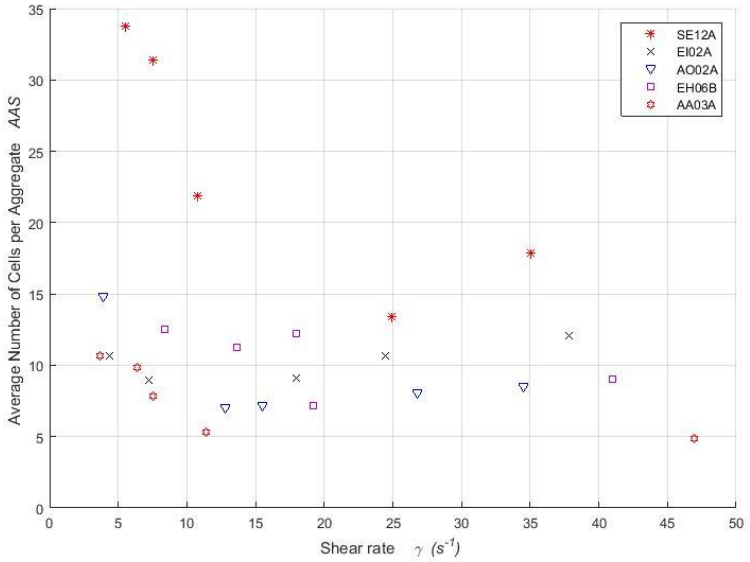

Figure 6.5: Change of average aggregate size with shear rate for approximate hematocrit of 5% [13].

The relation between disaggregation rate and shear rate is unknown. Owens suggested a power law correlation between disaggregation rate and shear rate [11]. On the other hand, Chen and Huang suggested a linear dependency between disaggregation rate and shear rate [88]. Matlab's "fminsearch" command is used for unconstrained nonlinear optimization. This command uses the simplex method to find a minimum for the error. It is found that the best fit for linear correlations can be presented as

$$\Omega_B = 5.01\times10^{-7}\dot{\gamma} + 8.2\times10^{-6}\ , \tag{6-3}$$

and similarly, for power law a correlation can be found as

$$\Omega_B = 3.8\times10^{-6}\ \dot{\gamma}^{\ 0.549}, \tag{6-4}$$

where the results for these fits are presented in Figure 6.6. The units for macroscopic disaggregation rate are s^{-1}. The average error for a power law fit, Equation (6-4), is 34% and for a linear relation, Equation (6-3), it is 33% compared to experimental results. As discussed, each sample has its own characteristics (plasma, aggregation rate and RBCs) and the relatively high errors are likely due to the variety of characteristics in different blood samples. Other sources of errors came from image processing techniques, as discussed later in Chapter 7.

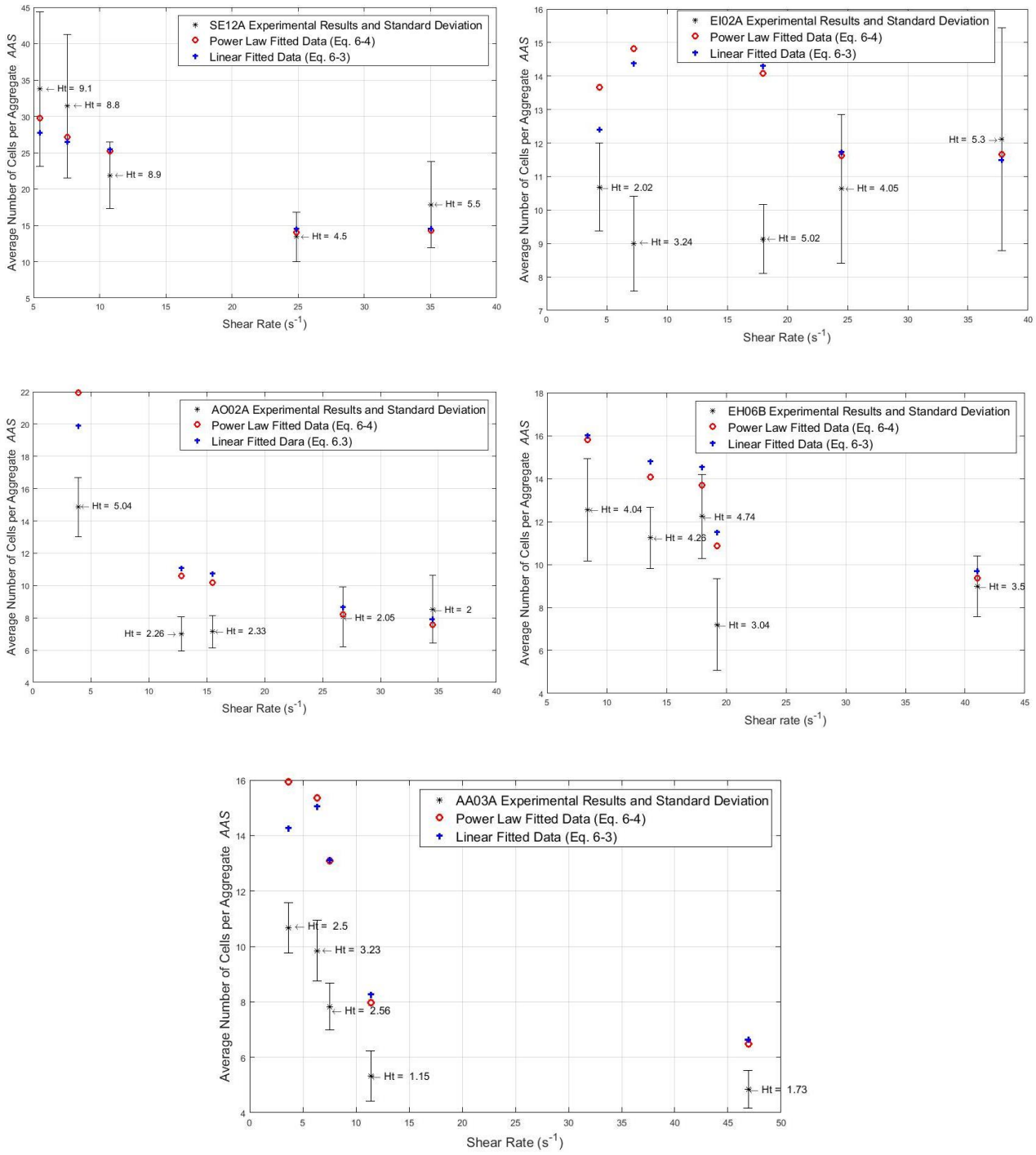

Figure 6.6: Change of average aggregate size with shear rate (5 samples) Experimental versus fitted data

Another suggestion by Owens [11] is a linear relationship between macroscopic aggregation rate and shear rate. To investigate this suggestion, a linear term is added to the

constant aggregation rate found in the previous step. Using the above results (Figure 6.5) and Equation (6-2) the optimized aggregation rate correlation is found as

$$\Omega_A = 7.1\mathrm{e}^{-12} - 1.7\times10^{-14}\dot{\gamma}\,. \qquad (6\text{-}5)$$

As the slope in Equation (6-5) is very small compared to the constant and use of Equation (6-5) does not improve the error compared to experiment, a constant aggregation rate is assumed.

6.4 Microscopic Aggregation Rate

According to Equation (3-12), the microscopic aggregation rate is the product of the collision rate and sticking probability. To find the collision rate using Equation (3-13), the velocity distribution of each class is needed. The Matlab code developed in Section 4.5 is used to find the particle size and velocity distribution in all experiments. Figure 6.7 shows the particle size distribution and Figure 6.8 shows the velocity distribution for the sedimentation experiment in the first 150 seconds of the experiment for sample EI09A.

The accuracy of the results in Figure 6.8 depends on the number of particles tracked in the domain. An accurate velocity distribution of particles cannot be reached unless a huge number of particles are tracked. But, as can be seen from Figure 6.7, the number of particles in the domain which can be tracked are of the order of 10,000 particles for smaller aggregates and of the order of 1000 particles for larger particles. In order to overcome this obstacle, the velocity distribution of particles in all experiments are combined together and used in Equation (3-15) to calculate the mean relative speed of particles, $\bar{g}$, between classes. Using this parameter in Equation (3-13) the collision rate of the particles between each class can be calculated. Table 6-2 shows the results for the relative speed in the sedimentation test found for 5 samples and two hematocrits. In this table the relative velocities between class 8 and other classes are not reported as it is assumed that particles in class 8 are not going to aggregate any further.

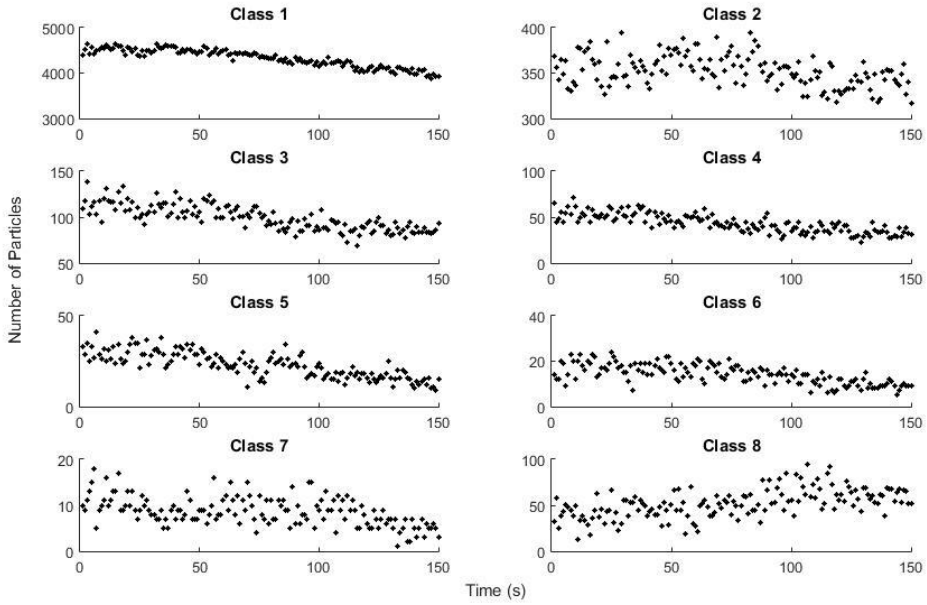

Figure 6.7: Particle size distribution for the sedimentation experiment. Sample EI09A

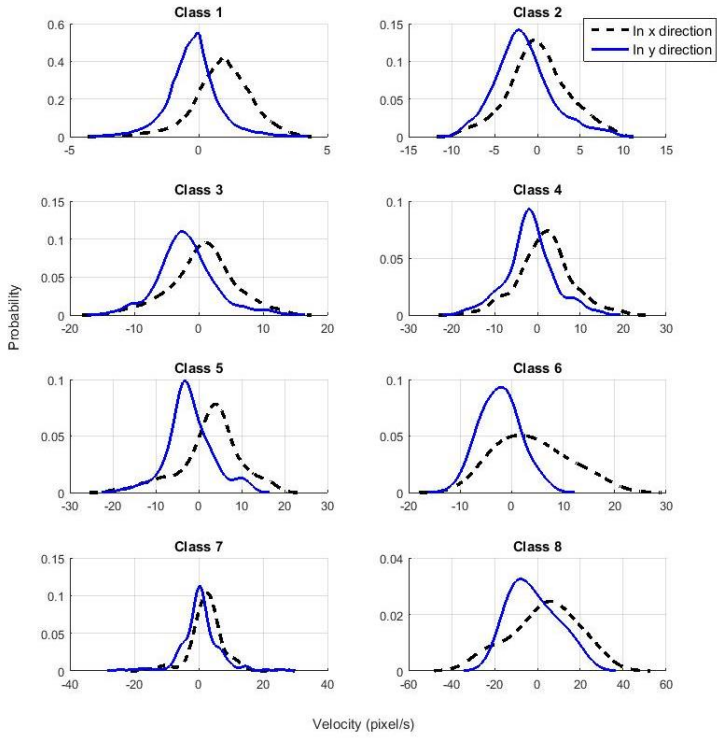

Figure 6.8: Velocity distribution of each class for the sedimentation experiment. From t=0 s to t=150 s Sample EI09A

Table 6-2: The mean relative speed of particles $\bar{g}$ between classes (pixel/s) in the sedimentation test

	Class 1	Class 2	Class 3	Class 4	Class 5	Class 6	Class 7
Class 1	4.7607	6.4474	8.4162	9.4787	10.9943	11.1340	11.589
Class 2	6.4474	7.6313	9.3298	10.3013	11.7739	11.8051	11.9495
Class 3	8.4162	9.3298	10.6876	11.4997	12.8692	12.9764	13.3406
Class 4	9.4787	10.3013	11.4997	12.2638	13.5322	14.1219	14.4398
Class 5	10.9943	11.7739	12.8692	13.5322	13.5322	14.7856	15.1284
Class 6	11.1340	11.8051	12.9764	14.1219	14.7856	15.1846	15.6575
Class 7	11.5890	11.9495	13.3406	14.4398	15.1284	15.6575	16.1213

The sticking probability is still needed to find microscopic aggregation rate. To find this parameter, the numerical model is combined with an optimization code, where sticking probabilities between each class are the optimization parameter. For this purpose, the initial condition for the numerical code is set similar to the initial values in the experiment. To do so, the density of particles in each class is calculated using the area of measurement window in the experiment and number of particles at $t = 0$ s. Measurements in the numerical model are done in a similar measurement window as was used in the experiment. An initial guess for sticking probabilities is set using a random number between zero and one. Matlab's "fmincon" function is used for this optimization and constraints for the optimization are set that all the optimized value be between zero and one. This function uses the "Interior point method" to minimize the objective function. The objective function for this problem is to minimize the absolute deviations of numerical model compare to experimental results. The optimization process is done several times and the values are compared to confirm that the optimized values are not a local minimum. Figure 6.9 shows the numerical results versus experimental results using optimized sticking probabilities for the sedimentation test.

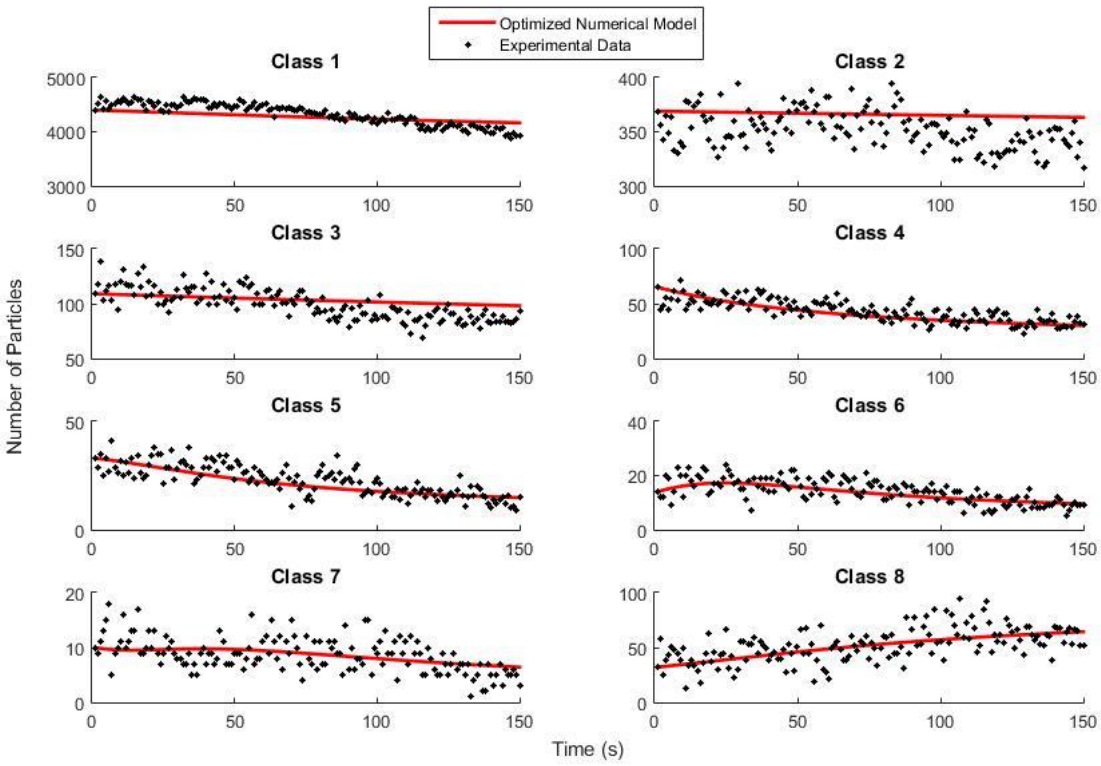

Figure 6.9: Numerical model results optimized to match experimental results in the sedimentation test. Sample EI09A

Table 6-3 shows the average value for the optimized sticking probability in the sedimentation test. This optimization is performed for five samples with hematocrit of 5%. It is important to say that only two blood samples' sticking probability values activated the constraint in the optimization. Those sample results are not included in the averaging as the optimizations were not deemed to be trustworthy. It should be noted that in this optimization 28 free parameters are used. Having all the values between the physical constraints despite having 28 degree of freedom gives confidence that the model is working as expected. Table 6-3 shows that sticking probability in smaller classes are higher. Another observation is that particles in a specific class prefer to aggregate with particles from the same class or neighbouring classes. Similarly, as it is assumed that there is no aggregation in class 8, the sticking probabilities for this class are not reported in Table 6-3. According to Equations (3-12) and (3-13), the microscopic aggregation rate can now be found using mean particle speed (Table 6-2) and sticking probability (Table 6-3) between classes.

Table 6-3: Average sticking probability values between classes for three samples

	Class 1	Class 2	Class 3	Class 4	Class 5	Class 6	Class 7
Class 1	0.78	0.84	0.65	0.17	0.13	0.21	0.005
Class 2	0.84	0.54	0.67	0.43	0.40	0.14	0.18
Class 3	0.65	0.67	0.82	0.21	0.51	0.35	0.16
Class 4	0.17	0.43	0.21	0.4	0.35	0.15	0.06
Class 5	0.13	0.40	0.51	0.35	0.25	0.29	0.10
Class 6	0.21	0.14	0.35	0.15	0.29	0.51	0.08
Class 7	0.005	0.18	0.16	0.06	0.10	0.08	0.2

In the Couette flow and channel flow, it is assumed that the sticking probability remains the same and only collision rate or, specifically, mean particle speed between classes are changing. In Appendix C, the mean particle speed between classes for different shear rates for one sample (EI02A) are presented. The Matlab program developed in Chapter 4 can be used to find a similar table for any experiment including the channel flow. In the next section, these values are applied in the numerical code and experimental results are compared with the numerical model values.

6.5 Microscopic Disaggregation Rate

To estimate the microscopic disaggregation rates, Equation (3-17) is used. As discussed in Section 3.6, it is assumed that, when a particle breaks, two daughter particles of the same size appear. This assumption, in combination with the particle classification used in this research, simplifies the microscopic disaggregation rate greatly. Looking back to Equation (3-3), in the case of a steady-state and fully developed flow, one finds

$$B_{B\kappa} - D_{B\kappa} + B_{A\kappa} - D_{A\kappa} = 0 \qquad \text{for} \quad \kappa = 1,...,N. \tag{6-6}$$

Equation (6-6) results in a balanced equation between deaths and births of particles due to aggregation and disaggregation. In the Couette flow experiment, both steady-state and fully-developed conditions are met and, therefore, Equation (6-6) can be applied. The microscopic

aggregation rates discussed in the previous section can be used to estimate births, $B_{A\kappa}$, and deaths, $D_{A\kappa}$, due to aggregation. To do so, sticking probabilities found in the previous section are applied in Equation (3-11). Similarly, Equation (3-17) can be applied to birth, $B_{B\kappa}$, and death, $D_{B\kappa}$, due to disaggregation. By knowing the balanced number density of particles from the Couette flow experiment, this procedure results in a system of algebraic equations where only the breakage frequencies of particles in each class, $\omega_{\kappa,\kappa-1}$, are unknown.

As an example, Figure 6.10 shows the balanced number of particles for the sample SE12A and for 5 different shear rates in the Couette flow. It can be seen that in higher shear rates red blood cells tend to be in smaller classes and by decreasing the shear rate less particles are present in smaller classes. This figure is generated using the Matlab program presented in Chapter 4 and the number of particles is found by averaging the number of particles in all acquired images. Similar results are generated for 5 different samples and all are used in an optimization process to find the breakage frequency as a function of shear rates. A linear function is assumed for dependency of breakage frequency on shear rate. This linear function does not include any constant since as shear rate goes to zero, disaggregation rate is assumed to equal zero. In the optimization process, the goal function is defined to minimize the sum of the errors coming from the comparison of the experimental results and Equation (6-6) results. The "fminsearch" Matlab function is used for the optimization process and the following results are found to minimize the least absolute error of Equation (6-6) to 7.2%. This error is smaller than what is found in macroscopic model. This is expected, as there are more degrees of freedom in the microscopic model. The following relations for disaggregation frequency are found and used in this research,

$$\begin{aligned}
&\omega_{2,1}=0.35\dot{\gamma}, \quad \omega_{3,2}=1.91\dot{\gamma}, \quad \omega_{4,3}=2.81\dot{\gamma},\\
&\omega_{5,4}=3.11\dot{\gamma}, \quad \omega_{6,5}=3.85\dot{\gamma}, \quad \omega_{7,6}=4.07\dot{\gamma},\\
&\omega_{8,7}=3.33\dot{\gamma},
\end{aligned} \tag{6-7}$$

where the units for the microscopic disaggregation rate are s^{-1}.

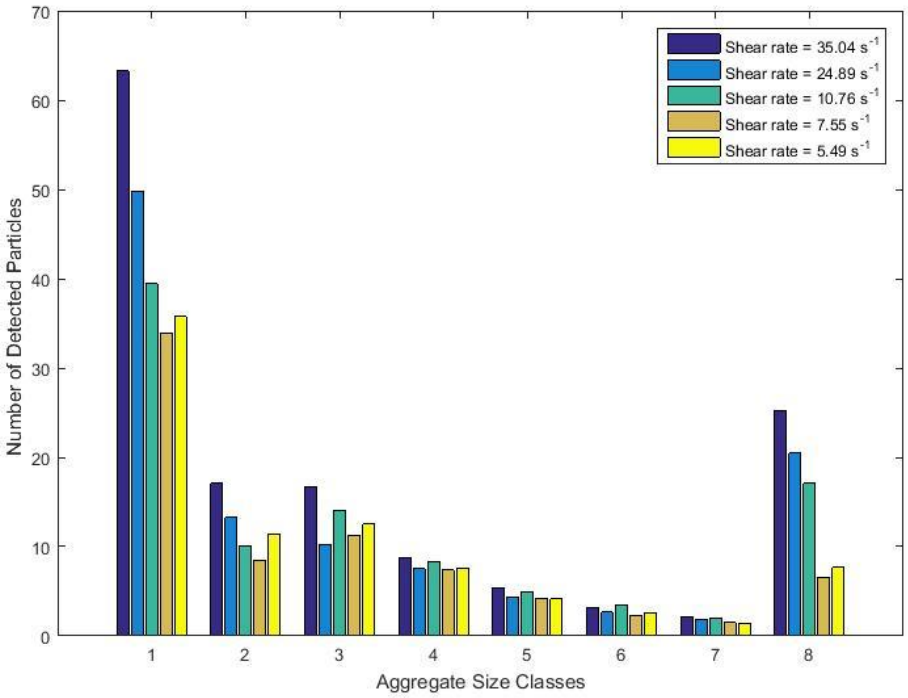

Figure 6.10: Particle size distribution in the Couette flow experiment for different shear rates for SE12A

Looking at the results presented in Equation (6-7), it can be argued that bigger particles are more prone to breakage compared to smaller particles. Also at no shear stress condition there is no particle disaggregation. The only exception to this argument is the largest particle size. This inconsistency might be the result of several assumptions that are made that are unique to this largest particle size. One of these assumptions is that there is no aggregation in this class. Another assumption in the image processing procedure is that any particle bigger than this size is also stored in this class. Considering these assumptions, this inconsistency for the largest particles is not surprising. To compare the microscopic model to the macroscopic model, the average aggregate size from Equation 6-4 is compared to that predicted using the current model in Figure 6.11. This comparison shows that by increasing the details of the model, it is easier to predict the size of particles in the domain more accurately. The predictions of the present microscopic model are always closer to the experimental data than those of the previous macroscopic model.

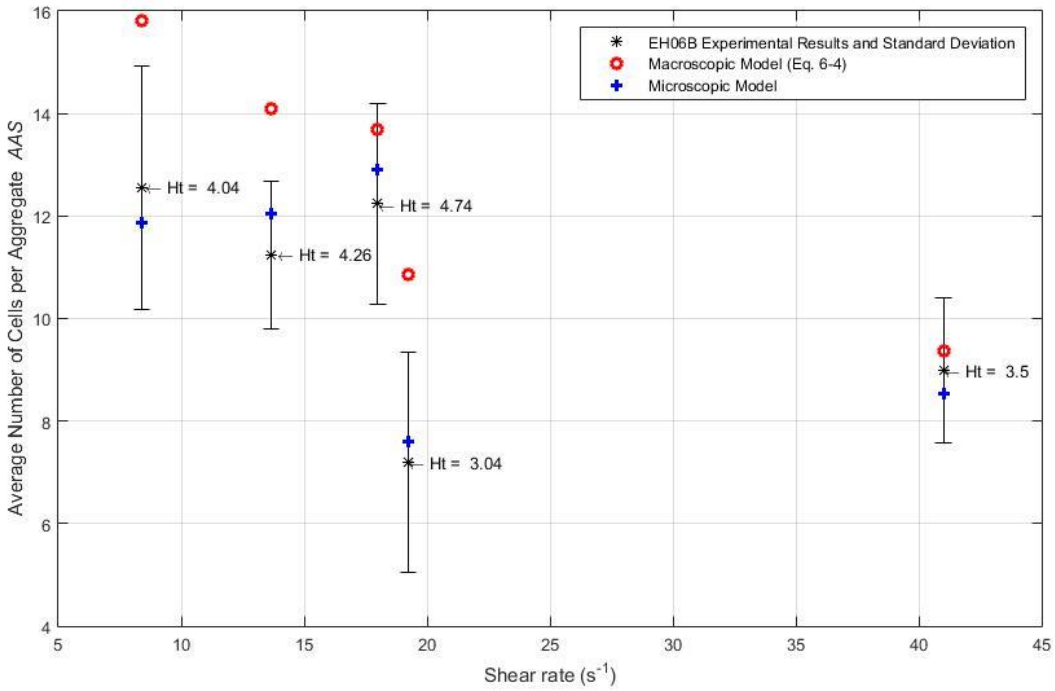

Figure 6.11: Change of average aggregate size with shear rate Experimental versus macroscopic and microscopic model (EH06B sample)

6.6 Ellipsoidal Particle Geometry

The last experimental parameter needed to complete the model is a description of the shape of the particles in the domain. This description is used in the calculation of drag force (Section 3.7.3) and intrinsic viscosity (Section 3.7.8). It is assumed that rouleaux have an oblate spheroid shape instead of an ellipsoid shape. This assumption results in two unknown parameters for each class instead of three. The major semi-axis and minor semi-axis are these two unknowns. To measure these parameters experimentally, the image processing method presented in Section 4.5.4 is used. The semi-axes of the ellipses reported in this section are assumed to be the major and minor semi-axes of the oblate spheroid. These results are slightly different for each shear rate or flow rate in Couette or channel flow. To reduce the dependency of the numerical model on the experiment, this small difference is ignored by averaging all the results. The probability density functions describing the particles' semi-axes lengths are presented in Figures

6.12 and 6.13. These results are for the channel flow experiment with hematocrit of 10% and flow rate of 12 µl/hr. It can be seen that both major and minor semi-axes are increasing with the size of particles.

From similar results for all the experiments (Couette and channel flow), Table 6-4 can be extracted. In this table particle semi axes are reported according to determined size as discussed in Table 4-1. As can be seen in this table, by considering that the minor semi axes are the same, it is impossible to have the same volume as spherical particles. There are several reasons behind these results. The most important one is that in both Couette and channel flow, the experiments are two dimensional and the shear near the walls makes two dimensional rouleaux. In the numerical modelling, this is not important and only the volume of particles is important. Another source of error in this table is that these numbers represent a wide range of particles that are classified in one size. To have the same volume as in Table 4-1, in this research only the major semi axis is used and the minor semi axis is found using the estimated volume of particles.

Table 6-4: Average geometric quantities for each particle family.

Class κ	Number of RBCs	Estimated Radius (µm)	Major Semi-Axis (µm)	Minor Semi-Axis (µm)	Calculated Minor Semi-Axis (µm)
1	1	2.780	2.44	1.05	2.97
2	2	3.503	3.35	1.65	3.58
3	4	4.413	4.95	2.5	4.17
4	8	5.560	6.83	3.93	5.01
5	16	7.005	8.75	5.23	6.27
6	32	8.826	12.53	7.98	7.41
7	64	11.120	15.41	8.78	9.44
8	128 and more	14.011	19.68	10.59	11.83

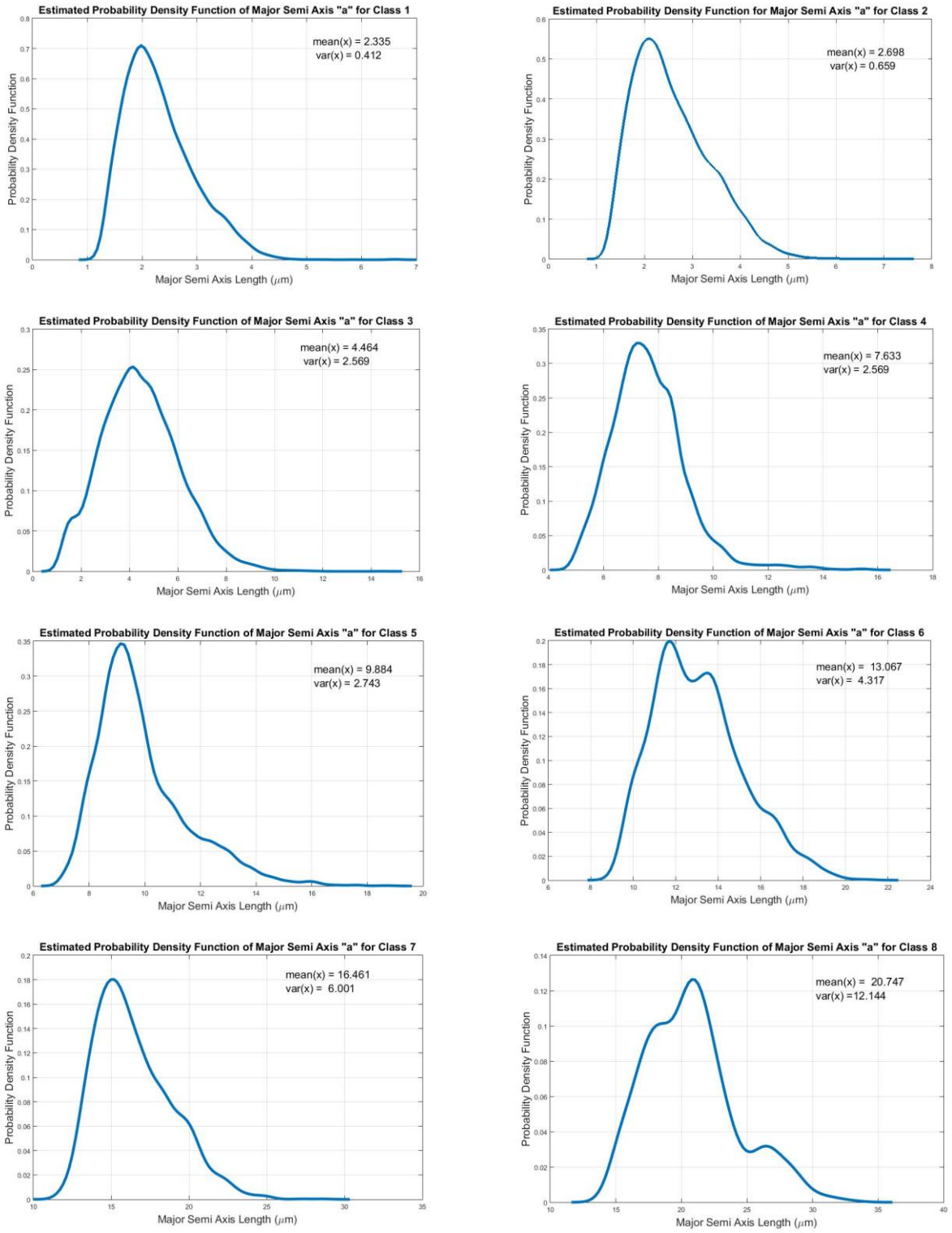

Figure 6.12: Probability density function of the particles major semi axis in channel flow experiment with hematocrit of 10% and flow rate of 12 µl/hr.

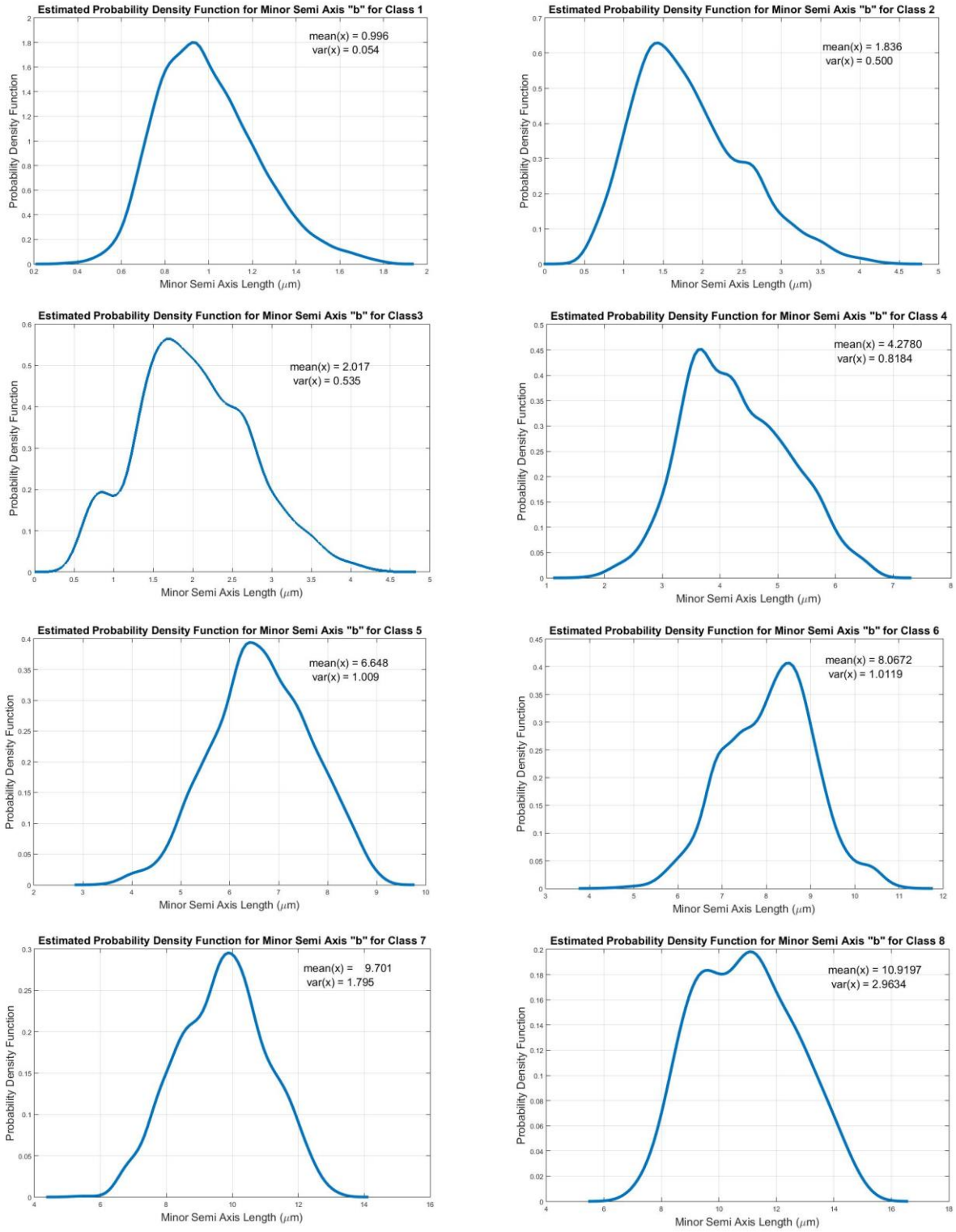

Figure 6.13: Probability density function of the particles minor semi axis in channel flow experiment with hematocrit of 10% and flow rate of 12 µl/hr.

6.7 Validation of the Numerical Code

6.7.1 Sedimentation Set-up

Now that aggregation and disaggregation rates have both been found, the model is complete. To validate the model with experiment, first the growth rate of a sedimentation layer is compared. In this experiment, particles aggregate and settle at the bottom of the domain. Larger particles settle faster due to a smaller drag to weight ratio and smaller particles settle more slowly due to a higher drag force to weight ratio. These particles form a sedimentation layer at the bottom of the domain which can be seen in Figure 6.14. This figure shows sedimentation layer growth in the experiment (sample EH06A 10% hematocrit) as a function of time. Similar results can be obtained from the developed model. In Figure 6.15, the numerical results are shown for the same instant in time. It is important to note that Figures 6.14 and 6.15 are not at the same scale.

This layer is detected as a single particle in the domain by the developed Matlab program. To measure the depth of this layer in the experiment, first, the closest particle to the bottom wall is selected, then, the vertical distance of the centre of the area of this particle to the bottom of the domain is measured and multiplied by two. This particle is representing the sedimentation layer as shown in Figure 6.14. In the numerical model, this layer is recognized when a computational cell's particle volume fraction reaches 98% of the maximum packing fraction. In the numerical model, to have the most similar geometry to the experiment and to have the same amount of particles in the domain, the height of the field is five times greater than its width. This simulation starts with single RBCs with volume fraction of 10% and it runs to a final time of 150 seconds. The aggregation is the reason for the formation of bigger particles and faster sedimentation. Table 6-2 is used as the input for the aggregation function. The grid used for this simulation is 200 by 200 and eight classes of particles and background fluid are solved together including all acting forces on particles. To quantitatively compare the position of the sedimentation layer, both experimental and numerical model values are compared in Figure 6.16. It can be seen that both model and experiment follow the same path. The growth rate of this layer is fast at the beginning and when the bigger particles have settled, this rate becomes smaller. Another observation that can be made is that ellipsoidal particles have less drag force on them and settle faster compared to the spherical particles. This is the reason behind a larger layer for ellipsoidal particles.

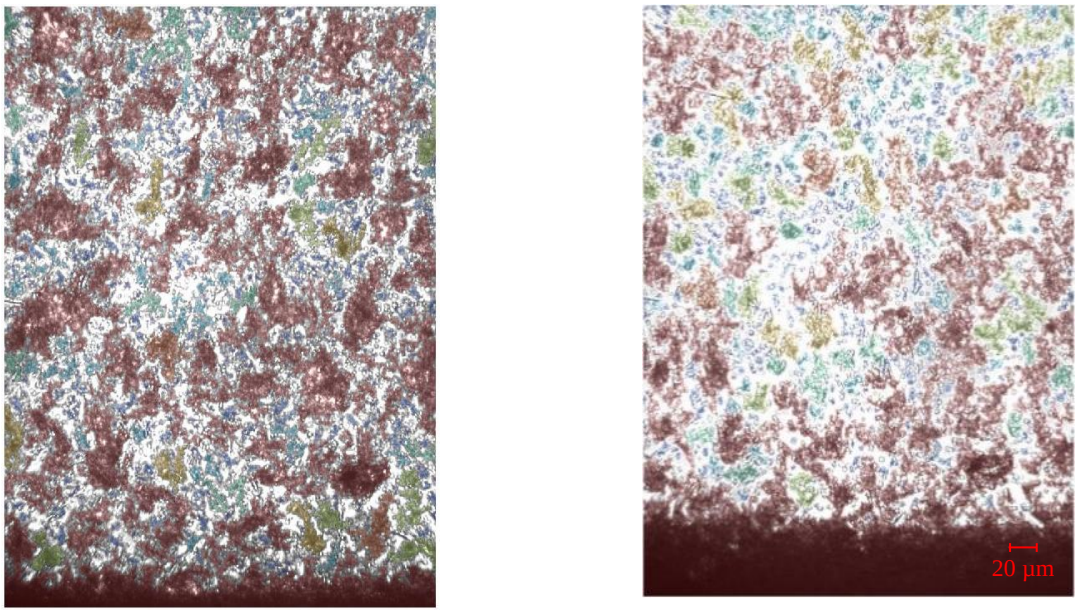

t = 40 *s* *t* = 110 *s*

Figure 6.14: Sedimentation layer growth in the experiment

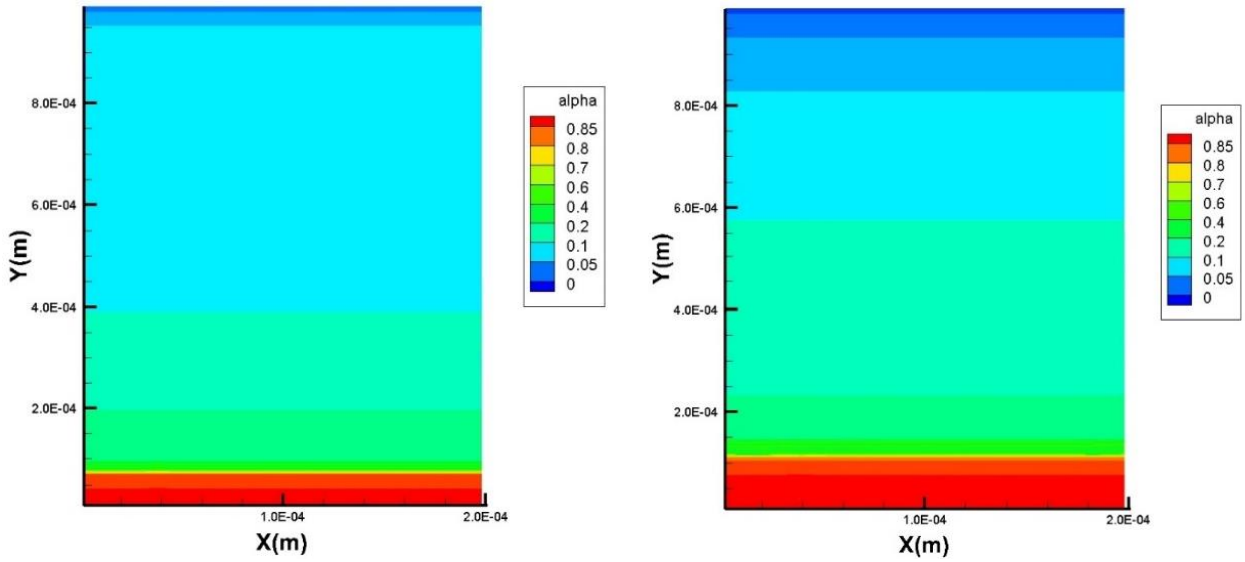

t = 40 *s* *t* = 110 *s*

Figure 6.15: Sedimentation layer growth rate in the numerical model

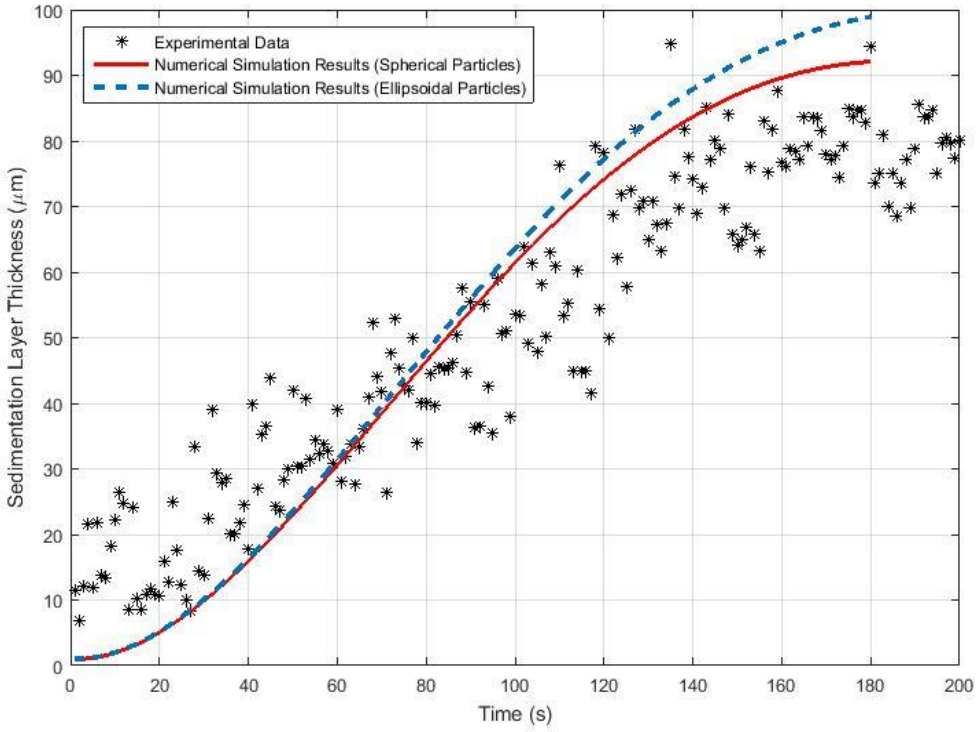

Figure 6.16: Sedimentation layer position growth in time for both experiment and numerical model for volume fraction of 10%.

6.7.2 Couette Flow and Channel Flow

The next step is to validate if the Couette and channel flow simulations match with the experimental results. These flows are steady-state and both aggregation and breakage functions are important. To validate the numerical code, the simulation starts with the same hematocrit as the experiment (10%) and it runs until it reaches steady-state conditions. Considering the balance of the forces in the steady-state condition, particle velocity should be the same as background fluid velocity. The effect of the lift force gets smaller as the particle velocity gets closer to the background flow (Equation 3-34). This means that the model results depend on the initial distribution and velocity of the particles. It is important to note that the same principle is applied to the experiment and the formation of the cell-free layer can depend on the initial velocity of particles in the domain. In this study, the simulation starts with uniformly distributed particles with zero velocity.

In the Couette flow, the velocity of the upper wall is $V = 20\ {}^{\mu m}/_{s}$ and a no slip boundary condition is used for both walls. Periodic boundary conditions are used on the left and right boundaries. For the channel flow the sum of the flow rates of particles and plasma is set to be $Q = 12\,\mu l/hr$ and periodic boundary condition for particles and plasma are set on the boundaries. The grid for both of these simulations are 200 by 200. In Figure 6.17, the results of the simulation for these flows are shown. The formation of the cell-free layers in both of these simulations are noticeable. To study it more quantitatively, the volume fractions of red blood cells are plotted at x = 0.008 m in Figure 6.18.

These results can be compared to the experimental results qualitatively. Figure 6.19(a) shows an image from experiment done by Mehri [13] at 10% hematocrit. By stacking all the images of different times together and averaging the light intensity of the stacked picture, Figure 6.19 (b) can be produced. Intensity profile of vertical lines in this picture shows the probability of presence of particle in that location during the experiment. Figure 6.19 (c) shows the averaged intensity profile of all vertical lines in the picture. Similarly for channel flow [134] the same procedure is done and shown in Figure 6.20. Although it is not possible to compare the numerical results with experimental results quantitatively, qualitatively Figure 6.19 (c) can be compared to Figure 6.18 (a) and similarly Figure 6.20 (c) can be compared to Figure 6.18 (b). The problem with using light intensity is that the maximum intensity is not correlated to a known volume fraction and therefore these graphs cannot be compared directly. These figures show that near a wall boundary in the domain, where the no slip boundary condition is applied to the fluid flow, there are less particles, while there are more particles further from the walls.

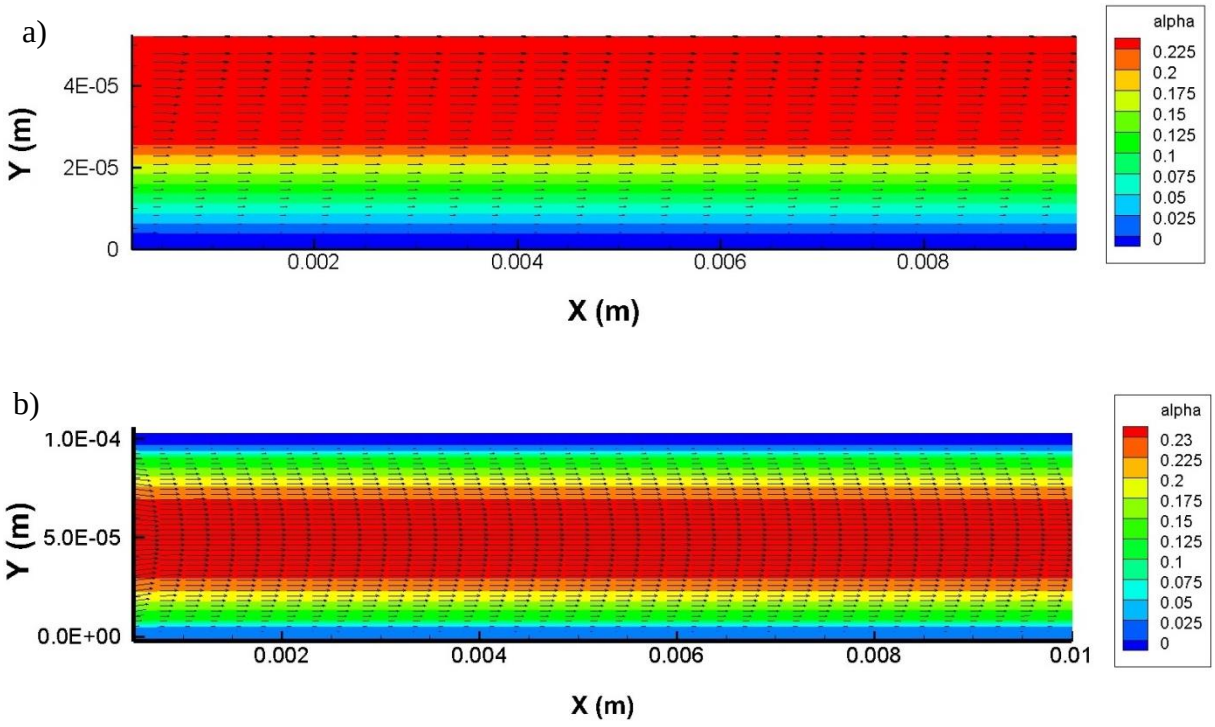

Figure 6.17: The numerical simulation of particles volume fraction fora) Couette flow $V = 20\mu m/s$ *and b) Channel flow* $Q = 12\,\mu l/hr$.

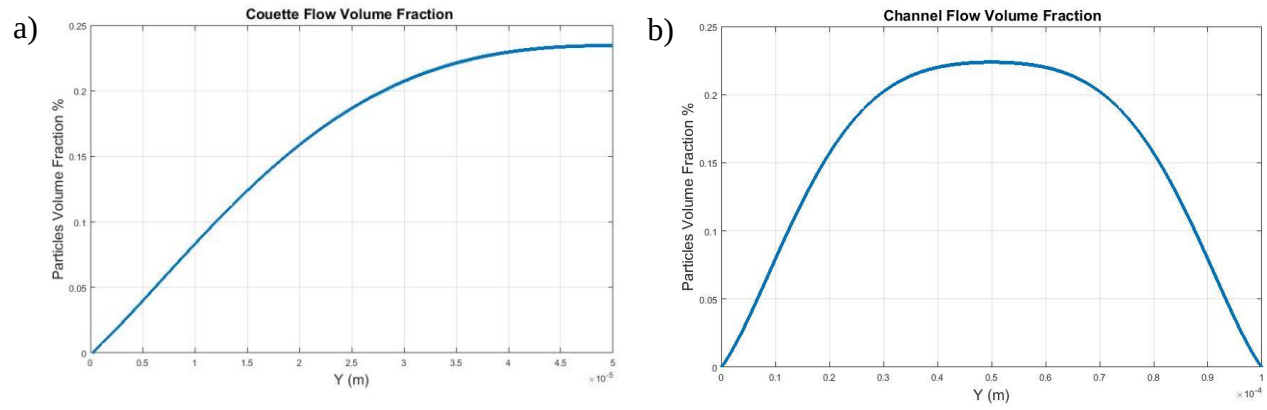

Figure 6.18: Particle volume fraction profile at x= 0.008 m of a) Couette flow $V = 20\mu m/s$ *and b) Channel flow* $Q = 12\,\mu l/hr$.

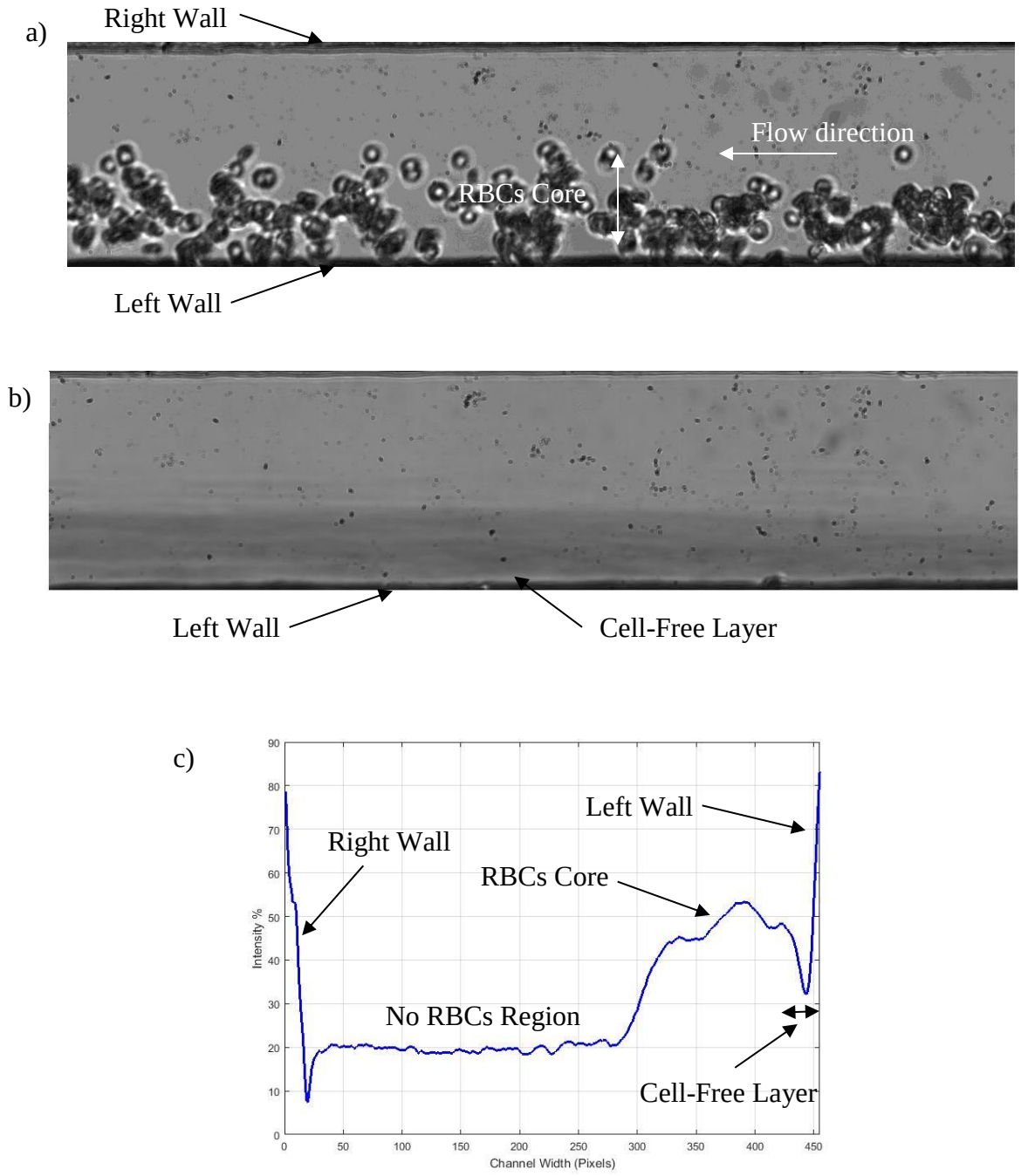

Figure 6.19: Cell-free layer in the Couette flow experiment (SE12A) a) An original picture of the Couette flow with 10% hematocrit b) Average of the light intensity of the stacked images c) Averaged intensity profile of all vertical lines

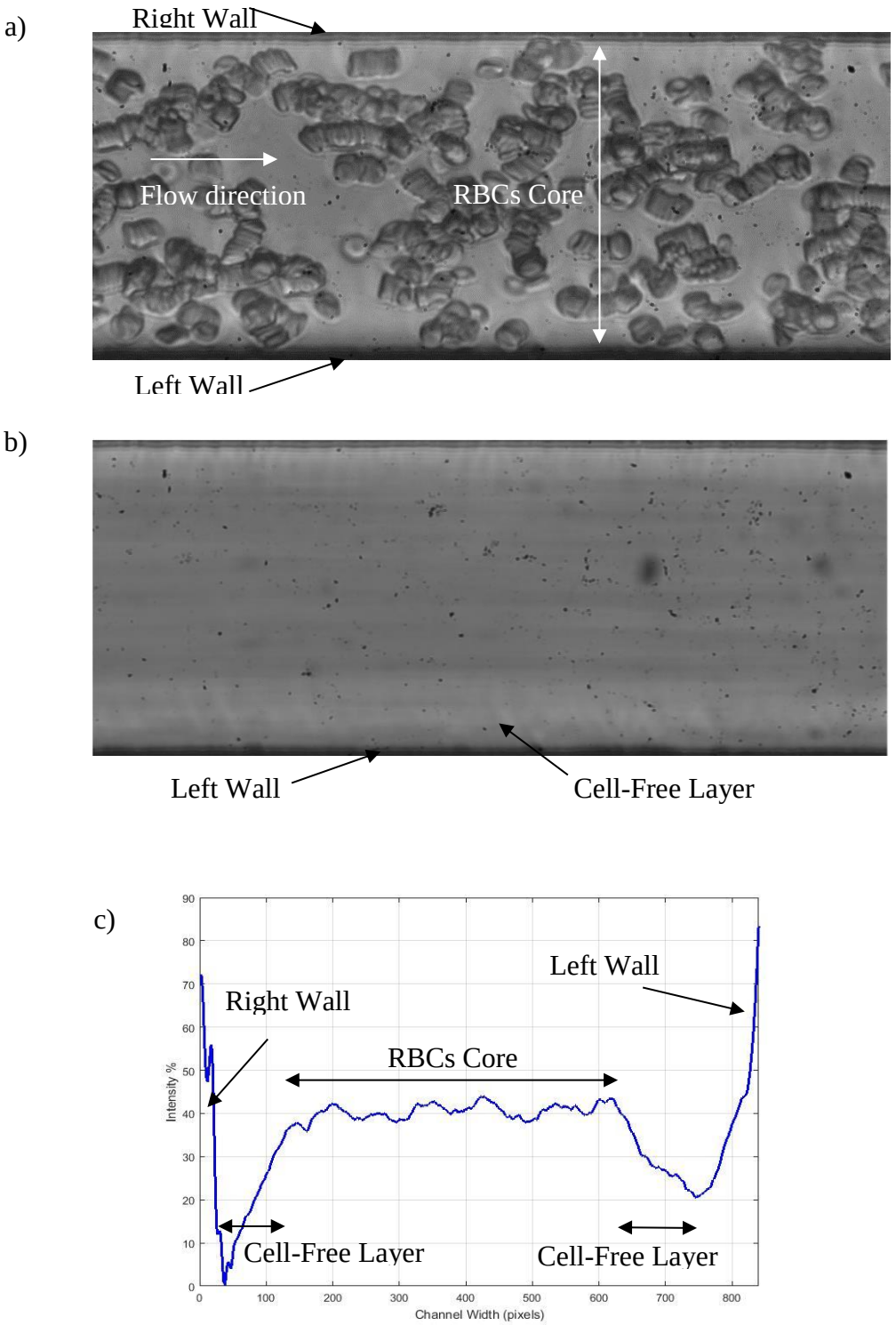

Figure 6.20: Cell-free layer in the Channel flow experiment (EH06C) a) An original picture of the Couette flow with 10% hematocrit b) Average of the light intensity of the stacked images c) Averaged intensity profile of all vertical lines

6.8 Apparent Viscosity

The ultimate goal of this model is to predict the whole-blood apparent viscosity. The experimental results of Figure 2.1 are used to compare the numerical results with experiment. It is assumed that the whole blood has an average hematocrit of 40%. To measure the apparent viscosity, a channel-flow simulation is used. The method used to find the apparent viscosity versus apparent shear rate is very similar to the one used in capillary viscometers [63]. To calculate the apparent viscosity of whole-blood, Equation (2-1) is modified to be used in a two dimensional channel flow as

$$\mu_{app} = \frac{w^3}{12L}\frac{\Delta P}{\widehat{Q}}, \tag{6-8}$$

where, w is the width of the channel and in this simulation is 100 μm. The parameter L is the length of the channel, where inlet and outlet pressures are measured to calculate the pressure drop. Volumetric flow rate per meter, $\widehat{Q}$, is calculated to correspond to the sectional velocity profile of the experimental channel flow.

To compute collision rates, measured particle relative velocities from the experiments of Gliah [134] are used. These experiments are done for apparent shear rates of 28 s^{-1}, 56 s^{-1} and 84 s^{-1}. To compute the volumetric flow rate per meter in 2D, $\widehat{Q}$, theoretical maximum velocities of the experiment (0.916 mm/s, 1.83 mm/s, and 2.75 mm/s) are used. Parabolic velocity profiles with these maximum velocities are used to calculate volumetric flow rate in the two dimensional channel. By using this method, the same apparent shear rate as the experiment can be achieved in the two dimensional channel. These experiments are done using 10% hematocrit and it is assumed that the hematocrit does not affect particle relative speeds. This assumption is discussed further in the next section. Using the image processing methods discussed in Chapter 4, the particle relative speeds are calculated and presented in Appendix C.

The parameter which is used from the numerical model to calculate the apparent viscosity is the pressure drop over a specific length. The flow rate and relative velocity of particles are the input of the numerical model. The same geometry and specification shown in Figure 6.17 are used in the model and the average pressures at the inlet and outlet are reported when the

simulation reaches the steady-state condition. Figure 6-21 shows the convergence study of the pressure drop with time in a simulation with 12 µl/hr flow rate. As can be seen it takes at least 50 seconds for the fluid flow to converge to the final solution. Similar measurements are done to insure the convergence of other cases.

Figure 6.22 compares the numerical model results for apparent viscosity to experimental results. First, to verify the discussed method to find apparent viscosity, a case with no particles is simulated with a shear rate of 56 s^{-1}. By using Equation (6-8) and the pressure drop found in the simulation, the plasma viscosity is predicted accurately. Next, the complete model is used to predict blood apparent viscosity using elliptical and spherical particles. As shows using elliptical particles predicts the viscosity more accurately, as compared to spherical particles. As these cases are in steady-state conditions, particles have the same velocities as the background fluid and the only parameters that affect viscosity are the intrinsic viscosity and the formation of cell-free layer.

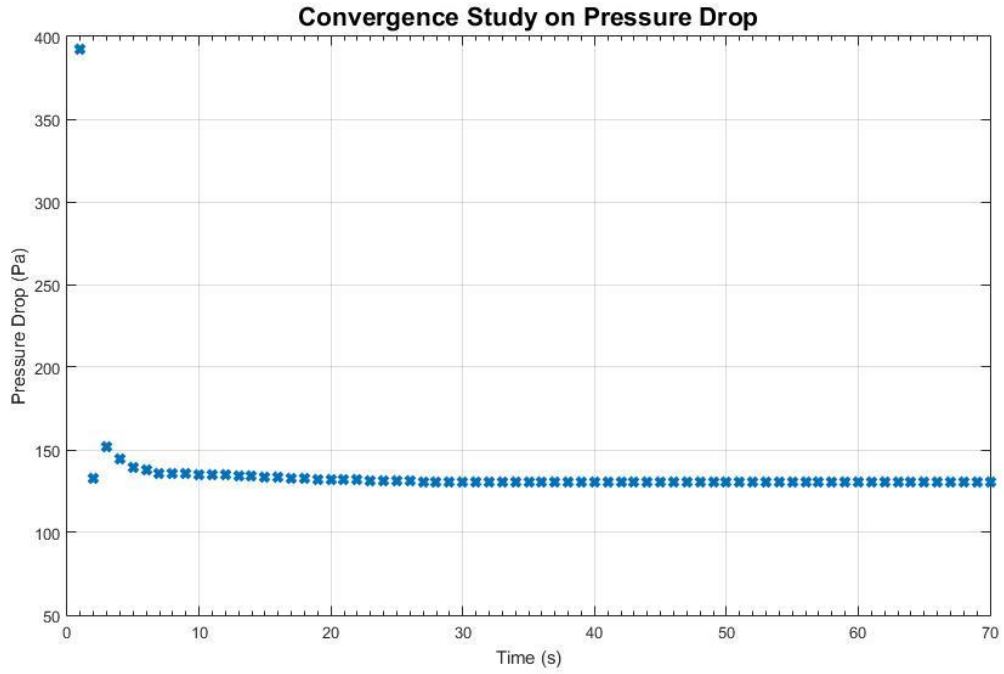

Figure 6.21: Convergence study of the pressure drop in channel flow with 12µl/hr.

To further investigate the effect of each component of the model, three specific case results are compared in Figure 6.23. In all the cases, elliptical particles with the same specification as those in Table 6-4 are used. Flow rates are the same and are set to 12 µl/hr so that the maximum velocity of the Newtonian flow is 1.83 mm/s. The same channel flow geometry discussed before is used in all cases.

In the first case, particle initial velocities are set to have a same parabolic profile as the background fluid. By using the same initial velocity for both particles and background fluid, drag (Equation 3-31) and lift force (Equation 3-34) become equal to zero. Therefore, a cell-free-layer is not formed and the velocity profile follows the parabolic profile. This parabolic profile is shown in Figure 6.23, case 1. In the second case, aggregation of particles is turned off. In this case, all the particles are single red blood cells. As particles have zero velocity at the initial condition, a cell-free-layer is formed with time. It can be seen in Figure 6.23 that, this case velocity profile is very close to parabolic. In this case, red blood cells reach their terminal velocity very quickly, as they are very small and the drag force on them is very high. This will result in a more uniform distribution of particles in the domain. The last case that is shown in Figure 6.23 is the complete model with zero initial velocity for particles at the beginning of the simulation. It can be seen that velocity profile increases more steeply near the walls compared to other cases. Table 6-5 compares the apparent viscosity of these cases.

Table 6-5: Apparent viscosity for different case studies with hematocrit of 40%, apparent shear rate of 56 s^{-1} and elliptical particles.

	Apparent Viscosity Pa.s	Characteristics
Case 0	0.0013	No particles – Plasma viscosity
Case 1	0.0027	Same initial velocity for both particles and background fluid
Case 2	0.0031	Single particles and no aggregation
Case 3	0.0093	Complete model with zero initial velocity for particles

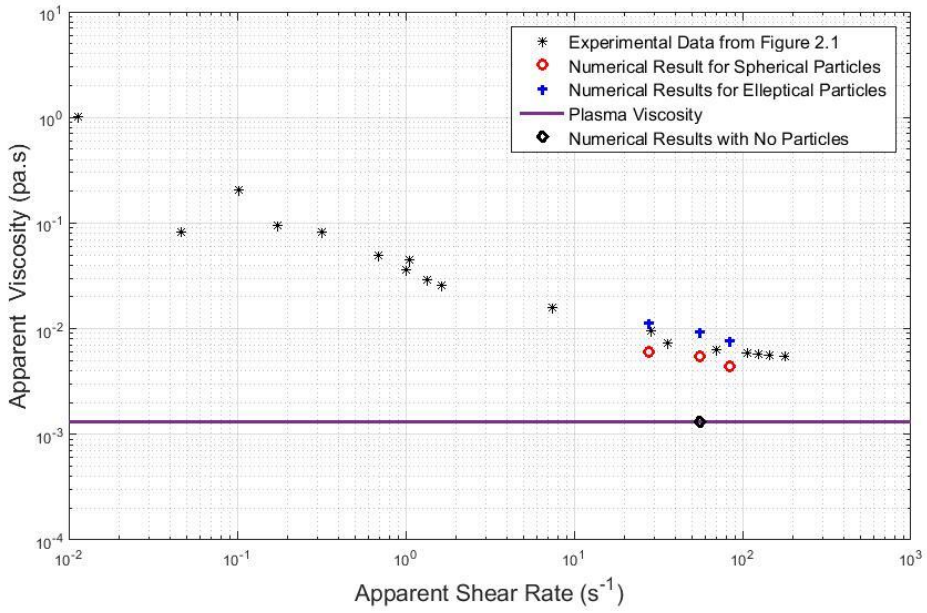

Figure 6.22: Whole-blood apparent viscosity, comparison of the numerical model with the experimental data [57].

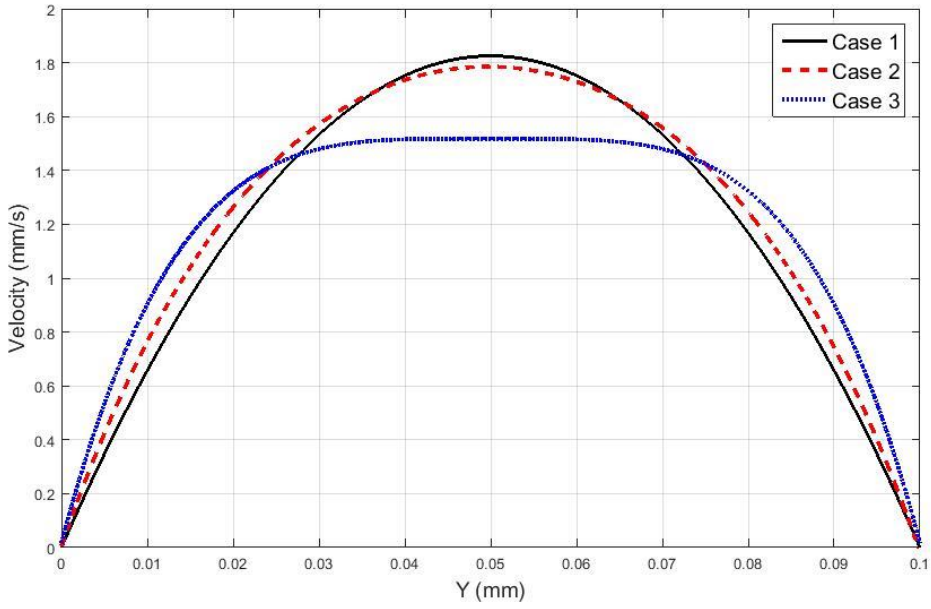

Figure 6.23: Velocity profile of flow with apparent shear rate of 56 s^{-1}, numerical results for: Case 1- particles with initial velocity identical to the background flow. Case 2- No aggregation. Case 3- Complete model

6.9 Effects of the Bulk Hematocrit on the Simulation

An important parameter that effects both simulation and experiment is the sample hematocrit. To study the effects of this parameter on the simulation results, a channel flow set-up similar to the one used in the previous section is used. The only parameters that is changed here is the bulk hematocrit; the apparent viscosity versus the bulk hematocrit is shown in Figure 6.24 and the normalized volume fractions for each bulk hematocrit is shown in Figure 6.25. The hematocrit is normalized using the maximum local hematocrit of the channel.

As shown in Figure 6.24 increasing hematocrit result in increasing the apparent viscosity. This is expected as the intrinsic viscosity increases with the density of particles. Comparing these results to the experimental results presented in [3], it can be seen that although the model predicts a linear increase in the viscosity, in the experimental results viscosity increases more exponentially. This difference might be coming from the fact that red blood cells are very deformable and their interactions in the flow is not completely simulated in this model.

Figure 6.25 shows the steady state normalized volume fraction distribution for each bulk hematocrit. Higher hematocrits have a sharper slope near the walls. This slope can be correlated to the cell free layer that becomes smaller as the concentrate core is larger. The current model predicts a decrease of the cell free layer size with an increase in hematocrit. This prediction follows the experimental results in the literature [7, 58, 62].

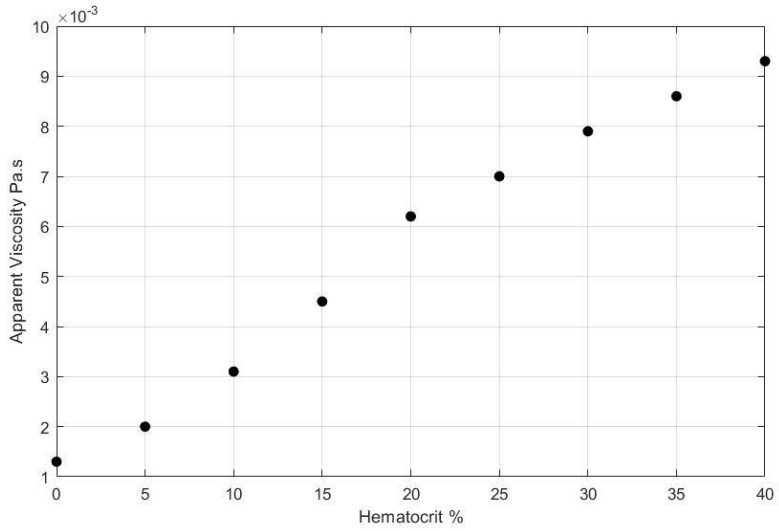

Figure 6.24: Hematocrit versus apparent viscosity for the channel flow simulation with apparent shear rate of 56 s^{-1}

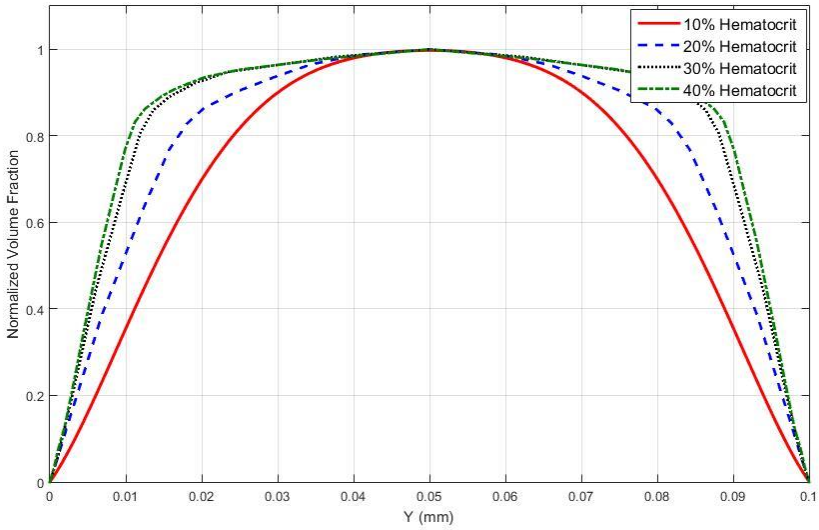

Figure 6.25: Steady state normalized volume fraction for the channel flow simulation with apparent shear rate of 56 s^{-1}

6.10 Model Limitations

This model shows promising results, when compared to experiment; it simulates particle distribution and therefore predicts the local viscosity of blood. Nonetheless, this is a very complicated model and there are some aspects that need to be improved. Though predicted viscosity from this model shows promise, it does rely on several parameters that must be measured from experiment for each situation of interest. In this section all the limitations of the model is summarized.

The first part that might be a source of error in the model is performing a 2D analysis of a 3D problem. This includes calculating flow rates, assuming an oblate spheroid shape for rouleaux and ignoring the three dimensional geometry and shape of particles. Another source of error in the model is assuming a RBC has rigid sphere characteristics. Most of the equations shown in Chapter 3 are for rigid spheres. This results in different lift which might change the measured viscosity. The accuracy of population-balance modeling depends on the number of classes used in the simulation. In this research, eight classes are used due to image processing restrictions. Improving this number might result in a more accurate model, but would increase numerical cost. The last source of error in this model is the fact that this model is developed for situations with low hematocrits. In the case of whole blood with a hematocrit of 40% the aggregation and disaggregation rates might be different. This assumption is applied inside the intrinsic viscosity model.

Another important limitation of the model is that currently, particle relative velocity plays a major role in the simulations. To do a simulation, an experiment should be performed first to find particle relative velocity. This limitation could be solved by extending the population balance method to also track particle velocity variance.

6.11 Summary

In this chapter, first macroscopic aggregation and breakage rates are found. These rates could be used in other numerical models directly and they are used to compare existing models to the presented model. To further develop the numerical model, microscopic aggregation and

disaggregation rates are found by combining the numerical model with a Matlab optimization code. Knowledge of these rates is required to close the model. To validate this model, several case studies, including sedimentation, Couette flow and channel flow, are compared with experimental results. In the next chapter there is further discussion of the model and the conclusion and contribution of this research are discussed.

Chapter 7

Conclusions and Future Work

7.1 Discussion and Conclusion

The model presented in this research is bound to experimental results, therefore in this section, first, the experimental results and limitations are discussed. It is assumed that the experiments are performed in two dimensions. Although this assumption is necessary to do image processing, particles are moving in all three dimensions. Particles can move over each other and overlap during the image processing. To reduce this error, rectangular channels with very small depth are used. As the RBCs tend to move away from walls, they should travel nearly at the centre of the channel. This small depth also results in high shear rate near the front and the back wall in the Couette and the channel flow. This high shear rate prevents 3D aggregates from forming. Due to this high shear rate, particles aggregation would happen more in two dimensions and is less in the third dimension. This effect will increase the accuracy of the image processing result, but, it might also result in underestimation of aggregation rate or overestimation of disaggregation rate compare to a real 3D aggregation formation.

Another interesting phenomena that can be noted in the sedimentation experiment is the shape of the aggregates. Instead of typical rouleaux shape, shown in Figure 1.1, aggregates have more spherical shapes. When bigger aggregates are formed in this experiment, the local shear rate around the aggregates has a different distribution compared to the channel flows, which may explains the particular shape. In addition, high relative velocity of large aggregates prevents other surrounding particles from attaching to the fast aggregates, which results in underestimation of aggregation rates for larger particles.

As discussed in Section 6.7.2, finding the cell free layer in the experiment is not practical as the light intensity profile cannot be mapped into the local particle distribution profile. In addition, the cause of the cell free layer is not very well understood. Several physical effects are proposed to explain cell free layer formation such as lift force, shear diffusion or cell collision. In the model, the Saffman lift force is used to simulate the formation of a cell free layer. Considering the lack of consensus in the literature, in this research, cell free layer thickness is not measured quantitatively, but investigated by looking at the spatial density distribution.

Another strong assumption made during the development of the model is the two-dimensional modelling. This simplification is made to link the quantitative parameters extracted from the two-dimensional experimental pictures. In particular the local density of RBC extracted from image processing give only two-dimensional spatial distribution. When modelling a three-dimensional problem using a two-dimensional model, it is important to note the physics that are removed by this assumption. Also, the definition of hematocrit, flow rate and other parameters changes when this assumption is made.

Looking at the literature, research in this area is either confined to numerical modelling or experimental research. This research tried to link these two parts together and developed a model that works with experimental data and provides satisfactory results. This research is one of the few that have combined both experiment and modelling.

7.2 Contributions

The proposed model aims to understand, analyze and characterize RBC aggregate sizes and their behaviour in microcirculation. The present research contributes a great potential to the advancement of the blood flow simulations. Some of the important achievements of this work are listed below.

Experiments are designed such that the characteristics of RBC aggregation and disaggregation can be viewed under a microscope. These experiments are analyzed using image processing techniques to find RBC aggregation size in different samples. To do so, a Matlab GUI is developed to apply different image processing techniques and to find the best method for analyzing particle size. At the same time using this code, the repeatability of the analysis is guaranteed.

Aggregation and disaggregation rates are the important parameters in the population-balance method. Finding these parameters experimentally opens new paths for a numerical simulation of blood flow. Using image processing techniques, it was possible to analyze aggregate size distribution in different experiments. These results are used to find aggregation and breakage rates in Chapter 6.

The sedimentation set-up is selected for two reasons. First, the shear stress in the domain is very low and can be neglected. Second, the interaction between RBCs will not stop with time as opposed to stasis blood aggregation. Ponder [118] studied the kinetic of RBC aggregation in stasis and suggested that there is a linear relation between the aggregation rate and the hematocrit (constant Ω_A). This relationship can be seen in the experimental data.

Since the disaggregation rate is a function of shear rate, a steady-state Couette flow is used to find this function. Chen and Huang [88] suggested a linear relationship between shear rate and macroscopic disaggregation rate, where Owens [11] suggests a power law relationship. Both relationships were examined to find a best correlation for the macroscopic disaggregation rate. The microscopic disaggregation rate decreases the error greatly as it has more degrees of freedom. The main assumption in finding the microscopic disaggregation rate in this work is that particles only break in to two particles with a same size.

A numerical code is developed to couple the population-balance model to the fluid flow solver. In order to couple these solvers, momentum transfer between the two phases is modelled using an estimation of the hydrodynamic forces on single or aggregated RBCs. These estimations and correlations are all extracted from literature and presented in Chapter 3.

The overall size distribution obtained from the numerical model is similar to that of the experiments. However further studies can be conducted to improve the expression of the aggregation rate and consequently the size distribution. These simulations and results are the first step for further studies using population-balance modelling coupled with the Navier-Stokes equations in this field.

The numerical model shows promising results compared to experiment. Using this model, the special distribution of particles can be predicted for various flow situations. Knowing the particle distribution provides an estimate of the local viscosity of blood. Also, by using this model, one can find the particle distribution in other geometries such as bifurcations. In the next section, future works for this research are discussed.

7.3 Future Work

This research is the first step of many steps to come. Although the model was shown to be capable of modelling blood flow in microcirculation, there are a few parameters that should be studied further to improve the population-balance modelling approach. Future works are divided into two sections: the first one discusses improvements for the experimental procedure and the second part discusses improvements for the model.

7.3.1 Future Works for Experimental Procedures

The Matlab GUI code developed for the purpose of the image processing in this research has a great potential to be improved further. This code is written in a way that other users can easily add to it. There are parts in the base code that make it easy for other users to add their own filters and binary operators. This code can also be used for other studies like cell tracking, bubble movement and other mesoscale particles.

In this research, due to image processing limitations, eight classes of particles are chosen with each successive class assumed to represent particles with double the size of the previous class. This choice is made due to the difficulty of detection single blood cells or small agglomerates. By improving the image processing techniques, one could investigate more classes with different relations between the classes. Increasing the number of classes could greatly increase the accuracy of the model.

As discussed, the distribution of daughter particles when a larger particle disaggregates is not investigated in this research. Finding this distribution could help the model further in the future. The experiment for this investigation needs to be transient. Designing an experiment and applying the image processing for it is challenging.

Finding volume fraction using the images produced in the lab is another challenging analysis that can potentially improve this research greatly. The light intensity used in this research to find the cell-free layer is a good start but it has a problem: the maximum intensity is not correlated to a known volume fraction, therefore further investigation is required.

7.3.2 Future Works for Model

The developed model has a great potential to be further improved. As discussed, the current model has a dependency on finding relative velocities of particles experimentally. In this study for each situation an experiment is performed to find a table for particle relative velocity. A model for this parameter could be developed to avoid this dependency.

Additional investigation on drag and lift force correlations for actual RBCs using an experimental set-up is needed for better modelling. The drag and lift forces used in this research are derived for rigid spherical or ellipsoidal particles. Real RBCs have a biconcave shape and are not rigid.

To numerically solve the model equations presented here, a first-order accurate discretization in time and second-order accurate discretization in space are used. Improving these discretization will improve the quality of the solution greatly. By improving the accuracy in time, one could use this model to investigate the time dependency of the viscosity of blood, as Bureau [38] suggested in his research.

Changing the code from a 2D structured-mesh code to a 3D unstructured-mesh would open new paths in this field. This would allow the investigation of more complicated geometries, such as systems of connected blood vessels, as depicted in Figure 1.3.

References

[1] R. Mehri, C. Mavriplis and M. Fenech, "Red blood cell aggregation investigation and characterization in a microfluidic device," in *The Society of Rheology 86th Annual Meeting*, Philadelphia, Pennsylvania, 2014.

[2] G. Thurston, "Viscoelasticity of human blood," *Biophysical Journal*, pp. 12(9):1205-17, 1979.

[3] O. Baskurt, B. Neu and H. J. Meiselman, Red Blood Cell Aggregation, Boca Raton, FL: CRC PressTaylor & Francis Group, 2012.

[4] A. Popel and P. Johnson, "Microcirculation and hemorheology," *Annual Review of Fluid*, pp. 37(1):43-69, 2005.

[5] G. Lu, "Rheological studies on the flow behavior of two-phase solid-liquid materials," PhD thesis, Iowa State University, Ames, Iowa , 2008 .

[6] P. Bagchi, P. C. Johnson and A. S. Popel, "Computational fluid dynamic simulation of aggregation of deformable cells in a shear flow," *Journal of Biomechanical Engineering*, vol. 127, pp. 1070-1080, 2005.

[7] J. M. Sherwood, J. Dusting, E. Kaliviotis and S. Balabani , "The effect of red blood cell aggregation on velocity and cell-depleted layer characteristics of blood in a bifurcating microchannel," *Biomicrofluidics*, vol. 6, no. 2, 2012.

[8] G. Mchedlishvili, L. Gobejishvili and N. Bertashvili, "Effect of intensified red blood cell aggregability on arterial pressure and mesenteric microcirculation," *Microvasc*, pp. Res. 45, 233–242, 1993.

[9] R. Malcolm, H. I. Bicher, R. C. Duncan and M. H. Knisely, "Behavioral Effects of Erythrocyte Aggregation," *Microvascular Research*, vol. 4, pp. 94-97, 1973.

[10] J. K. Wright Chesnutt, "Discrete-Element Model od Red Blood Cell Aggregation in Blood Flow," Ph. D. thesis University of Iowa, Iowa City, IA, 2009.

[11] R. G. Owens, "A new microstructure-based constitutive model for human blood," *J. Non-Newtonian Fluid Mech.*, vol. 140, pp. 57-70, 2006.

[12] K. L. Pitts, "Rheological and velocity profile measurements of blood in microflow using micro-particle image velocimetry," Ph.D. thesis, University of Ottawa, Ottawa, Ontario, 2013.

[13] R. Mehri, "Red Blood Cell Aggregation Characterization:Quantification and Modeling Implications of Red Blood Cell Aggregation at Low Shear Rates," PhD thesis, University of Ottawa, Ottawa, 2016.

[14] S. M. Bertoluzzo, S. M. Bollini, A. Rasia and A. Raynal, "Kinetic model for

erythrocyte aggregation," *Blood Cells, Molecules, and Diseases,* vol. 25, pp. 339-349, 1999.

[15] S. Doddi, "Three-Dimensional computational modeling and simulation of biological cells and capsules," Ph.D. thesis, Rutgers university, New Brunswick, New Jersey, 2008.

[16] D. A. Fedosov, "Multiscale Modeling of Blood Flow and Soft Matter," Ph.D thesis, Brown University, Pawtucket, RI, 2007.

[17] C. Pozrikidis, Modeling and Simulation of Capsules and Biological Cells, Boca Raton, Florida: Chapman & Hall/CRC, 2003.

[18] J. Zhang, P. C. Johnson and A. S. Popel, "Red blood cell aggregation and dissociation in shear flows simulated by lattice Boltzmann method," *Journal of Biomechanics,* vol. 41, pp. 47-55, 2008.

[19] M. J. Pearson and H. Lipowsky, "Influence of erythrocyte aggregation on leukocyte margination in postcapillary venules of rat mesentery," *Am. J. Physiol.,* vol. 279, p. H1460–H1471, 2000.

[20] E. Vicaut, X. Hou, L. Decuypere and M. Duvelleroy, "Red blood cell aggregation and microcirculation in rat cremaster muscle," *Int. J. Microcirc. Clin. Exp.,* vol. 14, p. 14–21, 1994.

[21] M. Tissot Van Patot, S. MacKenzie, A. Tucker and N. Voelkel , "Endotoxin-induced adhesion of red blood cells to pulmonary artery endothelial cells," *Am J Physiol,* vol. 270, pp. L28-3, 1996.

[22] E. W. Merrill, A. M. Benis, E. Gilliland, T. K. Sherwood and E. W. Salzman, "Pressure flow relations of human blood in hallow fibers at low shear rates," *J. Appl. Physiol.,* vol. 20, p. 954–967, 1965.

[23] K. Vajravelu, S. Sreenadh and V. Ramesh Babu, "Peristaltic transport of a Herschel–Bulkley fluid in an inclined tube," *Int. J. Nonlinear Mech,* vol. 40, p. 83–90, 2005.

[24] C. Tu and M. Deville, "Pulsatile flow of non-Newtonian fluids through arterial stenosis," *J. Biomech.,* vol. 29, no. 7, pp. 899-908, 1996.

[25] I. Fontaine, D. Savery and G. Cloutier, "Simulation of ultrasound backscattering by red cell aggregates: effect of shear rate and anisotropy.," *Biophysical Journal,* vol. 82, pp. 1696-1710, 2002.

[26] Y. Liu and W. Liu, "Rheology of red blood cell aggregation by computer simulation," *Journal of Computational Physics,* vol. 220, pp. 139-154, 2006.

[27] G. Agresar, "A computational environment for the study of circulating cell mechanics and adhesion," Ph. D. thesis, University of Michigan, Ann Arbor, 1996.

[28] M. R. King and D. A. Hammer, "Multiparticle adhesive dynamics. Interactions

between stably rolling cells," *Biophysical Journal,* vol. 81, pp. 799-813, 2001.

[29] N. A. N'Dri, W. Shyy and R. Tran-Son-Tay, "Computational modeling of cell adhesion and movement using a continuum-kinetics approach," *Biophysical Journal,* vol. 85, pp. 2273-2286, 2003.

[30] C. Dong and X. X. Lei, "Biomechanics of cell rolling: shear flow, cell-surface adhesion, and cell deformability," *J. Biomechanics,* vol. 33, pp. 35-43, 2000.

[31] C. Sun, C. Migliorini and L. L. Munn, "Red blood cells initiate leukocyte rolling in postcapillary expansions: a lattice Boltzmann analysis," *Biophysical J.,* vol. 85, pp. 208-222, 2003.

[32] B. Das, H. Cohen and R. G. Muncaster, The Theory of Pseudo-rigid Bodies, New York: Springer, 1988.

[33] A. L. Fogelson, "Continuum models of platelet aggregation: formulation and mechanical properties," *SIAM Journal on Applied Mathematics,* vol. 52, pp. 1089-1110, 1992.

[34] T. Murata, "Effects of sedimentation of small red blood cell aggregates on blood flow in narrow horizontal tubes," *Biorheology,* vol. 33, pp. 267-283, 1996.

[35] N. B. Kounov and V. G. Petrov, "Determination of erythrocyte aggregation," *Math. Biosci.* , vol. 157, pp. 345-356, 1999.

[36] T. Murata and T. W. Secomb, "Effects of shear rate on rouleau formation in simple shear flow," *Biorheology,* vol. 25, pp. 113-122, 1988.

[37] V. G. Petrov and I. Edissonov, "The role of aggregation kinetics in the sedimentation of erythrocytes," *Biorheology,* vol. 33, pp. 353-364, 1996.

[38] M. Bureau, J. C. Healy, J. C. Bourgoin and M. Joly, "Rheological hysteresis of blood at low shear rate," *BioRheology,* vol. 17, pp. 191-203, 1980.

[39] W. Dzwinel, K. Boryczko and D. A. Yuen, "A discrete-particle model of blood dynamics in capillary vessels," *Journal of Colloid and Interface Science,* vol. 258, p. 163–173, 2003.

[40] I. Dulinska, M. Targosz, W. Strojny, M. Lekka, P. Czuba, W. Balwierz and M. Szymonski, "Stiffness of normal and pathological erythrocytes studied by means of atomic force microscopy," *J. Biochem. Biophys. Methods* , vol. 66, pp. 1-11, 2006.

[41] M. Navidbakhsh and M. Rezazadeh, "An immersed boundary-lattice Boltzmann model for simulation of malaria-infected red blood cell in micro-channel," *Scientia Iranica,* vol. 19, pp. 1329-1336, 2012.

[42] K. Tsubota, S. Wada, H. Kamada, Y. Kitagawa, R. Lima and T. Yamaguchi, "A Particle Method for Blood Flow Simulation, Application to Flowing Red Blood Cells and Platelets," *Journal of the Earth Simulator,* vol. 5, pp. 2-7, 2006.

[43] T. Wang, U. Rongin and Z. Xing, "A micro-scale simulation of red blood cell

passage through symmetric and asymmetric bifurcated vessels," *Scientific Reports,* vol. 10, no. 6, 2015.

[44] J. Venkatesan, D. Sankar, K. Hemalatha and Y. Yatim, "Mathematical Analysis of Casson Fluid Model for Blood Rheology in Stenosed Narrow Arteries," *Journal of Applied Mathematics,* vol. 2013, 2013.

[45] M. Sharan and A. Popel, "A two-phase model for flow of blood in narrow tubes with increased effective viscosity near the wall," *Biorheology,* vol. 38, pp. 425-428, 2001.

[46] N. Smith, A. Pullan and P. Hunter, "An anatomically based model of transient coronary blood flow in the heart," *SIAM Journal on Applied Mathematics,* vol. 62, no. 3, pp. 990-1018, 2002.

[47] M. Fenech, D. Garcia, H. J. Meiselman and G. Cloutier, "A Particle Dynamic Model of Red Blood Cell Aggregation Kinetics," *Annals of Biomedical Engineering,* vol. 37, no. 11, p. 2299–2309, 2009.

[48] J. Freund, "Numerical Simulation of Flowing Blood Cells," *The Annual Review of Fluid Mechanics,* vol. 46, pp. 67-95, 2014.

[49] H. L. Goldsmith, G. R. Cokelet and P. Gaehtgens, "Robin Fahraeus: evolution of his concepts in cardiovascular physiology," *Am J Physiol,* vol. 257, p. 1005–15, 1989.

[50] T. M. Geislinger and T. Franke, "Hydrodynamic lift of vesicles and red blood cells in flow — from Fåhræus & Lindqvist to microfluidic cell sorting," *Advances in Colloid and Interface Science,* vol. 208, p. 161–176, 2014.

[51] M. Faivre, "Red blood cells and vesicles: Deformability and behavior under flow," PhD thesis, L'universit´e Joseph Forier, Marselle, France, 2007.

[52] W. Reinke, P. Gaehtgens and P. C. Johnson, "Blood viscosity in small tubes: effect of shear rate, aggregation, and sedimentation," *Am. J. Physiol.,* vol. 253, pp. 540-547, 1987.

[53] A. R. Pries, T. W. Secomb, T. Gessner, M. Sperandio, J. F. Gross and P. Gaehtgens, "Resistance to blood flow in microvessels in vivo," *Circulation Research,* vol. 75, pp. 904-915, 1994.

[54] P. W. Rand, E. Lacombe, H. E. Hunt and W. H. Austin, "Viscosity of normal human blood under normothermic and hypothermic conditions," *Journal of Applied Physiology,* vol. 19, pp. 117-122, 1964.

[55] D. E. Brooks, J. W. Goodwin and G. V. F. Seaman, "Interactions among erythrocytes under shear," *Journal of Applied Physiology* , vol. 28, no. 2, pp. 172-177, 1970.

[56] K. Chandran, S. Rittgers and A. Yoganathan, Biofluid Mechanics, The Human Circulation, Newyork: CRC Press, Taylor & Francis Group, 2012.

[57] A. M. Robertson, A. Sequeira and R. Owens, "Rheological models for blood," in

Hemodynamical Flows: Modeling, Analysis and Simulation, Verlag Italia, Milano, Springer, 2008, pp. 211-241.

[58] S. Kim, P. K. Ong, O. Yalcin, M. Intaglietta and P. C. Johnson, "The cell-free layer in microvascular blood flow," *Biorheology,* vol. 46, no. 3, pp. 181-189, 2009.

[59] J. J. Bishop, P. R. Nance, A. S. Popel, M. Intaglietta and P. C. Johnson, "Effect of erythrocyte aggregation on velocity profiles in venules," *Am J Physiol Heart Circ Physiol,* vol. 280, no. 1, pp. 222-236, 2001.

[60] H. Kitamura, B. Sigel, J. Machi, E. Feleppa, J. Sokil-Melgar, A. Kalisz and J. Justin, "Roles of hematocrit and fibrinogen in red cell aggregation determined by ultrasonic scattering properties," *Ultrasound in Med. & Biol.,* pp. 21, 827-832., 1995.

[61] C. Alonso, A. Pries, D. Lerche and P. Gaehtgens, "Transient rheological behavior of blood in low-shear tube flow: velocity profile and effective viscosity," *Am. J. Physiol.,* vol. 268, pp. 25-32, 1995.

[62] S. Kim, R. L. Kong, A. S. Popel, M. Intaglietta and P. C. Johnson, "A computer-based method for determination of the cell-free layer width in microcirculation," *Am. J. Physiol. Heart Circ. Physiol,* vol. 13, no. 3, pp. 199-207, 2006.

[63] R. Fahraeus and T. Lindqvist, "The viscosity of the blood in narrow capillary tubes," *American Journal of Physiology,* vol. 96, p. 562, 1931.

[64] R. T. Yen and Y. C. Fung, " Effect of velocity of distribution on red cell distribution in capillary blood," *Am. J. Physiol.,* vol. 235, pp. 251-257, 1978.

[65] G. W. Schmid-Schoenbein, Y. C. Fung and B. W. Zweifech, "Vascular endothelium-leukocyte interaction," *Circ. Res.,* vol. 36, pp. 173-184, 1975.

[66] P. Gaehtgens, G. Will and F. Schmidt, "Comparative rheology of nucleated and non-nucleated red blood cells. II. Rheological properties of avian red cells suspensions in narrow capillaries," *Pfl¨ugers Arch.,* vol. 390, pp. 293-287, 1981.

[67] G. W. Schmid-Schonbein, S. Usami, R. Skalak and S. Chien, "The interaction of leukocytes and erythrocytes in capillary and postcapillary vessels," *Microvasc. Res.,* vol. 19, pp. 45-70, 1980.

[68] Y. Fung, Microcirculation. In: Biomechanics: Circulation, 2nd edition, Chapter5, New York: Springer-Verlag, 1996.

[69] G. R. Cokelet, R. Soave, G. Pugh and L. Rathbun, "Fabrication of in vitro microvascular blood flow systems by photolithography," *Microvasc. Res.,* vol. 46, pp. 394-400, 1993.

[70] D. C. Duffy, J. C. McDonald, O. J. Schueller and G. M. Whitesides, " Rapid prototyping of microfluidic systems in poly(dimethylsiloxane)," *Anal. Chem.,* vol. 70, pp. 4974-84, 1998.

[71] J. Zhou, A. Vera Ellis and N. Velcker, "Recent developments in PDMS surface

modiffication for microfluidic devices," *Electrophoresis,* vol. 31, no. 1, pp. 2-16, 2010.

[72] D. Bodas and C. Khan-Malek, "Hydrophilization and hydrophobic recovery of PDMS by oxygen plasma and chemical treatment—An SEM investigation," *Sensors and Actuators B: Chemical,* vol. 123, no. 10, p. 368–373, 2007.

[73] T. Shiga, K. Imaizumi, N. Harada and M. Sekiya, " Kinetics of rouleaux formation using TV image analyzer. I. Human erythrocytes," *American Journal of Physiology* , vol. 245, pp. H252-H258, 1983.

[74] T. Shiga, K. Imaizumi, N. Maeda and K. Kon, " Kinetics of rouleaux formation using TV image analyzer. II. Rat erythrocytes," *American Journal of Physiology,* vol. 245, pp. H259-H264, 245.

[75] S. Chen, G. Barshtein, B. Gavish, Y. Mahler and S. Yedgar, "Monitoring of red blood cell aggregability in a flow-chamber by computerized image analysis," in *International and Eighth European Conference on Clinical Hemorheology*, Vienna, Austria, 1993.

[76] S. Chen, B. Gavish, S. Zhang, Y. Mahler and S. Yedgar, "Monitoring of erythrocyte aggregate morphology under flow by computerized image analysis," *Biorheology,* vol. 32, no. 4, pp. 487-496, 1995.

[77] K. L. Pitts and M. Fenech, "High speed versus pulsed images for micro-particle image velocimetry: a direct comparison of red blood cells versus fluorescing tracers as tracking particles," *Physiological Measurement,* vol. 34, pp. 1363-1374, 2013.

[78] Y. Sugii, A. Nakano, S. Nishio and M. Minamiyama, "Blood flow velocity measurement in microcirculation field," *Nihon Kikai Gakkai Ronbunshu B,* vol. 67, p. 2431–6, 2001.

[79] Y. Sugii, R. Okuda, K. Okamoto and H. Madarame, "Velocity measurement of both red blood cells and plasma of in vitro blood flow using high-speed micro PIV technique," *Meas. Sci. Tech.,* vol. 16, p. 1126–30, 2005.

[80] L. Bitsch, L. H. Olesen, C. H. Westergaard, H. Bruus, H. Klank and J. P. Kutter, "Micro particle-image velocimetry of bead suspensions and blood flows," *Exp. Fluids,* vol. 39, p. 507–13, 2005.

[81] R. Lima, T. Ishikawa, Y. Imai, M. Takeda, S. Wada and T. Yamaguchi, "Measurement of individual red blood cell motions under high hematocrit conditions using a confocal micro-PTV system," *Ann. Biomed. Eng.,* vol. 37, pp. 1546-59, 2009.

[82] R. Lima, S. Wada, M. Takeda, K. Tsubota and T. Yamaguchi, "In vitro confocal micro-PIV measurements of blood flow in a square microchannel: the effect of the haematocrit on instantaneous velocity profiles," *J. Biomech.,* vol. 40, pp. 2752-7, 2007.

[83] R. A. Gaspar and G. B. Thurston, " Erythrocyte aggregate rheology by transmitted and reflected light. 1988;25:471–87.," *Biorheology*, vol. 25, p. 471–87, 1988.

[84] J. Stoltz, F. Paulus and M. Donner, " Experimental approaches to erythrocyte

aggregation," *Clin Hemorheo,* pp. 109-118, 1987.

[85] M. Hardeman, P. Goedhart, J. G. G. Dobbe and K. P. Lettings, "Laser-assisted optical rotational cell analyzer: a new instrument for measurement of various structural hemorheological parameters," *Clin Hemorheol,* vol. 14, p. 605–18, 1994.

[86] M. Singh and M. Kumaravel, " A computerized system for sequential analysis of aggregation of erythrocyte under dynamic conditions," *Comput Biomed Res,* vol. 27, p. 325–36, 1994.

[87] C. V. L. Pop and S. Neamtu, "Aggregation of red blood cells in suspension: study by light-scattering technique at small angles," *Journal of Biomedical Optics,* vol. 13, no. 4, p. 041308, 2008.

[88] J. Chen and Z. Huang, "Analytical model for effects of shear rate on rouleau size and blood viscosity," *Biophysical Chemistry,* vol. 58, pp. 273-279, 1996.

[89] J. J. Bishop, P. R. Nance, . A. S. Popel, M. Intaglietta and P. C. Johnson, "Relationship between erythrocyte aggregate size and flow rate in skeletal muscle venules," *American Journal of Physiology - Heart and Circulatory Physiology,* vol. 286, pp. H113-H120, 2004.

[90] Y. I. Cho and . K. R. Kensey, "Effects of the non-Newtonian viscosity of blood on hemodynamics of diseased arterial flows. Part 1: Steady flows," *Biorheology,* vol. 28, p. 241–262, 1991.

[91] F. Yilmaz and M. Y. Gundogdu, "A critical review on blood flow in large arteries; relevance to blood rheology, viscosity models, and physiologic conditions," *Korea-Australia Rheology Journal,* vol. 20, p. 197–211, 2008.

[92] Y. Tsuji, T. Tanaka and T. Ishida, "Lagrangian numerical simulation of plug flow of cohesionless particles in a horizontal pipe," *Powder Technology* , vol. 71, pp. 239-250, 1992.

[93] P. J. Hoogerbrugge and J. M. V. A. Koelman, "Simulating microscopic hydrodynamic phenomena with dissipative particle dynamics," *Europhysics Letters,* vol. 19, no. 3, pp. 155-160, 1992.

[94] R. D. Groot and P. B. Warren, "Dissipative particle dynamics: Bridging the gap between atomistic and mesoscopic simulation," *Journal of Chemical Physics,* vol. 107, no. 11, p. 4423–4435, 1997.

[95] S. Succi, The Lattice Boltzmann equation for fluid dynamics and beyond, Oxford: Oxford University Press, 2001.

[96] D. L. Ermak, "A computer simulation of charged particles in solution. II. Polyion diffusion coefficient," *Journal of Chemical Physics,* vol. 62, p. 4197, 1975.

[97] K. Schulten and I. R. Epstein, "Recombination of radical pairs in high magnetic fields: a path integral-Monte Carlo treatment," *Journal of Chemical Physics,* vol. 71, p. 309, 1979.

[98] R. Ata and A. Soulaimani, "A stabilized SPH method for inviscid shallow water flows," *International Journal for Numerical Methods in Fluids,* vol. 47, no. 2, pp. 139-159, 2005.

[99] A. Tartakovsky, P. Meakin, T. D. Scheibe and R. E. West, "Simulations of reactive transport and precipitation with smoothed particle hydrodynamics," *Journal of Computational Physics,* vol. 222, pp. 654-672, 2007.

[100] S. T. O'Connell and P. A. Thompson, "Molecular dynamics-continuum hybrid computations: a tool for studying complex fluid flows," *Physical Review E,* vol. 52, no. 6, p. 5792–5795, 1995.

[101] X. B. Nie, S. Y. Chen, W. N. E and M. O. Robbins, "A continuum and molecular dynamics hybrid method for micro- and nano-fluid flow," *Journal of Fluid Mechanics,* vol. 500, pp. 55-64, 2004.

[102] R. Delgado-Buscalioni and P. V. Coveney, "Continuum-particle hybrid coupling for mass, momentum, and energy transfers in unsteady fluid flow," *Physical Review E,* vol. 67, no. 4, p. 046704, 2003.

[103] T. Werder, J. H. Walther and P. Koumoutsakos, "Hybrid atomistic-continuum method for the simulation of dense fluid flows," *Journal of Computational Physics,* vol. 205, no. 1, pp. 373-390, 2005.

[104] M. Fyta, S. Melchionna, E. Kaxiras and S. Succi, "Coupling Lattice Boltzmann with atomistic dynamics for the multiscale simulation of nano-biological flows," *Computing in Science and Engineering,* p. arXiv:0710.1272v1, 2007.

[105] A. Dupuis, E. M. Kotsalis and P. Koumoutsakos, "Coupling lattice Boltzmann and molecular dynamics models for dense fluids," *Physical Review E,* vol. 75, no. 4, 2007.

[106] M. V. Smoluchowski, "Veruch einer mathematischen theorie der koagulationkinetik kolloider losungen," *Z. Phys. Chem.,* vol. 192, pp. 129-168, 1917.

[107] D. Ramkirishna, "Statistical models of cell populations," *Advances in BioChemical Engineering,* vol. 11, pp. 1-47, 1979.

[108] B. Venneker, "Turbulent non-Newtonian fluid flow and gas dispersion in stirred vessels," PhD thesis, Delft University of Technology, Delft, 2002.

[109] S. Yuu and T. Oda, "Disruption mechanism of aggregate aerosol particles through an orifice," *J. AIChE,* vol. 29, pp. 191-198, 1983.

[110] D. Kinneberg and J. Herbst, "A comparison of linear and nonlinear models for open-circuit ball mill grinding," *Int. J. Miner. Process,* vol. 13, pp. 143-165, 1984.

[111] M. Hounslow, "A discretized population balance for continuos systems at steady state," *J. AIChE,* vol. 36, pp. 106-116, 1990.

[112] J. Congalides and C. Georgakis, "Multiplicity patterns in atmospheric fluidized bed coal combusters," *Chemical Engineering Science,* vol. 36, pp. 1529-1545, 1981.

[113] H. Luo, H.F. Svendsen, “Theoritical model for drop and bubble breakup in turbulent dispersions”, , Vol. 42, , 1992.," *J. AIChE,* vol. 42, pp. 1225-1233, 1992.

[114] E. Chatzi and C. Kiaparissides, "Dynamic simulation of biomodal drop size distributions in low-coalescence batch dispersion system," *Chemical Engineering Science,* vol. 47, pp. 445-446, 1992.

[115] M. Grag and H. Pratt, "Measurment and modeling of droplet coalescence and breakage in pulsed plate extraction column," *J. AIChE,* vol. 30, pp. 432-441, 1984.

[116] S. Du and J. Wilson, "Modeling the effect of turbulence on the collision of cloud droplets," *J. of the Atmospheric Sciences,* vol. 52, pp. 524-529, 1995.

[117] D. Ramkrishna, Population Balances: Theory and Applications to Particulate Systems in Engineering, Academic Press, 2000.

[118] E. Ponder, "On sedimentation and rouleaux formation," *Q. J. Exp. Physiol.*, vol. 16, p. 173–194, 1924.

[119] T. I. Gombosi, Gas Kinetic Theory, Michigan: Cambridge University Press, 2003.

[120] H. Lue and H. Svendsen, "Theoretical model for drop and bubble breakup in turbulent dispersions," *AIChE Journal,* vol. 42, no. 5, p. 1225, 1996.

[121] T. Karmer and M. Clark, "Incorporation of aggregate breakup in the simulationof orthokinetic coagulation," *J. Colloid Interface Sci.,* vol. 216, p. 116–126, 1999.

[122] S. Peng and R. Williams, "Direct Measurment of Floc Breakage in Flowing Suspensions," *Journal of Colloid and interface science,* vol. 166, pp. 321-332, 1994.

[123] I. Gallily and A. H. Cohen, "On the orderly nature of the motion of nonspherical aerosol particles," *Journal of Colloid and Interface Science,* vol. 68, pp. 338-356, 1979.

[124] J. Happel and H. Brenner, Low Reynolds number hydrodynamics., Hague, Netherland: Martinus Nijhoff Publishers, 1983.

[125] R. Di Felice, "The voidage function for fluid-particle interaction systems.," *InternationalJournal of Multiphase Flow,* vol. 20, pp. 153-159, 1994.

[126] P. G. Saffman, "The lift force on a small sphere in a slow shear flow," *Journal of Fluid Mechanics,* vol. 22, pp. 358-400, 1965.

[127] P. G. Saffman, "Corrigendum to "The lift force on a small sphere in a slow shear flow," *Journal of Fluid Mechanics,* vol. 31, p. 624, 1968.

[128] D. Drew and R. Lahey Jr, "The Virtual Mass and Lift Force on a Sphere in Rotating and Straining Inviscid flow," *Int. J. Multiphase flow,* vol. 13, no. 1, pp. 113-121, 1987.

[129] K. Chandran, S. Rittgres and A. Yoganathan, Biofluid Mechanics, The Human Circulation, Boca Raton, FL: CRC Press, 2012.

[130] A. Einstein, "Eine neue Bestimmung der Moleküldimensionen," *Ann. d. Physik,* vol. 19, p. 289, 1896 with a correction vol. 34, p. 591 (1911).

[131] G. B. Jeffery, "The Motion of Ellipsoidal Particles Immersed in a Viscous Fluid,"

Proc. Roy. Soc., vol. A102, pp. 161-179, 1922.

[132] L. D. landau and E.M. Lifshitz, Fluid Mechanics, Oxford: Pergamon Press, 1987.

[133] H. A. Scheraga, "Non-Newtonian Viscosity of Solutions of Ellipsoidal Particles," *The Journal of Chemical Physics* , vol. 23, no. 8, p. 1526, 1955.

[134] O. Gliah, "In Vitro Investigation of Cell-Free Layer Formation in Microchannels: Dependency on the Red Blood Cell Aggregation and Field of Shear," University of Ottawa, Ottawa, 2017.

[135] P. Renaud, H. Van Lintel, M. Heuschkel and L. Guerin, Photo-polyme rmicrochannel technologies and applications, Banff, Canada: pp. 17–21. uTAS, Oct 1998.

[136] R. J. Holmes and N. J. Goddard, "Rapid prototyping of microfluidics," *Chips and Tips from Lab on a Chip,* 2007.

[137] A. B. Shrirao and R. Perez-Castillejos, "Simple fabrication of microfluidic devices by replicating Scotch-tape masters," *Chips & Tips (Lab on a Chip),* 2010.

[138] R. Mehri, "Micro PIV and Numerical Investigation of a Micro-Couette Blood Flow," M.A.Sc. thesis, University of Ottawa, Ottawa, 2012.

[139] S. Jayavanth and M. Singh, "Computerized analysis of erythrocyte aggregation from sequential video-microscopic images under gravitational sedimentation," *ITBM-RBM,* vol. 25, no. 2, pp. 67-74, 2004.

[140] R. Mehri, J. Laplante, C. Mavriplis and M. Fenech, "Blood Flow Analysis and Red Blood Cell Aggregation Investigation," *J. Med. Biol. Eng.,* vol. 34, no. 5, Jul 7, 2014.

[141] W. Thielicke and E. Stamhuis, "PIVlab – Towards User-friendly, Affordable and Accurate Digital Particle Image Velocimetry in MATLAB," *Journal of Open Research Software,* vol. 2, no. 1, p. 30, 2014.

[142] J. Tinevez, "Simple Tracker," Mathworks file exchange, March 2016. [Online]. Available: https://www.mathworks.com/matlabcentral/fileexchange/34040-simple-tracker.

[143] J. Munkres, "Algorithms for the Assignment and Transportation Problems," *Journal of the Society for Industrial and Applied Mathematics,* vol. 5, no. 1, pp. 32–38,, 1957 March.

[144] "ImageJ, image processing and image analysis in Java," ImageJ, [Online]. Available: https://imagej.nih.gov/ij/. [Accessed 10 12 2017].

[145] "Z-functions," [Online]. Available: http://fiji.sc/Z-functions.

[146] J. Walter, "FFT Filter," [Online]. Available: http://rsb.info.nih.gov/ij/plugins/fft-filter.html.

[147] E. Meijering, O. Dzyubachyk and I. Smal, "Imaging and Spectroscopic Analysis of Living Cells," in *Methods in Enzymology, Volume 504,* Elsevier, February 2012, pp. 183-200.

[148] E. Meijering, "MTrackJ: A Java Program for Manual Object Tracking," [Online].

Available: http://www.imagescience.org/meijering/software/mtrackj/.

[149] S. V. Patankar, Numerical Heat Transfer and Fluid Flow, London, UK: Taylor & Francis, 1980.

[150] R. J. LeVeque, Numerical Methods for Conservation Laws, Basel, Switzerland: Birkhauser Verlag, 1992.

[151] U. Ghia, K. Ghia and C. Shin, "High-Resolution for incompressible flow using the Navier-Stokes equations and a multigrid method," *Journal of Computational Physics* , vol. 48, pp. 387-411, 1982.

Appendix A. Particle Size Measurements

Table A-1: Different aggregate sizes and their volumes for Channel flow (40X)

Class i	Number of RBCs	Volume of rouleaux v_i μm^3	Diameter in Pixels	Pictures (not to scale)
1	1	90	40	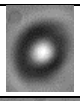
2	2	180	65	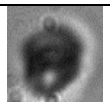
3	4	360	120	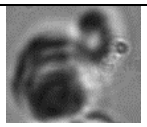
4	8	720	160	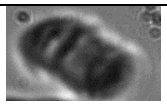
5	16	1440	430	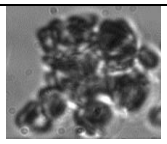
6	32	2880	900	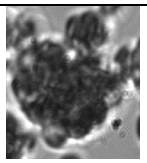
7	64	5760	1800	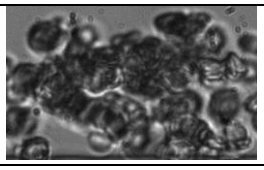

Table A-2: Different aggregate sizes and their volumes for Couette flow (20X)

Class i	Number of RBCs	Volume of rouleaux v_i μm^3	Diameter in Pixels	Pictures (not to scale)
1	1	90	20	
2	2	180	40	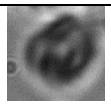
3	4	360	80	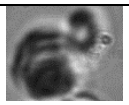
4	8	720	120	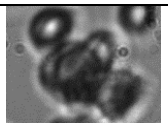
5	16	1440	240	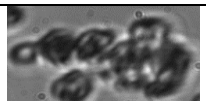
6	32	2880	480	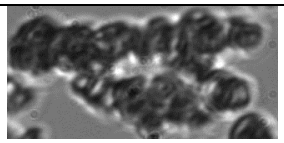
7	64	5760	960	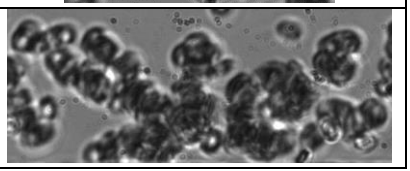

Appendix B. The SIMPLE Method

For the numerical simulation of the background fluid, the SIMPLEC method proposed by Patankar & Spalding [149] is used. This method is very similar to the SIMPLE method. Therefore, the SIMPLE method is first explained here. The specific details for the SIMPLEC method is given in Section B-1.

In the SIMPLE method, velocity and pressure are divided into an initial guess and a corrector step. The discretized continuity equation is used to compute pressure correctors that lead to a divergence-free velocity field. Velocities and pressure are then found by adding the initial guess to the correction. New velocities and pressures are considered as a new initial guess for the next iteration and the operation is repeated until the convergence is achieved.

To see the steps in more details, consider a transfer equation in its general form as

$$\frac{\partial}{\partial t}(\rho\phi_i)+\nabla\cdot(\rho\,\phi_i\vec{u})=\nabla\cdot(\Gamma\,\nabla\phi_i)+S_\phi, \tag{B-1}$$

Where an arbitrary field, φ, is treated. Here, Γ is the corresponding diffusion coefficient and S_φ is the source term. By choosing an appropriate field, φ, the continuity and momentum equation can be recovered. These terms are introduced in table D-1.

Table B-1: Transport equations parameters

Equation	φ	Γ	S_φ
Continuity Equation	1	0	0
Momentum equation in x direction	u	μ	$-\frac{\partial P}{\partial x}+F_{particles}$
Momentum equation in y direction	v	μ	$-\frac{\partial P}{\partial y}-\rho g+F_{particles}$

Here u and v are the velocities in the *x* and *y* directions, μ is the fluid viscosity, ρ is the density of fluid and P is the pressure. In the finite-volume method, Equation (B-1) is integrated over a control-volume consisting of a computational cell,

$$\frac{\partial}{\partial t}\left(\int_V \rho\phi \,\mathrm{d}V\right)+\int_A \vec{n}\cdot\left(\rho\,\phi\vec{u}\right)\mathrm{d}A=\int_A \vec{n}\cdot\left(\Gamma\,\nabla\phi\right)\mathrm{d}A+\int_V S_\phi \mathrm{d}V\ . \tag{B-2}$$

Here, V is the volume of the computational cell, A is the area of the computational cell surface and $\vec{n}$ is the outward-facing normal vector that is perpendicular to the surface of the cell. For time discretization it is necessary to integrate the transport equation (Equation B-2) from t and $t+\Delta t$ as

$$\int_t^{t+\Delta t}\left(\frac{\partial}{\partial t}\left(\int_V \rho\phi \,\mathrm{d}V\right)\right)\mathrm{d}t+\int_t^{t+\Delta t}\left(\int_A \vec{n}\cdot\left(\rho\,\phi\vec{u}\right)\mathrm{d}A\right)\mathrm{d}t=\int_t^{t+\Delta t}\left(\int_A \vec{n}\cdot\left(\Gamma\,\nabla\phi\right)\mathrm{d}A\right)\mathrm{d}t+\int_t^{t+\Delta t}\left(\int_V S_\phi \mathrm{d}V\right)\mathrm{d}t\ . \tag{B-3}$$

As discussed, the SIMPLE method uses a staggered grid, which means that, in the two dimensional case, there are three different control volume. These control volumes are shown in Figure B-1, B-2 and B-3. Figure B-1 shows the scaler control-volume. The scaler control-volume is mainly used for continuity equation where the pressure is the unknown. Note that the pressure is estimated at locations indexed using capital letters I and J. Figure B-2 shows the *x*-momentum control-volume. In the *x*-momentum control volume, the velocity in the *x*-direction is estimated at i and J locations. Finally, Figure B-3 shows the *y*-momentum control-volume. In the *y*-momentum control-volume the velocity in *y*-direction is estimated at I and j location.

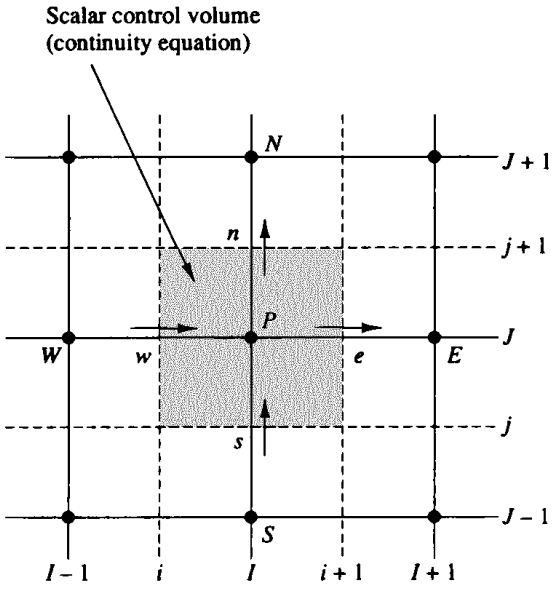

Figure B-1: Scalar control-volume in staggered grid [149].

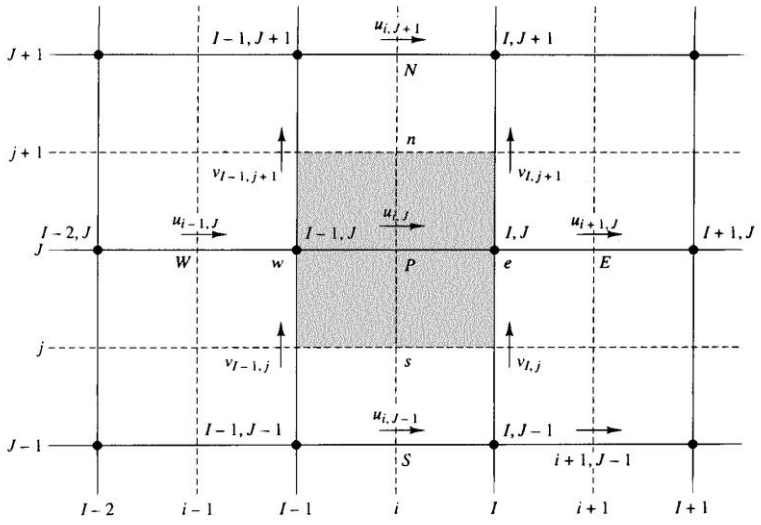

Figure B-2: Control-volume for x momentum equation in staggered grid [149].

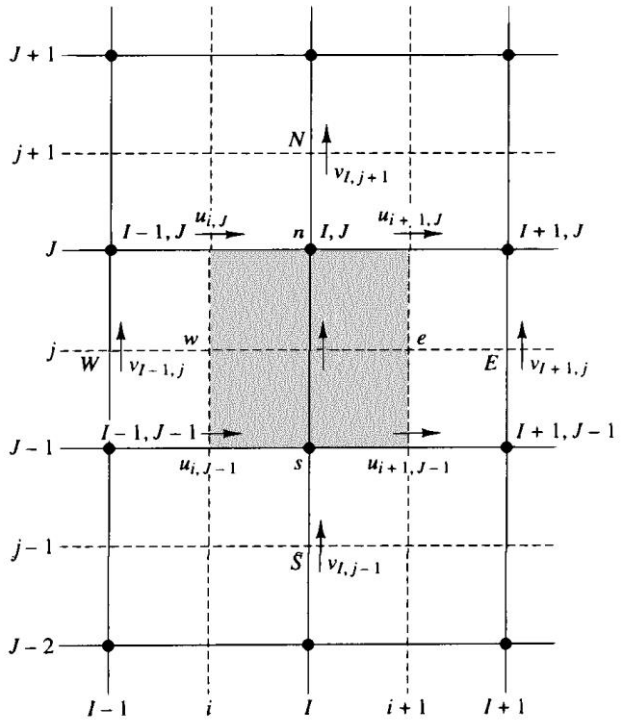

Figure B-3: Control-volume for y momentum equation in staggered grid [149].

Mass flux can be defined as $F = \rho u A$ and the diffusion coefficient over a control-volume can be defined as $D = \Gamma A/\Delta l$. Where, A is the cell's face area and Δl is the length of the cell. Using the mass flux and diffusion coefficient, a Peclet number can be defined as $\mathrm{Pe} = F/D$. In cases when the Reynolds number is low, a central difference method is used for discretization in space ($\mathrm{Re} < 400$). This leads to

$$\left(\rho_p^{t+\Delta t}\phi_P^{t+\Delta t} - \rho_p^t\phi_P^t\right)\Delta V + \int_t^{t+\Delta t}\left(F_e\varphi_e - F_w\varphi_w\right)A\mathrm{d}t + \int_t^{t+\Delta t}\left(F_n\varphi_n - F_s\varphi_s\right)A\mathrm{d}t = \int_t^{t+\Delta t}\left(D_e(\varphi_E - \varphi_P) - D_w(\varphi_P - \varphi_W)\right)A\mathrm{d}t + \int_t^{t+\Delta t}\left(D_n(\varphi_N - \varphi_P) - D_s(\varphi_P - \varphi_S)\right)A\mathrm{d}t + S_\phi\Delta V\,\Delta t. \quad \text{(B-4)}$$

In other cases, depending on the Peclet number, other method of discretization might be used (for example the upwind method). Discretization choices are shown in table B-2. In Equation B-4, the indices used correspond to those in the Figure B-3.

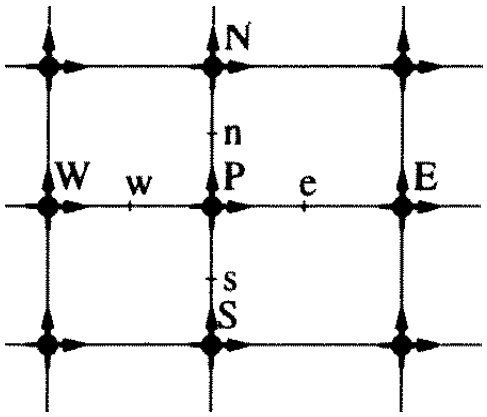

Figure B-4: Spatial discretization notation [149]

For solving this equation, it is necessary to estimate ϕ_e, ϕ_n, ϕ_w and ϕ_s. If the central difference method is again applied, it can be shown that

$$\phi_e = \frac{\phi_E + \phi_P}{2}, \quad \phi_n = \frac{\phi_N + \phi_P}{2}, \quad \phi_w = \frac{\phi_W + \phi_P}{2} \quad \text{and} \quad \phi_s = \frac{\phi_S + \phi_P}{2} \tag{B-5}$$

In the fully implicit method, parameters are estimated at $t + \Delta t$. For simplicity superscript of $t + \Delta t$ is removed and only parameters with superscript of " ^{0} " is used to indicate evaluation at the current time. The updated equation then takes the form

$$\rho_P \phi_P \frac{\Delta x \Delta y}{\Delta t} + \left(F_e \frac{\varphi_E + \varphi_P}{2} - F_w \frac{\varphi_W + \varphi_P}{2} + F_n \frac{\varphi_N + \varphi_P}{2} - F_s \frac{\varphi_S + \varphi_P}{2} \right) = \left(D_e(\varphi_E - \varphi_P) - D_w(\varphi_P - \varphi_W) + D_n(\varphi_N - \varphi_P) - D_s(\varphi_P - \varphi_S) \right) + S_\phi \Delta x \Delta y \, \Delta t + \rho_P^0 \phi_P^0 \frac{\Delta x \Delta y}{\Delta t}. \tag{B-6}$$

This equation can be written in full with i and j indices as,

$$\rho_{i,j}\phi_{i,j}\frac{\Delta x\Delta y}{\Delta t}+\left(\rho_{i-1,j}\left(\frac{u_{i-1,j}+u_{i,j}}{2}\right)\Delta y\left(\frac{\varphi_{i-1,j}+\varphi_{i,j}}{2}\right)-\rho_{i+1,j}\left(\frac{u_{i+1,j}+u_{i,j}}{2}\right)\Delta y\left(\frac{\varphi_{i+1,j}+\varphi_{i,j}}{2}\right)\right)$$
$$+\left(\rho_{i,j-1}\left(\frac{u_{i,j-1}+u_{i,j}}{2}\right)\Delta x\left(\frac{\varphi_{i,j-1}+\varphi_{i,j}}{2}\right)-\rho_{i,j+1}\left(\frac{u_{i,j+1}+u_{i,j}}{2}\right)\Delta x\left(\frac{\varphi_{i,j+1}+\varphi_{i,j}}{2}\right)\right)=$$
$$\left(\Gamma\frac{\Delta y}{\Delta x}(\varphi_{i-1,j}-\varphi_{i,j})-\Gamma\frac{\Delta y}{\Delta x}(\varphi_{i,j}-\varphi_{i+1,j})+\Gamma\frac{\Delta x}{\Delta y}(\varphi_{i,j-1}-\varphi_{i,j})-\Gamma\frac{\Delta x}{\Delta y}(\varphi_{i,j}-\varphi_{i,j+1})\right) \quad \text{(B-7)}$$
$$+S_\phi\Delta x\Delta y\Delta t+\rho^0_{i,j}\phi^0_{i,j}\frac{\Delta x\Delta y}{\Delta t}$$

The source term S_φ can also be written as $S_\varphi = S_c + S_P\phi_P$ which denote that the source term can also be a linear function of ϕ.

Considering the previous figures, the staggered grid method and Equation B-7 in addition to Table B-1, the discretized momentum equations can be written and simplified as

$$a_{i,J}u_{i,J}=\sum_{nb}a_{nb}u_{nb}+(p_{I-1,J}-p_{I,J})A_{i,J}+b_{i,J}, \quad \text{(B-8)}$$

$$a_{I,j}v_{I,j}=\sum_{nb}a_{nb}v_{nb}+(p_{I,J-1}-p_{I,J})A_{I,j}+b_{I,j}, \quad \text{(B-9)}$$

where, in these equations, b shows the source term in the computational cell and nb indicates neighbours. The information on how to calculate these parameters are given as follow:

$$\begin{aligned}
a_E &= D_e\ A(|\mathrm{Pe}_e|)+\max[-F_e,0],\\
a_W &= D_w A(|\mathrm{Pe}_w|)+\max[\ F_w\ ,0],\\
a_N &= D_n\ A(|\mathrm{Pe}_s|)+\max[-F_n,0],\\
a_S &= D_s\ A(|\mathrm{Pe}_s|)+\max[\ F_s\ ,0],\\
a_P &= a_E+a_W+a_N+a_S+a^0_P-S_p\Delta x\Delta y,\\
b &= S_c\Delta x\Delta y+a^0_P\varphi^0_P,\\
a^0_P &= \frac{\rho^0_P\Delta x\Delta y}{\Delta t}.
\end{aligned} \quad \text{(B-10)}$$

Equation B-7 is just one case that might happen in the SIMPLE method. Depending on the cell Peclet number (Pe) different methods of discretization might be used. Table B-2 shows

different methods of discretization for the function A introduced in Equation B-10. In this research the hybrid method is used. The hybrid method uses either upwind or central method depending on the cell Pe number.

Table B-2: Different method of discretization for $A(|\mathrm{Pe}|)$

Method	$A(\|\mathrm{Pe}\|)$
Central difference	$1-0.5\|\mathrm{Pe}\|$
Upwind	1
Hybrid	$\max\left[0\,,\,1-0.5\|\mathrm{Pe}\|\right]$
Power Law	$\max\left[0\,,\,(1-0.1\|\mathrm{Pe}\|)^5\right]$

It is important to note that notation from Figure B-4 is used instead of the staggered grid notation. As there are three different control-volume in that notation, it is easier to use the general notation. In the next section, the specific procedure followed for the SIMPLEC algorithm is summarized.

B-1 SIMPLEC Algorithm

In the SIMPLEC algorithm, first, the estimated pressure, p^*, is assumed to be constant from the previous time step and predicted u^* and v^* values are calculated using Equation B-8 and B-9. These calculations are done as,

$$a_{i,J}u^*_{i,J} = \sum_{nb} a_{nb}u^*_{nb} + (p^*_{I-1,J} - p^*_{I,J})A_{i,J} + b_{i,J}, \tag{B-11}$$

$$a_{I,j}v^*_{I,j} = \sum_{nb} a_{nb}v^*_{nb} + (p^*_{I,J-1} - p^*_{I,J})A_{I,j} + b_{I,j}. \tag{B-12}$$

Next, pressure and velocity correction, $`p$, $`u$ and $`v$ are defined as follow,

$$p = `p + p^*, \tag{B-13}$$

$$u = `u + u^*, \tag{B-14}$$

$$u = `u + u^*. \tag{B-15}$$

These corrections are intended to restore the divergence-free velocity field. By reducing Equation B-12 by using Equation B-9 and Equation B-13 by using Equation B-10, they can be written as

$$a_{i,J}\grave{u}_{i,J} = \sum_{nb} a_{nb}\grave{u}_{nb} + (\grave{p}_{I-1,J} - \grave{p}_{I,J})A_{i,J}, \tag{B-16}$$

$$a_{I,j}\grave{v}_{I,j} = \sum_{nb} a_{nb}\grave{v}_{nb} + (\grave{p}_{I,J-1} - \grave{p}_{I,J})A_{I,j}. \tag{B-17}$$

These, in turn, can be written as

$$\grave{u}_{i,J} = d_{i,J}(\grave{p}_{I-1,J} - \grave{p}_{I,J}), \tag{B-18}$$

$$\grave{v}_{I,j} = d_{I,j}(\grave{p}_{I,J-1} - \grave{p}_{I,J}). \tag{B-19}$$

In the SIMPLEC method $d_{i,J}$ and $d_{I,j}$ are estimated as

$$d_{i,J} = \frac{A_{i,J}}{a_{i,J} - \sum_{nb} a_{nb}}, \tag{B-20}$$

$$d_{I,j} = \frac{A_{I,j}}{a_{I,j} - \sum_{nb} a_{nb}}. \tag{B-21}$$

This allows one to calculate $u_{i,J}$ and $v_{I,j}$ as

$$u_{i,J} = d_{i,J}(\grave{p}_{I-1,J} - \grave{p}_{I,J}) + u^{*}_{i,J}, \tag{B-22}$$

$$v_{I,j} = d_{I,j}(\grave{p}_{I,J-1} - \grave{p}_{I,J}) + v^{*}_{I,j}. \tag{B-23}$$

In these equations the pressure corrector term, $\grave{p}$, is needed. The continuity equation for a control-volume can be discretized as

$$\left[(\rho uA)_{i+1,J} - (\rho uA)_{i,J}\right] + \left[(\rho vA)_{I,j+1} - (\rho vA)_{I,j}\right] = \frac{\rho_{i,J} - \rho^{0}_{i,J}}{\Delta t}. \tag{B-24}$$

By putting Equation B-22 and Equation B-23 in this equation and some simplification, it can be written,

$$a_{I,J}\grave{p}_{I,J} = a_{I+1,J}\grave{p}_{I+1,J} + a_{I-1,J}\grave{p}_{I-1,J} + a_{I,J+1}\grave{p}_{I,J+1} + a_{I,J-1}\grave{p}_{I,J-1} + \grave{b}. \qquad \text{(B-25)}$$

In this equation we have $a_{I,J} = a_{I+1,J} + a_{I-1,J} + a_{I,J+1} + a_{I,J-1} + \rho_{I,J}\Delta x\Delta y/\Delta t$ and other coefficients are equal to

$a_{I+1,J}$	$a_{I-1,J}$	$a_{I,J+1}$	$a_{I,J-1}$	$\grave{b}$
$(\rho d)_{i+1,J}\Delta y$	$(\rho d)_{i,J}\Delta y$	$(\rho d)_{I,j+1}\Delta x$	$(\rho d)_{I,j}\Delta x$	$-\rho^0_{I,J}\Delta x\Delta y/\Delta t + (\rho u^*\Delta y)_{i,J} - (\rho u^*\Delta y)_{i+1,J} + (\rho v^*\Delta x)_{I,j} - (\rho v^*\Delta x)_{I,j+1}$

To summarize, the SIMPLEC algorithm is applied by following these steps:

1- Guess the pressure field p^* or use values from previous time-step

2- Solve the momentum equations, such as equations (B-11)-(B12) to obtain u^* and v^*

3- Solve the p' equation.

4- Calculate p from equation (B-13) by adding p' to p^*.

5- Calculate u and v from their starred values using velocity correction formulas (B-22)-(B-23)

6- Solve the discretization equation for other ϕ's (such as temperature, concentration and turbulence quantities) if they influence the flow field through fluid properties, source term, etc.

7- Treat the corrected pressure as a new guessed pressure p^*, return to step 2, and repeat the whole procedure until a converged solution is obtained.

Appendix C. Extended Results

In this section the results which are used in this research but are not crucial for readers to understand the thesis are presented. First, the mean particle speed for sample EI02A in different shear rates is presented. Similar results can be produced for each sample and shear rate using the Matlab GUI code.

Table C-1: The mean particle relative speed, $\bar{g}$, between classes (pixel/s) in Couette flow for shear rate of 4.37 s^{-1} Sample EI02A

	Class 1	Class 2	Class 3	Class 4	Class 5	Class 6	Class 7	Class 8
Class 1	21.0531	25.4617	27.6783	25.7903	26.1479	25.7169	25.2487	0
Class 2	25.4717	24.6176	25.3606	24.4175	25.3021	26.0354	23.4903	0
Class 3	27.6962	25.3671	25.5597	24.9158	25.9278	26.9586	23.9163	0
Class 4	25.7841	24.4020	24.8937	24.0001	24.8663	25.6384	23.1397	0
Class 5	26.0953	25.2413	25.8589	24.8223	25.7144	26.3894	24.0505	0
Class 6	25.6028	25.9097	26.8216	25.5308	26.3253	26.8202	24.8484	0
Class 7	25.1308	23.3715	23.7892	23.0372	23.9865	24.8426	21.5288	0
Class 8	0	0	0	0	0	0	0	0

Table C-2: The mean particle relative speed, $\bar{g}$, between classes (pixel/s) in Couette flow for shear rate of 7.26 s^{-1} Sample EI02A

	Class 1	Class 2	Class 3	Class 4	Class 5	Class 6	Class 7	Class 8
Class 1	31.6065	57.1715	76.4070	105.3551	120.2629	125.4537	138.7335	0
Class 2	57.4116	59.3660	65.6954	86.5514	98.8785	105.9901	118.5261	0
Class 3	77.2483	66.1409	59.2548	68.4942	77.2140	86.3213	99.6338	0
Class 4	106.4479	87.0833	68.4510	59.3431	61.2624	73.1347	84.0825	0
Class 5	121.0099	99.0764	76.8475	61.0100	59.4665	71.1142	81.4506	0
Class 6	125.9544	105.968	85.7219	72.6728	70.9573	80.9924	92.3732	0
Class 7	136.9560	116.518	97.2861	82.1530	79.9106	90.8272	98.2602	0
Class 8	0	0	0	0	0	0	0	0

Table C-3: The mean particle relative speed, $\bar{g}$, between classes (pixel/s) in Couette flow for shear rate of 18 s^{-1}, Sample EI02A

	Class 1	Class 2	Class 3	Class 4	Class 5	Class 6	Class 7	Class 8
Class 1	118.036	177.978	240.758	230.339	234.508	263.105	281.359	0
Class 2	178.312	113.252	147.529	140.864	143.301	167.040	183.570	0
Class 3	241.276	147.569	153.863	152.980	155.211	171.931	185.145	0
Class 4	230.758	140.855	152.929	150.551	152.762	170.503	184.129	0
Class 5	234.707	143.154	155.010	152.615	154.594	172.327	186.027	0
Class 6	262.957	166.633	171.465	170.097	172.083	187.521	199.849	0
Class 7	280.897	182.925	184.444	183.493	185.564	199.634	210.955	0
Class 8	0	0	0	0	0	0	0	0

Table C-4: The mean particle relative speed, $\bar{g}$, between classes (pixel/s) in Couette flow for shear rate of 24.48 s^{-1}, Sample EI02A

	Class 1	Class 2	Class 3	Class 4	Class 5	Class 6	Class 7	Class 8
Class 1	127.374	223.714	313.820	418.275	525.641	574.947	700.629	0
Class 2	223.137	251.925	282.378	364.314	467.122	511.824	638.109	0
Class 3	314.914	284.095	215.346	243.444	333.712	373.577	505.609	0
Class 4	419.645	366.452	243.393	206.402	263.099	295.301	418.479	0
Class 5	526.735	469.303	333.244	262.785	272.067	292.287	387.330	0
Class 6	574.491	512.740	371.984	294.103	291.449	298.864	379.742	0
Class 7	697.127	636.560	501.333	415.028	384.594	378.144	422.302	0
Class 8	0	0	0	0	0	0	0	0

Table C-5: The mean particle relative speed, $\bar{g}$, between classes (pixel/s) in Couette flow for shear rate of 37.83 s^{-1}, Sample EI02A

	Class 1	Class 2	Class 3	Class 4	Class 5	Class 6	Class 7	Class 8
Class 1	123.250	213.592	343.830	458.291	575.505	733.972	823.234	0
Class 2	214.096	240.953	264.795	369.676	464.869	619.490	717.347	0
Class 3	345.055	265.114	273.337	342.684	408.582	552.923	652.168	0
Class 4	458.900	369.296	341.921	365.311	386.502	515.569	617.929	0
Class 5	575.075	463.429	406.827	385.701	333.124	419.490	520.744	0
Class 6	729.959	614.655	547.948	512.070	417.508	428.432	512.880	0
Class 7	809.848	704.024	639.285	607.074	512.659	507.314	560.351	0
Class 8	0	0	0	0	0	0	0	0

Table C-6: The mean particle relative speed, $\bar{g}$, between classes (pixel/s) in channel flow for flow rate of 6 µl/hr

	Class 1	Class 2	Class 3	Class 4	Class 5	Class 6	Class 7	Class 8
Class 1	73.824	123.334	199.932	254.925	307.453	349.990	430.558	0
Class 2	122.711	139.839	185.963	230.207	280.941	319.177	393.351	0
Class 3	198.340	185.419	164.919	176.412	222.297	242.795	312.523	0
Class 4	253.559	230.136	176.875	160.866	194.944	202.502	254.532	0
Class 5	303.835	279.044	221.444	193.688	212.290	204.474	247.925	0
Class 6	342.882	314.282	239.774	199.458	202.707	186.422	214.448	0
Class 7	417.919	383.742	305.784	248.391	243.513	212.468	188.467	0
Class 8	0	0	0	0	0	0	0	0

Table C-7: The mean particle relative speed, $\bar{g}$, between classes (pixel/s) in channel flow for flow rate of 12 µl/hr

	Class 1	Class 2	Class 3	Class 4	Class 5	Class 6	Class 7	Class 8
Class 1	73.034	134.848	205.072	271.273	310.277	369.547	389.739	0
Class 2	134.686	95.330	121.389	182.987	219.462	276.257	296.354	0
Class 3	205.018	121.503	74.088	107.956	138.675	187.102	206.864	0
Class 4	271.490	183.354	108.071	97.201	114.639	141.408	155.990	0
Class 5	310.624	219.972	138.866	114.675	118.272	128.801	138.707	0
Class 6	369.323	276.422	187.038	141.209	128.580	113.226	113.958	0
Class 7	389.241	296.332	206.654	155.666	138.374	113.881	110.755	0
Class 8	0	0	0	0	0	0	0	0

Table C-8: The mean particle relative speed, $\bar{g}$, between classes (pixel/s) in channel flow for flow rate of 18 µl/hr

	Class 1	Class 2	Class 3	Class 4	Class 5	Class 6	Class 7	Class 8
Class 1	71.021	135.037	165.650	236.937	298.992	327.726	500.941	0
Class 2	133.347	162.841	201.835	272.493	303.480	370.112	526.740	0
Class 3	159.210	196.446	208.755	267.142	335.491	344.707	510.474	0
Class 4	221.071	257.469	259.336	256.761	401.889	337.058	504.132	0
Class 5	289.699	297.776	338.214	417.346	356.985	488.125	625.991	0
Class 6	299.365	342.369	327.614	329.987	460.185	380.860	529.813	0
Class 7	453.015	482.383	480.309	488.620	584.258	524.515	587.308	0
Class 8	0	0	0	0	0	0	0	0